GRAPHITE-BEARING AND GRAPHITE-DEPLETED BASEMENT ROCKS IN THE DUFFERIN LAKE ZONE, SOUTH-CENTRAL ATHABASCA BASIN, SASKATCHEWAN

A Thesis Submitted to the College of

Graduate Studies and Research

In Partial Fulfillment of the Requirements

For the Degree of Master of Science

In the Department of Geological Sciences

University of Saskatchewan

Saskatoon

By

MARJOLAINE PASCAL

PERMISSION TO USE

In presenting this thesis in partial fulfilment of the requirements for a Postgraduate degree from the University of Saskatchewan, I agree that the Libraries of this University may make it freely available for inspection. I further agree that permission for copying of this thesis in any manner, in whole or in part, for scholarly purposes may be granted by the professor or professors who supervised my thesis work or, in their absence, by the Head of the Department or the Dean of the College in which my thesis work was done. It is understood that any copying or publication or use of this thesis or parts thereof for financial gain shall not be allowed without my written permission. It is also understood that due recognition shall be given to me and to the University of Saskatchewan in any scholarly use which may be made of any material in my thesis.

Requests for permission to copy or to make other use of material in this thesis in whole or part should be addressed to:

Head of the Department of Geological Sciences

University of Saskatchewan

114 Science Place

Saskatoon, Saskatchewan (S7N 5E2)

ABSTRACT

Unconformity-type uranium deposits from the Athabasca Basin are considered to be the result of mixing between oxidized basinal brines and basement-derived reduced fluids/gases, and/or reduced basement rocks. Graphite and/or its breakdown products are suggested to be responsible for uranium mineralization by acting as a reductant that could trigger deposition of uranium. Also, graphite is considered to be indicative of basement structures; being often concentrated along structures which can be identified as electromagnetic (EM) conductors. Thus, exploration for uranium deposits is often focused on the search for EM conductors.

Underlying the sedimentary rocks of the basin in the Dufferin Lake zone are variably graphitic pelitic schists (VGPS); altered to chlorite and hematite (Red/Green Zone: RGZ), and locally bleached equivalents near the unconformity during paleoweathering or later fluid interactions. These altered zones are texturally similar rocks within "graphite-depleted zones" as the unconformity is approached. Both zones are characterized by a lower concentration of carbon and sulfur, with the bleached zone showing higher concentrations of uranium and boron, the latter corresponding to high dravite content. The major element composition of the graphite-bearing pelitic schists and altered equivalents (RGZ) are similar. Raman analyses indicate that well-ordered carbon species (graphite to semi-graphite) are present in the pelitic schists, with both types more common within shear zones. In contrast, only rare low-ordered carbon species (carbonaceous matter) were detected in the graphite-depleted samples within the RGZ. This variation is interpreted to be the result of graphite consumption by oxidizing fluids migrating downward from the Athabasca Group. This graphite consumption may have resulted in the production of a mobile reductant (gas or fluid), which may have played a subsequent role in the deposition of uranium mineralization.

Secondary fluid inclusions (FI) examined in different quartz vein generations using microthermometry and Raman analysis, provide an indication of the fluids that have interacted with these rocks. Monophase vapor are the dominant type of fluid inclusions in the VGPS, whereas aqueous two-phase (L+V) and three-phase (L+V+Halite) FI occur in the RGZ. CH_4-dominant and N_2-dominant FI identified using Raman could be the result of fluid(s) interaction with the graphitic lithologies. This would have generated the breakdown of graphite to CH_4 and associated feldspars/micas to NH_4/N_2. CH_4, N_2 and H_2 (resulting from the decomposition of NH_4^+) represent possible reductants of uranium-bearing brines.

Two brines in the RGZ: a regional basinal fluid and an evolved fluid possibly related to U mineralization; similar to other nearby deposits, are observed. These suggest that the basinal brines have circulated in the basement rocks and have been able to evolve by interaction with the basement rocks to possibly be related to uranium mineralization.

ACKNOWLEDGMENTS

First, I would like to acknowledge Michel Cuney, without whom I would not have found this project.

I would like to acknowledge my two supervisors, Dr. Kevin Ansdell and Dr. Irvine Annesley, for their patience, support, and guidance of my graduate study. Thanks also go to Dan Jiricka, Tom Kotzer, Marie-Christine Boiron, Michel Cuney and Gerard Zaluski for their comments, suggestions and explanations.

I would like to thank Cameco for giving me the opportunity to work on this master project and for their financial and logistical support. In addition, funding was also provided by the Canadian government's TGI4 program, and an NSERC Discovery grant to Kevin Ansdell.

I am also grateful to Aaron Brown (Cameco) and Gary Witt (Cameco) for organizing field logistics, Kyle Reid (University of Saskatchewan) for field assistance, the Saskatchewan Research Council (SRC), and in particular Robert Millar, for the geochemical analyses, as well as Blaine Novakovski (University of Saskatchewan) for preparing my thin sections, Jason Maley (Saskatchewan Structural Sciences Centre) for his help with the Raman spectrometer, Georessources in Nancy (France) for having allowed me to perform the fluid inclusions study, and Thomas Bonli (University of Saskatchewan) for probe analysis.

I also thank my two roommates, Kristen and Tanner, who allowed me to have a nice environment to live, and the friendly people here in Saskatoon, including my good friend Adrienne.

Finally, big thanks goes to France, to my parents, my brothers, my sister and my boyfriend, who always supported me and who are proud of me, despite the distance, all along this amazing trip. I also thank my friends who did not forget me, and supported me as well through the journey.

TABLE OF CONTENTS

page

LIST OF TABLES

LIST OF FIGURES

CHAPTER 1
INTRODUCTION

The Athabasca Basin is located in northern Saskatchewan in Canada. It hosts the highest grade unconformity-type uranium deposits in the world, which are mainly located in the eastern part of the basin. Uranium mineralization and associated alteration are often concentrated where structures intersect the unconformity between the basin and the underlying basement rocks (Fig. 1-1).

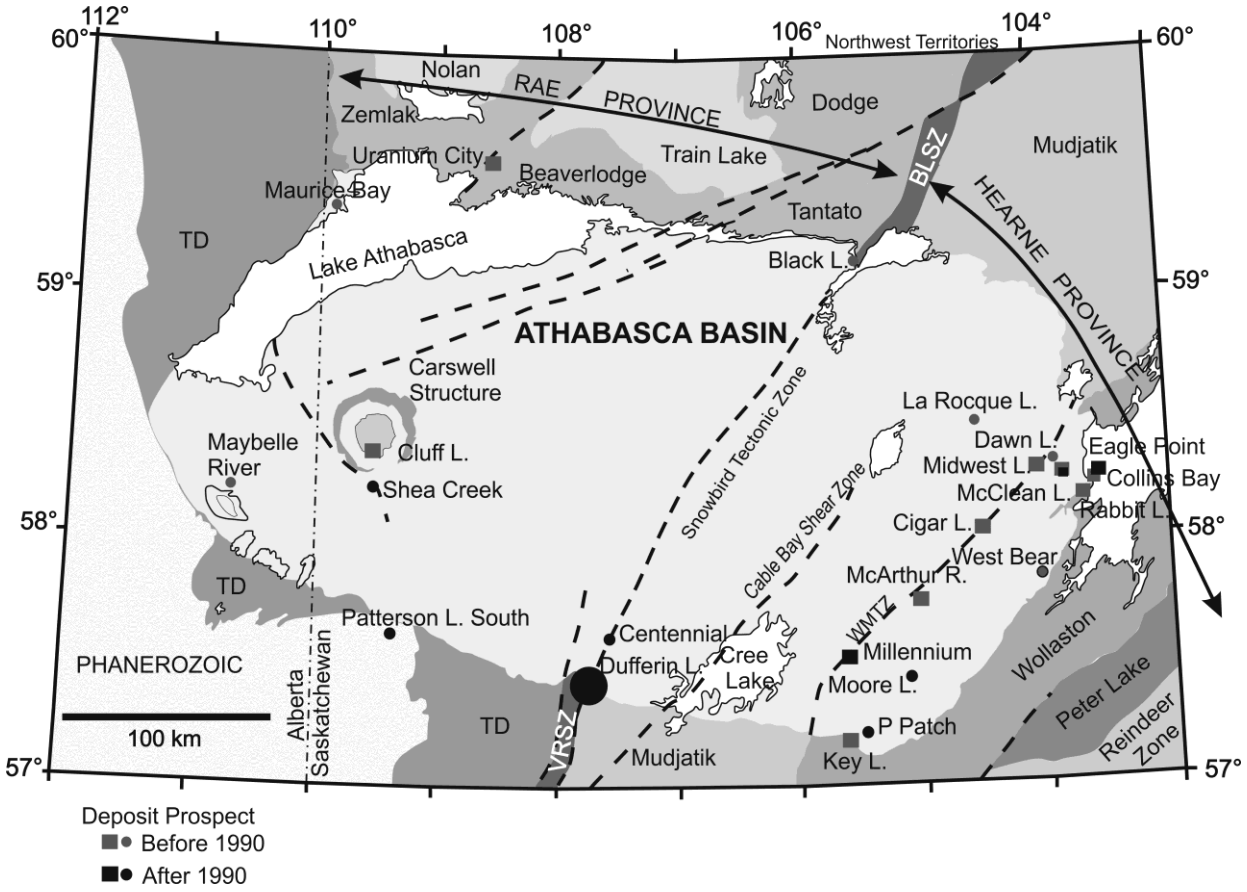

Figure 1-1. Simplified geological map of the Athabasca Basin and underlying tectonic domains (northern Saskatchewan and Alberta, Canada), showing the location of unconformity-associated uranium deposits and occurrences of the Athabasca Basin region of northwestern Canada (modified after Jefferson *et al*. 2007, Card 2012). Heavy dashed lines are selected major reactivated fault zones. TD: Taltson Domain, WMTZ: Wollaston Mudjatik transition zone, VRSZ: Virgin River Shear Zone, BLSZ: Black Lake Shear Zone

Different geochemical and geophysical methods (summarized by Jefferson *et al*. 2007) are used to target uranium mineralization, and in particular, determining the location of strong electromagnetic (EM) conductors is considered to be an important geophysical tool. These EM conductors are often associated with graphite, because graphite is a highly conductive mineral. A graphitic conductor is often associated with fault zones, which may provide the structural controls on fluid flow and uranium deposition. In addition to acting as a conduit for fluids, graphite can also act as a reductant for uranium mineralization, by generating methane (CH_4) and carbon dioxide (CO_2) (Hoeve & Sibbald 1978).

The Dufferin Lake Zone is located in the south-central Athabasca Basin. It hosts an unconformity-type uranium deposit in the sandstone (Jiricka *et al*. 2007). This unconformity-type uranium deposit is underlain by variably graphitic basement rocks, but as we approach the unconformity, they become depleted in graphite. However, metamorphic textures and structures are preserved, which obviously means that some processes removed graphite. From the graphitic rocks up to the unconformity, the graphite-depletion zone is composed of a red/green zone and a bleached zone (Appendix A). The lower part of the red/green zone is more chloritic (green zone) and progressively become more hematitic to form the red zone in the upper part of the RGZ. This profile is interpreted to be the result of paleoweathering (Macdonald 1980, 1985). However, this model has been modified to incorporate the circulation of basinal brine into the basement rocks (Cuney *et al*. 2003), overprinting the original paleoweathering profile.

Research Objectives

The purpose of this M.Sc. project was to provide constraints on the processes by which graphite had been consumed in the basement rocks. The aim was also to discuss the possible relationships between graphite and/or its breakdown products with uranium mineralization, and

thus determine if the presence of graphitic conductors is still important for the localization of a deposit. Thus, the main goal was to provide some information on the similarities and differences between the variably graphitic rocks and the ones depleted in graphite (and sulfides), by:

- Determining the mineralogy and composition of the variably graphitic pelitic schists
- Characterizing the different types of carbon species present in the graphitic and graphite-depleted samples
- Providing information on the fluid(s) that have interacted within the basement rocks

Methodology

Eight drill holes (DF-60, SW-10, SW-13, SW-17, SW-18, SW-19 and SW-20 on L250+00E, and SW-42 on L270+00E) from the Dufferin Lake Zone (DLZ) were examined at the Dufferin Lake core storage facility in July 2012. This consisted of core logging, sampling and photographing drill core. The report of this fieldwork is included as Appendix B, and presents field observations with a description of macroscopic drill core samples. All the drill holes except SW-42 are located near a graphitic conductor and near uranium mineralization. SW-42 is located in a non-mineralized zone and was studied for comparison with the rocks in the mineralized zone.

Forty-four polished thin sections were prepared at the University of Saskatchewan, to determine the mineral assemblages, texture, and types of carbon species present, using both transmitted and reflected light (Chapter 2). Appendix C provides the detailed mineralogy of the different rocks. Electron microprobe analysis were carried out on one sample from the bleached zone, one sample from the RGZ, and one graphitic sample from a fault zone, in order to examine and identify minerals and in particularly the clay minerals assemblage (Chapter 2, Appendix D). This was done using back-scattered electron (BSE) imagery and energy dispersive spectrometry

(EDS), using a JEOL 8600 superprobe electron-microprobe analyzer (EMPA), at the University of Saskatchewan. Some graphitic and non-graphitic samples were chosen for Raman analysis in order to identify the presence of carbon species, and to characterize them (Chapter 2). Raman analyses were performed at the Saskatchewan Structural Sciences Centre (SSSC) at the University of Saskatchewan. Appendix E shows some spectra of well-crystallized carbon species. The samples used for petrography were sent to Saskatchewan Research Council Geoanalytical Laboratories (SRC) in Saskatoon, Canada, for geochemical analysis. Whole-rock geochemical analysis was performed using lithium metaborate fusion and ICP-OES. A multi-element geochemical was completed by ICP-OES, using a combination of partial and total digestions. Total carbon and sulfur analyses were analyzed using a LECO induction furnace, and FeO was determined by titration. Appendix F contains the full set of geochemical results. Density of samples from the drill hole SW-18 was also determined at the Saskatchewan Research Council in order to do mass-balance calculations (Chapter 2). A fluid inclusions study was performed on doubly-polished chips of quartz from the red/green zone with no graphite, and graphitic pelitic schist, so to identify the fluids that interacted with the basement rocks, and that possibly could be related to graphite consumption (Chapter 3). Appendix G contains all of the microthermometric data. A more detailed description of the analytical methods is provided in the appropriate chapter.

Thesis Structure

This thesis is divided into four chapters including a general introduction, followed by two chapters written as manuscripts intended for publication, and a conclusions chapter, summarizing all the conclusions generated from this study. The author was responsible for all of the fieldwork, data analysis, and manuscript preparation for this thesis.

Chapters two and three each contain five sections including introduction, methodology, results, discussion, and conclusions. Dr. Irvine Annesley and Dr. Kevin Ansdell edited both manuscripts. Chapter 2 has also been reviewed by Marie-Christine Boiron, Tom Kotzer, Dan Jiricka, Michel Cuney and Gerard Zaluski. Chapter 3 has been reviewed by Dan Jiricka and Tom Kotzer.

Chapter 2 "Graphite-bearing pelitic schists and their altered equivalents in the Dufferin Lake Zone, south-central Athabasca Basin, Saskatchewan: constraints on graphite formation and destruction, and implications for uranium mineralization", documents all the similarities and differences of the collected graphitic and graphite-depleted pelitic schists samples using petrography, geochemistry, mass-balance calculations, and Raman analysis. The results and interpretations led to confirming and documenting the loss of graphite, and to the discussion of the processes that may have removed it, and its potential role in uranium mineralization.

Chapter 3 "Fluids preserved in variably altered graphitic pelitic schists in the Dufferin Lake Zone, south-central Athabasca Basin, Canada: Implications for graphite loss and uranium deposition" introduced the types of fluids that have interacted with the graphitic pelitic schist and with the rocks depleted in graphite. This part presents an explanation of the various processes by which the interaction of fluids may have removed the graphite.

The conclusions chapter (Chapter 4) summarizes the observations and conclusions made in Chapters 2 and 3. This last part is followed by a reference list, comprising the references for both chapters, followed by some appendices.

CHAPTER 2
GRAPHITE-BEARING PELITIC SCHISTS AND THEIR ALTERED EQUIVALENTS IN THE DUFFERIN LAKE ZONE, SOUTH-CENTRAL ATHABASCA BASIN, SASKATCHEWAN: CONSTRAINTS ON GRAPHITE FORMATION AND DESTRUCTION, AND IMPLICATIONS FOR URANIUM MINERALIZATION

Introduction

The world's richest uranium deposits are located in the Athabasca Basin of northern Saskatchewan. They are spatially related to the unconformity between the sedimentary rocks of the basin and underlying Archean to Paleoproterozoic basement rocks. All of the larger high grade deposits (*e.g.* Key Lake, McArthur River, and Cigar Lake) are spatially associated with graphite-related electromagnetic (EM) conductors and found within high-strain zones hosted by graphitic pelitic gneiss (Madore & Annesley 1997). This spatial relationship implies that graphite has an important role in the genesis of unconformity-type uranium deposits. It is important to understand the role of graphite, because its detection remains an important aspect of exploration targeting.

The diagenetic-hydrothermal model, initially proposed by Hoeve & Sibbald (1978), is widely accepted for the generation of the uranium deposits, and proposes that oxidized basinal fluids transporting uranium reacted at the unconformity with basement graphite to create methane (CH_4) and carbon dioxide (CO_2) leading to uranium precipitation (Hoeve & Quirt 1984, Komninou & Sverjensky 1996, Fayek & Kyser 1997). Alternatively, uranium precipitation may have occurred through the mixing of oxidized basinal fluids with basement-derived reduced fluids moving along reactivated structures (Hoeve & Sibbald 1978, Hoeve & Quirt 1987, Kotzer & Kyser 1990, Kotzer & Kyser 1995).

However, a variety of different reducing mechanisms have been suggested for unconformity-type uranium deposits, which include carbon-based reductants such as

intrabasinal fluid hydrocarbons (Alexandre & Kyser 2006), graphite/carbonaceous matter, and CH_4 and CO_2 generated from graphite (Hoeve & Sibbald 1978, Kyser *et al*. 1989, Landais *et al.* 1993, McCready *et al.* 1999a, 1999b, Annesley *et al.* 2001, Komninou & Sverjensky 1996). In addition, other reductants such as H_2S from pyrite, Fe^{2+} from chloritization of biotite or illitization of hornblende (Alexandre *et al.* 2005), and bacteria-mediated reduction (Cai *et al.* 2007) have also been proposed. Recently, modelling by Aghbelagh and Yang (2014) suggest that changes in temperature and decrease in oxygen fugacity is more important in the localization of uranium precipitation than the presence of graphite, although graphite facilitates higher grades of uranium in much less time.

This study is part of a project designed to examine the processes that may have led to the consumption of graphite in the basement rocks underlying uranium mineralization in the Dufferin Lake Zone in the south-central Athabasca Basin (Fig. 2-1). Exploration drilling, completed to test EM conductor systems in the Virgin River trend area, has indicated the presence of possible "graphite-depletion zones" near the Dufferin Lake Zone. These zones are characterized by the absence of graphite in basement rocks extending to depths of ~20-30 metres below the unconformity. This sub-horizontal zone of non-graphitic rocks is underlain by steeply dipping and texturally similar but graphite-bearing pelitic basement rocks. This situation has been interpreted elsewhere in the eastern Athabasca Basin (Annesley *et al*. 2001, McCready *et al*. 2006) to have occurred as a result of graphite consumption by basinal brine fluids migrating from the Athabasca Group unconformity into the basement rocks. This graphite consumption may have resulted in the production of a mobile reductant (gas or fluid) which may have played a

role in the deposition of uranium mineralization. The purpose of this study is to characterize the similarities and differences between the variably graphitic rocks and the zones depleted in graphite using a combination of petrography, Raman analysis, and geochemistry in order to shed light on the processes that might have consumed graphite.

Geological Setting

Regional Geology

The Athabasca Basin of northern Saskatchewan (Fig. 2-1) formed at 1700-1750 Ma (Kotzer *et al.* 1992). It is filled by the Athabasca Group which consists of a Paleoproterozoic to Mesoproterozoic quartz-rich clastic sequence, comprising four unconformity-bounded quartz sandstone sequences (Ramaekers *et al.* 2007). The lower sequence is only present in the western Athabasca Basin, and consists of coarse quartz arenite and conglomerate of the Fair Point Formation. This sequence is overlain by sequence 2, which comprises the conglomeratic Read Formation, the well-sorted Smart Formation, and the Manitou Falls Formation. The Manitou Falls Formation is dominated by quartz-rich arenites, pebbly arenites and conglomerates of fluvial origin. The Lazenby Lake Formation, which consists of quartz arenite, siltstone and sparse mudstone beds, and the Wolverine Point Formation, consisting of interbedded mudstone and quartz arenite, composes sequence 3. Finally, sequence 4 consists of quartz arenite and quartz-pebbly arenite of Locker Lake and Otherside formations.

Archean and early Paleoproterozoic basement rocks of the Taltson Domain and the Rae and Hearne provinces underlie the Athabasca Group. The Rae province and the Taltson Domain to the west and the Hearne Province to the east are separated by the

northeast-trending Snowbird Tectonic zone (STZ) (Hoffman 1988). The Dufferin Lake Zone is located along the STZ (Fig. 2-1).

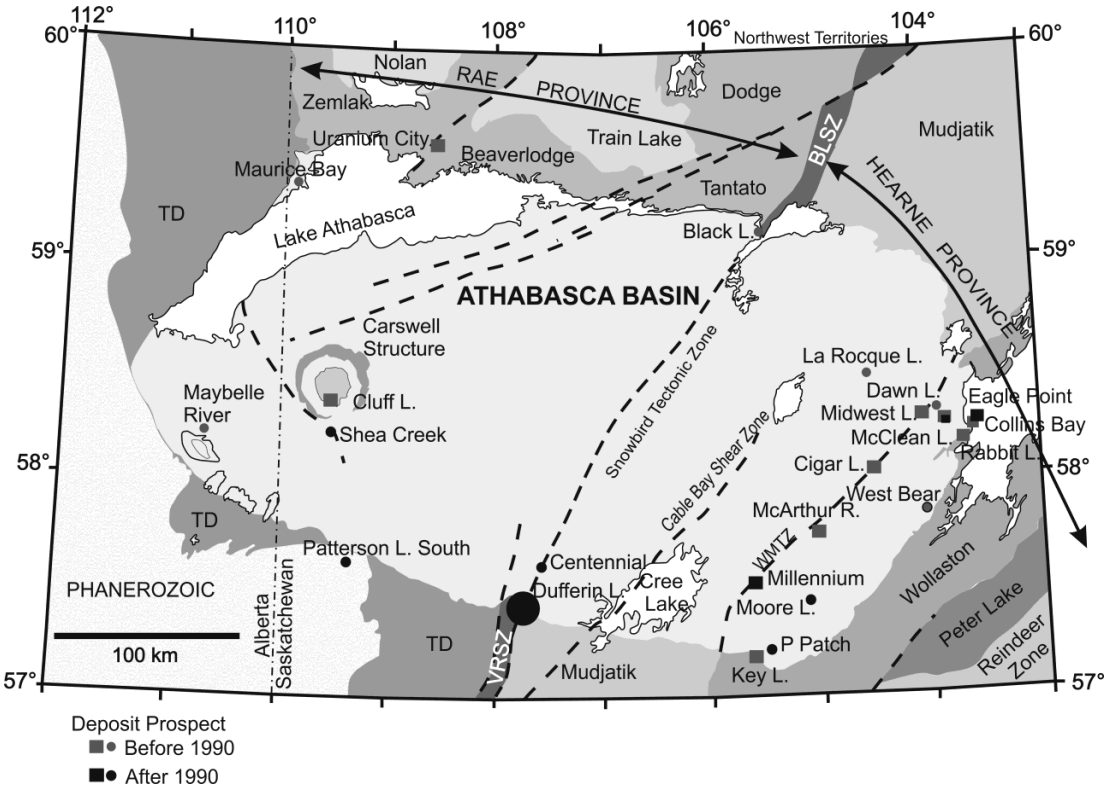

Figure 2-1. Simplified geological map of the Athabasca Basin, and underlying tectonic domains, (northern Saskatchewan, and Alberta, Canada), showing the location of unconformity-associated uranium deposits and occurrences (modified after Jefferson *et al*. 2007, Card 2012). Heavy dashed lines are selected major reactivated fault zones. The large circle shows the location of the study area, the Dufferin Lake Zone. TD: Taltson Domain, WMTZ: Wollaston Mudjatik transition zone, VRSZ: Virgin River Shear Zone, BLSZ: Black Lake Shear Zone

The Hearne and the Rae Provinces consist mainly of Archean gneisses which have been metamorphosed at greenschist to amphibolite grade and locally up to granulite grade (Card *et al.* 2007). Extensive thermotectonic reworking during the Trans-Hudson Orogen (ca. 1820-1790 Ma) within the Hearne Province differentiate it from the Rae Province (Hoffman 1988, Card *et al*. 2007). The Rae Province, north of the Athabasca Basin, has

been subdivided into several lithotectonic domains, including from west to east the Zemlak, Beaverlodge and Tantato domains (Fig. 2-1). The latter is bounded to the east by the Black Lake Shear Zone; a segment of the STZ. These rocks have been affected by the ca. 2.5-2.3 Ga Arrowsmith Orogen (Berman *et al*. 2005, Berman *et al*. 2013) and by the 2.0-1.91 Ga Taltson and Thelon orogenies.

The Hearne Province consists of the Wollaston and the Mudjatik domains (Fig. 2-1) which are separated by the Wollaston-Mudjatik Transition Zone (WMTZ; Annesley *et al.* 2005) (Fig. 2-1). The Wollaston Domain is a northeast-trending fold-thrust belt that formed during the Trans-Hudson Orogen, and is composed of Paleoproterozoic Wollaston Group metasedimentary rocks overlying Archean granitoid gneisses, whereas the Mudjatik Domain is a northeast-trending belt consisting mainly of Archean felsic gneisses (Annesley *et al.* 2005, Yeo & Delaney 2007).

The Taltson Magmatic Zone, part of the Taltson Domain, underlies the southwestern part of the Athabasca Basin (Jefferson *et al*. 2007, Pana *et al*. 2007) is considered to be the southern extension of the Thelon tectonic zone (Hoffman 1988). It consists of 2.0 to 1.9 Ga dominantly intrusive rocks that have been metamorphosed during the Taltson Orogen at ca. 1.9 Ga.

Throughout the Athabasca basin, the basement directly below the unconformity is overprinted by a subhorizontal variably bleached zone, a few metres thick, that, in turn, is underlain by strong interbanded hematitic and chloritic alteration, informally termed the Red/Green zone (RGZ). The RGZ is suggested to be a paleoweathering profile as described elsewhere by MacDonald (1980, 1985). The lower part of the RGZ is more chlorite-rich (Green zone) and is mainly characterized by the presence of the chlorite

group mineral sudoite and retains more of its primary textures than the upper part, which is more hematite-rich (Red zone) (Macdonald 1980, 1985). The middle part corresponds to the transition from the green zone to the red zone. The earlier, red alteration, characterized by pervasive hematite took place under oxidizing conditions, whereas during later green alteration, reducing conditions prevailed (Hoeve & Sibbald 1978). More recently, an alternative post-Athabasca hydrothermal origin for the RGZ has also been postulated (Cuney *et al.* 2003). The bleached zone overprints the top of the red zone of the paleoweathered profile, and is supposed to be the result of circulation of oxidized basinal brines (Jefferson *et al*. 2007).

Most of the high-grade uranium deposits in the Athabasca Basin are located in the eastern basin, in the vicinity of the graphite-rich WMTZ (Fig. 2-1). However, there are significant deposits associated with structural zones in the western part of the basin, including Shea Creek and Cluff Lake, and the new discovery at Patterson Lake South (Fig. 2-1).

Geology of the Dufferin Lake Zone

The Dufferin Lake Zone (DLZ) is astride the STZ, which, in the south-central Athabasca Basin, is represented by the Virgin River shear zone (VRSZ) (Hoffman 1990) (Fig. 2-2a). The VRSZ separates the Taltson Domain to the west from the Mudjatik domain of the Hearne province to the east (Fig. 2-2a). It is a 4.5 km wide zone of mylonitic rocks (Gilboy 1985a) and is cored by the Virgin Schist Group (Fig. 2-2a) which is composed mainly of psammopelitic to pelitic schists and amphibolites (Card & Bosman 2007, Card *et al.* 2008, Johnson 1968).

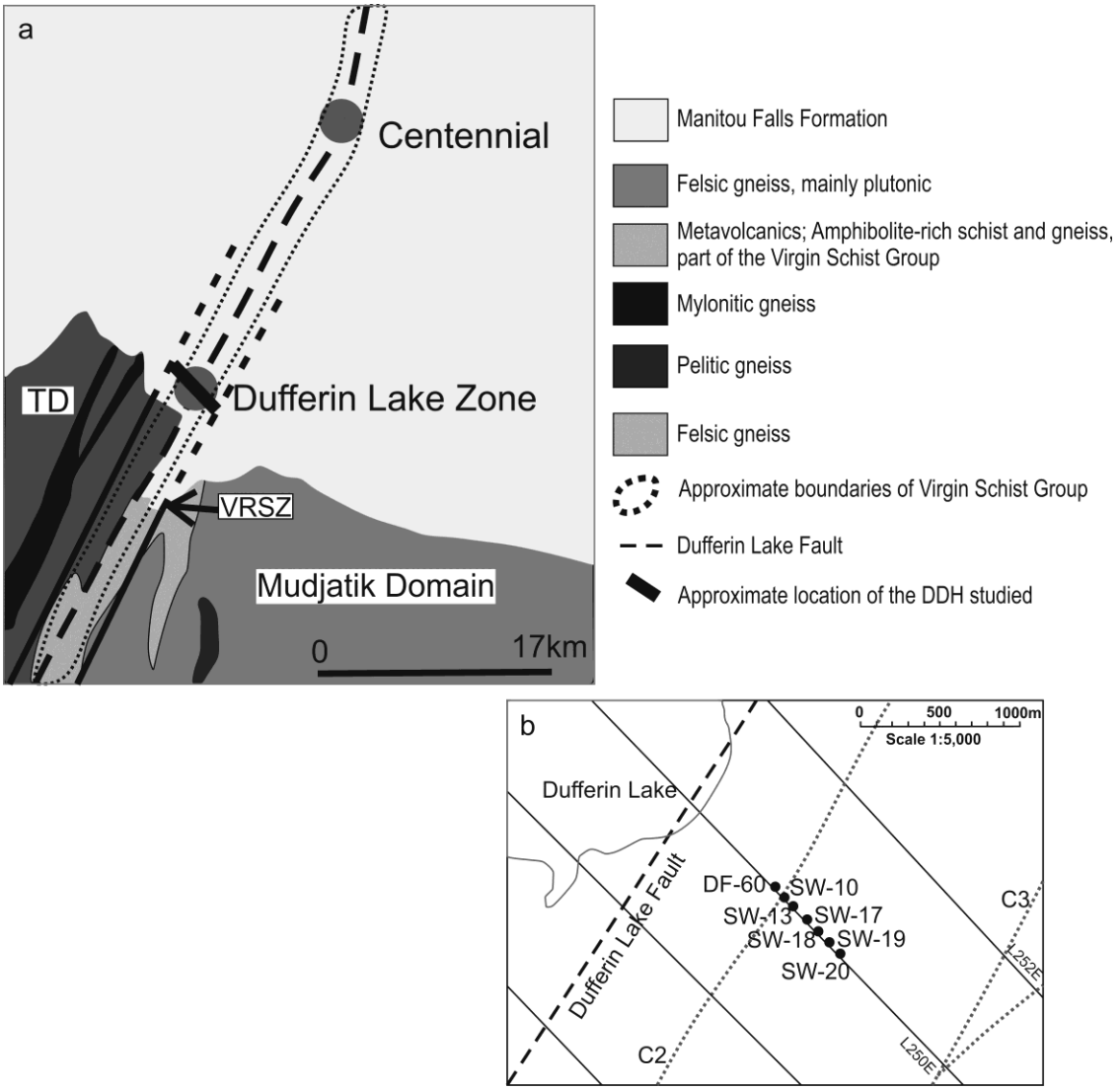

Figure 2-2. (a) Geology of Virgin River Trend including the Dufferin Lake Zone. TD: Taltson Domain, VRSZ: Virgin River Shear Zone (modified after Gilboy 1985b, Card 2009, SIR's Geological atlas of Saskatchewan). The black line indicates the location of the section of drillholes used in this study. (b) Map showing the location of the collars of the DDHs used in this study in relation to the Dufferin Lake Fault, and the conductors C2 and C3

The VRSZ area hosts unconformity-type uranium deposits and occurrences such as the Centennial Deposit (Jiricka & Witt 2002, Jiricka & Leppin 2003, Reid *et al.* 2014) and the DLZ (Jiricka *et al.* 2007). The VRSZ was reactivated after the deposition of the Athabasca Group, and is manifested as a northwest-dipping reverse fault, the Dufferin Lake fault (Fig. 2-2a), which offsets the unconformity by over 250 metres (Card *et al.* 2007, Powell *et al.* 2007). This fault could have had an important role in focusing uranium precipitation at/or near the unconformity by being the main fluid conduit (Thomas *et al*. 2000, Alexandre *et al.* 2012).

The Mudjatik Domain underlying the Athabasca Basin in the DLZ is dominated by felsic gneisses (Fig. 2-2a), but also comprise quartzites, pelitic and variably graphitic metasedimentary rocks, and amphibolites, granitoids, and pegmatites that have been metamorphosed at upper greenschist to amphibolite grade (Gilboy 1985a). The basement rocks in the Taltson Domain contain granulite-facies assemblages in its northwest part, and amphibolite-facies assemblages near the VRSZ (Card *et al.* 2008). Taltson Domain rocks consist mainly of orthogneiss, dominated by granodiorite compositions (Card *et al.* 2007, Card 2002).

Graphitic-rich EM conductors are present in the area (Fig. 2-2b), parallel to the Dufferin Lake fault (Jiricka *et al.* 2007). Significant structures, such as the Dufferin Lake fault, associated with these EM conductors provided encouragement for exploration in the area (Powell *et al.* 2007).

In the DLZ, uranium mineralization (Jiricka *et al*. 2007) is hosted in the quartz-rich arenites of the Manitou Falls Formation (Figs. 2-2 and 2-3a), just above (5 to 10m) the unconformity (Fig. 2-3a), and is associated with bleaching and clay alteration. The

basement rocks directly underlying the DLZ are composed primarily of variably graphitic (locally sulfidic) pelitic schists, with a strong foliation and shear zones which have a small angle (10 to 30°) to the core axis. As the unconformity is approached, at a depth of about 370 m, there is a gradual transition into the RGZ and finally the bleached zone (Fig. 2-3b). The RGZ is thickest in the vicinity of the more prominent shear zones (Fig. 2-3a), and appears to have lost graphite. However, metamorphic textures and structures are preserved in the least altered rocks of the RGZ (Fig. 2-3a). This implies that the variably graphitic pelitic schists did extend all the way to the unconformity, but that within the RGZ some processes must have removed graphite from these rocks. Appendix A shows the transition of the variably graphitic pelitic schists into the RGZ within the drill hole SW-20, and Appendix B presents field observations with a description of macroscopic drill core samples.

Also, several quartz generations have been identified in the basement samples (Pascal *et al*. 2013). Early quartz veins formed before the deposition of the Athabasca Basin, and two later quartz vein sets that could be related to post-Athabasca deformation and fluid flow, and therefore could potentially be related to uranium mineralization.

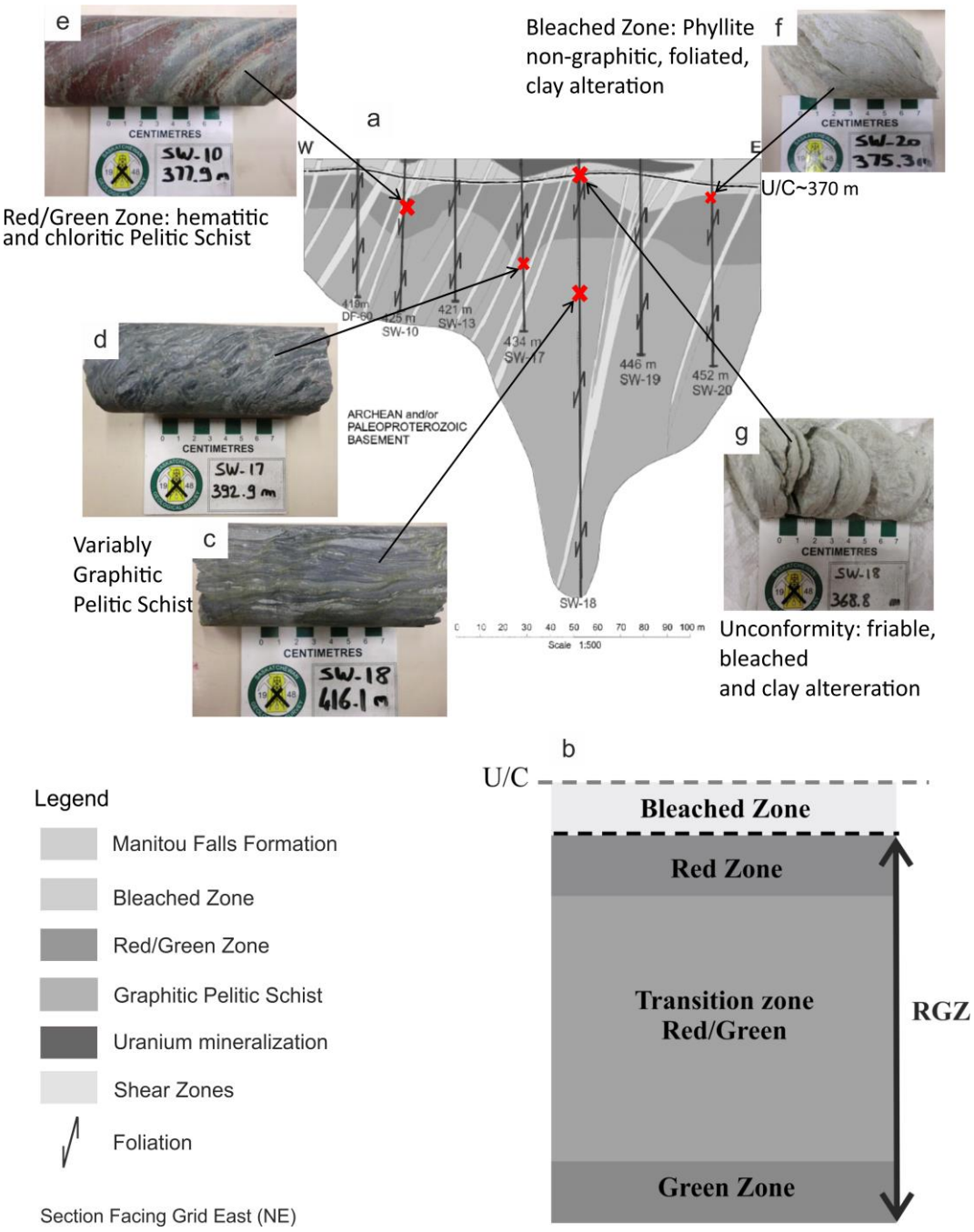

Figure 2-3. (a) Geological cross section from the Dufferin Lake Zone, illustrating the presence of graphite-depleted and graphite-rich zones, as well as the different rock units. (b) Schematic section through the RGZ profile below the unconformity (U/C). (c) and (d) Variably graphitic pelitic schists showing S1, and crenulation. (e) Pelitic schists from the RGZ with hematitic and chloritic layers (f) Foliated, clay-rich rock from the base of the bleached zone. (g) Clay-rich rock from the bleached zone at the unconformity

Sampling and Analytical Methods

Drill core samples were collected from the graphitic pelitic schists, the RGZ and from the bleached zone within the Dufferin Lake Zone (*i.e.* from drill holes DF-60, SW-10, 13, 17, 18, 19, 20 – see Figs. 2-2a, b). Polished thin sections were prepared and then investigated with a petrographic microscope under both transmitted light and reflected light at the University of Saskatchewan. Electron microprobe analysis was carried out on one sample from the bleached zone, one sample from the RGZ, and a graphitic sample from a shear zone in the basement, in order to characterize the mineral assemblage, and the clay minerals in particular. This was done on thin sections coated with carbon, using back-scattered electron (BSE) imagery and energy dispersive spectrometry (EDS), using a JEOL 8600 superprobe electron-microprobe analyser (EMPA), at the University of Saskatchewan. The EMPA were operated at an accelerating voltage of 15 kV and a beam current of 10 nA. The beam diameter was 1 μm.

Geochemical analyses were carried out at the Saskatchewan Research Council (SRC) Geoanalytical Laboratories in Saskatoon, Canada. Whole-rock geochemical analyses were performed using lithium metaborate fusion and inductively coupled plasma optical emission spectrometer (ICP-OES). A multi-element geochemical analysis was carried out by ICP-OES, using a combination of partial and total digestions. Total carbon and sulfur analyses were determined using a LECO induction furnace. Detection limits were ~0.01% for the major elements (except SiO_2), 0.1% for LOI and SiO_2, and 1 ppm for the trace elements. Detection limits for both carbon and sulfur were ~0.01%, and 2 ppm for B. Titration analysis was performed to obtain a value for FeO total in the rocks. Ferrous and ferric iron concentrations were determined using a combination of titration analysis and ICP-OES.

Mass-balance calculations were performed using whole-rock geochemical analyses and density measurements of samples collected from the longest drill hole. Density was determined using the method of volume displacement, which consists of putting the rock into water and carefully recording how much the water level rises. The amount that the water volume raises is equal to the volume of the object. From this, the density is determined using the ratio of the mass to the volume. Then, the sample which represents the least altered equivalent (*i.e.* the freshest) of the pelitic schists was chosen to compare with samples from the RGZ and bleached zones. Mass-balance calculations were resolved using the Grant isocon analysis method (Grant 1986) with freeware EasyGresGrant software (Lopez-Moro 2012).

Polished thin sections for petrographic and Raman analysis were chosen in order to 1) characterize the different type of carbon (C) species present in the variably graphitic pelitic schists and therefore to determine the sample heterogeneity, 2) to check for the presence of C species in the samples supposed depleted in graphite, and if present, 3) to determine the different C species. Note that the Raman spectra of graphitic materials having been polished can be sensitive and induce structural defects in graphitic compounds, resulting in an increase of the D band (Pasteris 1989, Wopenka & Pasteris 1993).

Spectra were acquired using a Renishaw Raman Invia Reflex Microscope SOP at the Saskatchewan Structural Sciences Center (SSSC), University of Saskatchewan. A 514.5 nm argon ion laser was used with power of 0.010W. The laser beam was focused on the sample with the x50 objectives lens of the microscope for single point analyses, and the 20x objective lens for the mapping analyses, with 100% power laser. Acquisition time

was 10 seconds with 10-15 accumulations for each spectrum. The static scan was focused on 1400cm^{-1}, allowing the observation of all the first-order peaks going from 1105 to 1700 cm^{-1} and then focused on 2800cm^{-1} allowing the observation of the second-order bands going from 2553 to 3050 cm^{-1}. The data acquisition was carried out using the computer program WiRE 3.3.

Results

Petrography

The carbon classification and terminology of this investigation follows that of Kwiecińska & Petersen (2004). The pelitic schists exhibit heterogeneous and complex textures and types of graphite (Gr), semi-graphite (HGr) and carbonaceous matter (CM) (Annesley *et al.* 2001, Kwiecińska & Petersen 2004, McCready & Annesley 2006). Appendices C and D exhibit petrographic observations, and supplementary data on microprobe analysis, respectively.

The rocks are porphyroblastic to granoblastic, and variably mylonitic. The samples display a strong ductile deformation fabric comprising mainly quartz, chlorite and muscovite, and appear to become more brittle as one approaches the unconformity. The porphyroblasts, when present, are garnet, staurolite, and/or andalusite (Wallis 1970, Gilboy 1985b), which are always retrograded (*i.e.* altered and recrystallized), even within the deeper drilling intersections of the basement rocks. Pyrite occurs as disseminated grains or in late veins. The mylonitic fabric can be contorted and locally microfolded, and shows a C-S structure, rotated porphyroblasts, and quartz boudinage. Primary layering (S0) and early foliation (S1) (Figs. 2-3c, d) are isoclinally folded (Fig. 2-3e). These rocks display a local crenulation cleavage (Figs. 2-3c, d), which overprints this fabric, as

observed in the area to the south of the DLZ and the Athabasca Basin (Card *et al*. 2007, 2008). Brittle faulting with quartz (+/- carbonates) and pyrite veins crosscut this fabric.

In the variably graphitic pelitic schists, the carbon species are often associated with pyrite and spatially associated with quartz veins. Locally, alternating quartz-rich and graphite-rich bands are observed. The porphyroblasts (garnet, staurolite, and andalusite) are generally silicified. Some carbonates veins are present. Graphite to semi-graphite (Fig. 2-4a), and CM (Fig. 2-4b), can sometimes be identified using reflected light microscopy, as the reflectivity is correlated with the degree of crystallinity. Graphite, semi-graphite and CM are concentrated along the foliation, within shear zones and along younger brittle fault zones. The carbon species are very fine grained and consist of small irregular or elongate particles, that can be dispersed in the matrix or form irregular aggregates or elongated parallel to the bedding (Fig. 2-4). Graphitic faults are composed of a mixture of graphite, illite, kaolinite, and Fe/Mg-chlorite, and locally pyrite, zircon, and rutile (Fig. 2-5a, b).

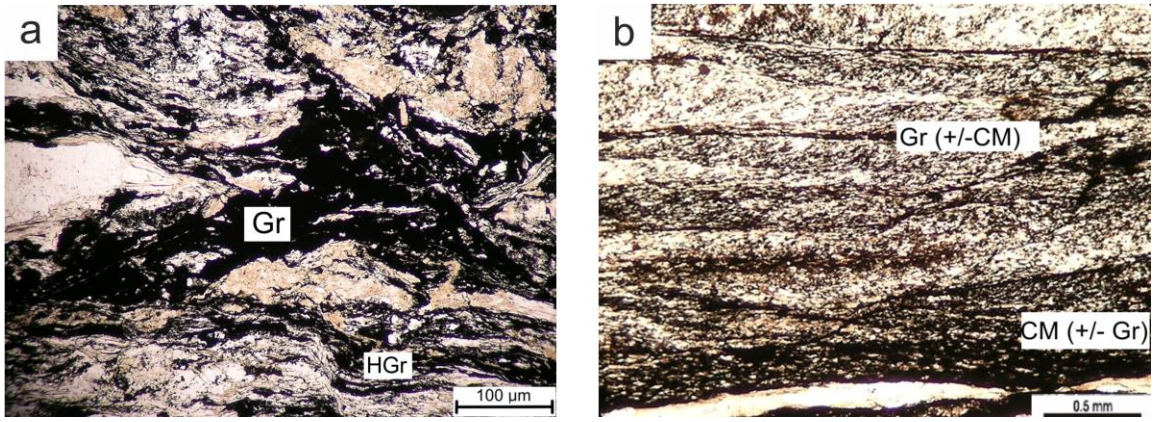

Figure 2-4. Photomicrograph of different types of carbon species in the graphitic pelitic schists (PPL Transmitted light). (a) High temperature retrograde graphite (Gr) and semi-graphite (HGr) within a high C content pelitic schists (DF60-384.2). (b) Gr and carbonaceous matter (CM) in a medium C content pelitic schist (SW18-495.0)

The alteration assemblage in the RGZ consists mainly of a mixture of Mg-chlorite and Fe-chlorite (Figs. 2-5c, d), and hematite (Figs. 2-3e, 2-6a), with no macroscopic graphite. However, some minor carbon species are present in the green-zone, *i.e.* in the lower part of the RGZ (Fig. 2-3b). Several quartz generations overprint the original fabric (Pascal *et al.* 2013) and all the porphyroblasts are replaced by quartz or by a mixture of Mg/Fe-chlorite or by hematite (Fig. 2-5d). It appears that carbon species are not present where both hematite and quartz have strongly overprinted the fabric. Zircon, apatite, rutile, calcite and pyrite occur locally in this zone, as well as siderite and quartz/siderite veins (Figs. 2-5c, d). Al-Sr-LREE phosphate and galena have also been observed.

The green zone is composed of abundant chlorite. At least two generations of chlorite can be distinguished, a pale green chlorite and a later dark chlorite (Fig. 2-6b). Most porphyroblasts in the green zone are silicified, replaced by chlorite in their cores surrounded by quartz margins, or completely altered to a mixture of chlorite and clay minerals. Locally, there are also some mica-rich zones where some carbon species are observed. In most cases, carbon species seem to be dispersed as small grains within the chloritic fabric, which makes them difficult to identify. The extent of "red alteration" increases upwards through the RGZ, into the hematite zone, described below.

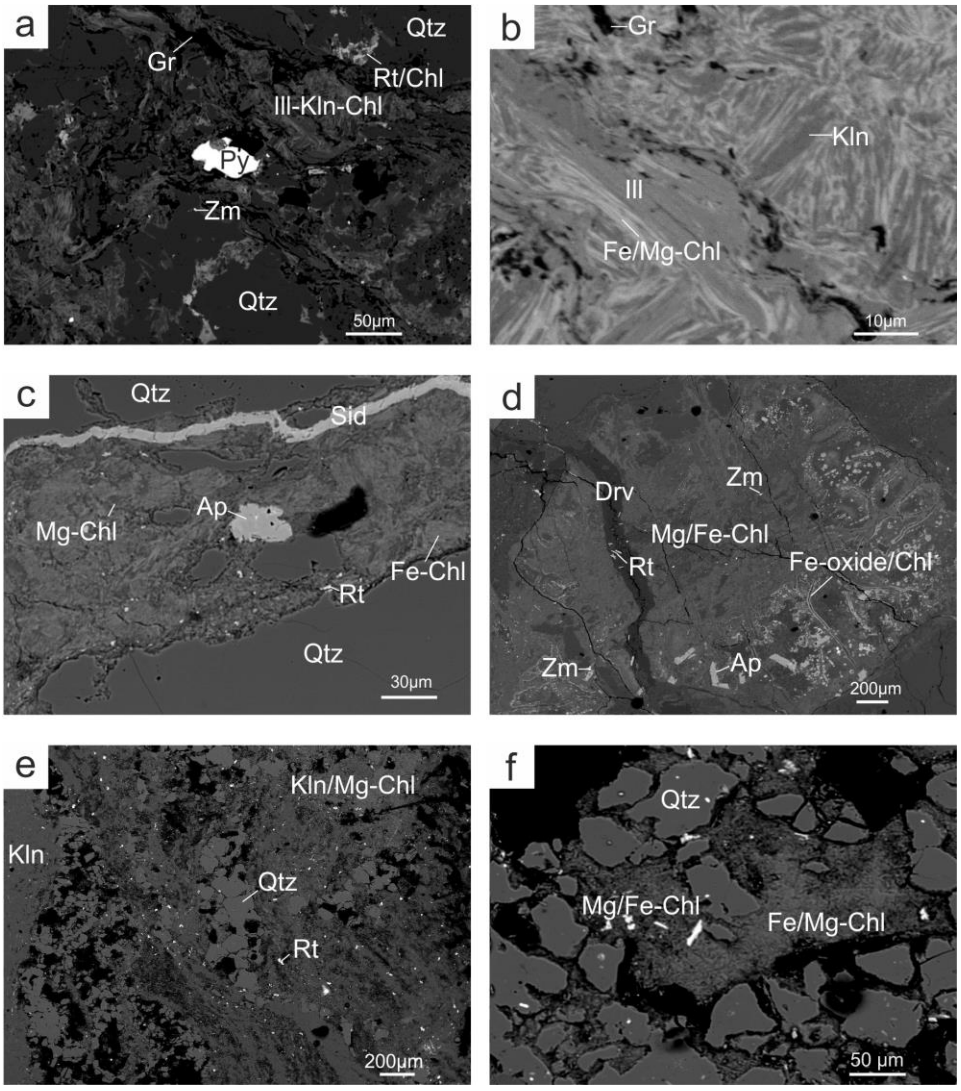

Figure 2-5. Backscatter electron images of mineral assemblages observed in the bleached zone, the RGZ, and graphitic pelitic schist. (a) Mixture of illite, kaolinite and chlorite (Ill-Kln-Chl) alteration matrix with pyrite (Py), zircon (Zm), rutile (Rt) and graphite (Gr), surrounded by quartz (Qtz) in a graphitic fault zone (DF60-380.2). (b) Intergrowth of illite, kaolinite and Fe and Mg-Chl in a graphitic fault zone (DF60-380.2). (c) Mixture of magnesium-rich chlorite (Mg-Chl; darker spots) and iron-rich chlorite (Fe-Chl; lighter spots), with apatite (Ap), rutile and siderite (Sid) vein, surrounded by quartz in the RGZ of the sample SW18-382.5. (d) Altered garnet composed of a mixture of Mg- and Fe-chlorite, with iron oxides (Fe-oxide) surrounding chlorite (Fe-oxide/Chl), apatite and zircon, crosscut by dravite (Drv) with rutile, in the RGZ of the sample SW18-382.5. (e) Kaolinite and a mixture of kaolinite and magnesium-rich chlorite (Kln/Mg-Chl) alteration matrix, with quartz and disseminated rutile in the bleached zone of the sample SW18-369.9. Black spots represent holes in the thin section. (f) Mixture of magnesium- and iron-rich chlorite, sometimes dominated by magnesium (Mg/Fe-Chl) and sometimes by iron (Fe/Mg-Chl), surrounded by quartz, in the bleached zone of the sample SW18-369.9. Black spots represent holes in the thin section

The red zone, *i.e.* the upper part of the RGZ (Fig. 2-3b), is composed mainly of pervasive hematite and clay minerals, which overprint the fabric (Fig. 2-6c). There are at least two generations of hematite; the latest being a darker hematite. All porphyroblasts in the red zone are replaced by hematite and clay minerals, or silicified. Petrographically, no obvious graphite is present in this upper part where pervasive hematite is present, and chlorite is much less abundant than in the green zone. The minerals in the red zone overprinted the RGZ which itself overprinted the green zone.

In the bleached zone, overlying the red zone and just below the unconformity, the rock texture is destroyed and drill core recovery is very poor (Fig. 2-3g). All the original silicate minerals are replaced by kaolinite, and a mixture of Mg/Fe chlorite (Figs. 2-3f, 2-6d). This bleaching process overprinted both chlorite and hematite and thus postdates the formation of the RGZ and the red zone. This zone is composed of ubiquitous hydrothermal dravite (magnesiofoitite, Alexandre *et al*. 2012). Zircon, rutile, and goyasite occur locally. Graphite was not observed.

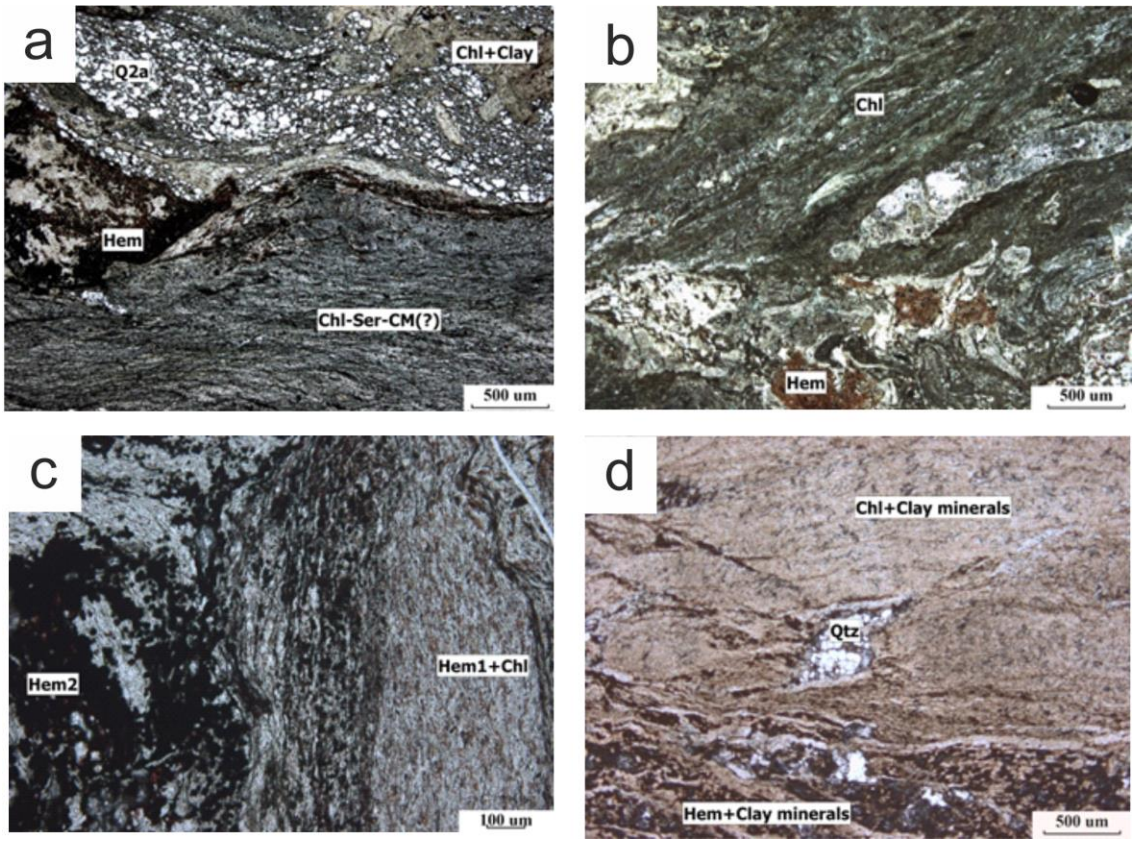

Figure 2-6. (a) Sample SW20-380.6, characteristic appearance of the RGZ with chlorite (Chl) and hematite (Hem). (b) Photomicrograph of green alteration (SW17-395). (c) Photomicrograph of red alteration (SW20-381.6). (d) Photomicrograph of a sample from the bleached zone (SW18-369.9) (PPL Transmitted light)

Raman Analysis

Raman analyses are useful in the determination and characterization of the different types of carbon species. It is a non-destructive tool allowing the measurement of the degree of crystallinity of carbon species (Tuinstra & Koenig 1970, Nemanich & Solin 1979, Pasteris & Wopenka 1991, Wopenka & Pasteris 1993, Cuesta *et al.* 1994, Bustin *et al.* 1995, Beyssac *et al*. 1999, 2002a, 2003a, 2003b) and classification as well-ordered carbon (graphite), poorly-ordered carbon (Semi-graphite) and very poorly-ordered and amorphous carbon (CM).

Raman analysis provides conclusive evidence for different types of graphite and carbonaceous matter in the basement rocks of the DLZ. The Raman spectrum of C species is composed of first-order (1100-1800cm^{-1}) and second-order (2500-3100 cm^{-1}) regions (Tuinstra & Koenig 1970, Nemanich & Solin 1979). The first-order region is composed of the graphite band (G band), and the defect bands D1, D2 and D3 bands, which occurs at 1580 cm^{-1}, 1350 cm^{-1}, 1620cm^{-1} and 1500 cm^{-1}, respectively. In poorly ordered carbons the D1 band become intense and very wide, the D2 bands is not visible because it produces a single wide peak with the G band, but it appears as a shoulder on the G band in better-ordered carbons. Finally, the D3 band is present only in poorly ordered carbons as a very wide band (Beyssac *et al*. 2002a). The increase of the D1 band is related to an increase in the amount of "unorganized" carbon in the samples and/or to a decrease in the graphite crystal size (Tuinstra & Koenig 1970). However, the G and D peaks are still present in the amorphous carbon, with different intensity, position and width. Contrary to well-ordered carbon, the development of a D peak in amorphous carbons indicates ordering (Ferrari & Robertson 2000). The second-order region (S band) is characterised by several bands occurring at 2400, 2700, 2900 and 3300 cm^{-1} (Nemanich & Solin 1979, Wopenka & Pasteris 1993), but in this study, only the 2700 cm^{-1} (S1 band) and the 2900 cm^{-1} (S2 band) have been interpreted. The S2 band appears in very poorly ordered carbon and disappears as the structural ordering increases. Figure 2-7 and Appendix E show representative spectra from different samples in which several types of carbon species are observed. Table 2-1 summarizes the most prominent data obtained from the decomposition of the first- and second-order Raman spectra. The intensity ratio R1=D/G and the peak area ratio R2=D1/(G+D1+D2) are used for

characterizing the defect quantity in graphitic materials (Pimenta *et al*. 2007). Both the R1 and R2 ratios decrease with increasing metamorphism (Beyssac *et al*. 2002a, 2002b). Moreover, the FWHM (Full Width at Half Maximum) of the G-band is also indicative of the degree of disorder, and increases as a sample becomes more disordered (Ferrari & Basko 2013).

In the variably graphitic pelitic schists, Raman spectra show the same type of spectral features. They reveal the presence of the G and D1 bands on the first-order Raman spectrum (Figs. 2-7a, b), but in some samples the presence of an additional very weak band, D2 (Fig. 2-7a). The second-order Raman is characterized by S1 and S2 bands (Figs. 2-7a, b).

Overall, the graphitic samples are characterized by a G and D1 bands centered between 1580 and 1583 cm^{-1}, and 1348 and 1360 cm^{-1}, respectively, and sometimes the D2 band centered between 1620 and 1625 cm^{-1}. The band S1 is situated around 2710-2714 cm^{-1} and the S2 band, when present, is very weak, and centered between 2910 and 2942 cm^{-1} (Fig. 2-7). The G band varies a little in intensity and thickness with the FWHM which varies between 23 and 32 cm^{-1}. The D1 band can also appear as a very wide band but with a low relative intensity meaning a lower organization in the carbon species (Fig. 2-7c). Due to this low intensity, and to show this effect better, most of these spectra with this low intensity and wide D1 band are not baseline corrected (Figs. 2-7b, c). This type of spectra appeared in areas with high luminescence due to high silicate content and is representative of zone with large amounts of quartz and chlorite. Overall, the carbon species within the graphitic pelitic schists exhibit mostly a relatively high structural organization that is typical of graphite to semi-graphite.

Table 2-1. Parameters obtained from the decomposition of Raman spectra of the first-order region

Acq.	D1		G				T1	T2	C	S	U
	Centre	FWHM	Centre	FWHM	R1	R2			%wt	%wt	ppm
VGPS2	1354.15	45.74	1580.98	23.93	0.37	0.42	456	401	3.08	5.25	7
VGPS4	1354.62	44.07	1581.29	25.02	0.34	0.39	467	418			
VGPS6	1354.72	46.31	1581.2	25.30	0.32	0.39	467	413			
VGPS11	1354.51	49.73	1581.17	22.77	0.30	0.40	465	405			
VGPS14	1355.15	48.68	1580.67	23.81	0.32	0.41	460	397			
VGPS15	1353.9	50.00	1580.76	27.78	0.29	0.39	467	406			
VGPS16	1354.01	44.32	1581.12	27.19	0.33	0.38	471	426			
VGPS22	1354.22	44.60	1581.11	24.73	0.34	0.40	463	412			
VGPS28	1354.45	44.86	1581.26	23.94	0.48	0.46	436	383			
VGPS29	1351.29	59.77	1581.09	26.17	0.42	0.51	413	313			
VGPS31	1353.26	49.01	1581.46	23.84	0.47	0.48	427	358			
VGPS35	1354.25	51.58	1581.17	26.00	0.48	0.51	415	330			
VGPS36	1354.6	56.15	1581.16	25.62	0.48	0.53	405	308			
VGPS41	1353.3	39.08	1581.65	27.49	0.43	0.40	462	432			
VGPS42	1353.85	42.39	1581.78	24.85	0.47	0.44	446	404			
VGPS43	1353.31	47.12	1581.51	23.91	0.53	0.49	423	362			
VGPS44	1352.85	48.41	1581.64	23.86	0.57	0.51	414	349			
VGPS45	1354.1	54.70	1581.59	24.93	0.60	0.54	401	325			
VGPS46	1352.93	61.31	1581.73	26.67	0.60	0.57	388	295			
VGPS60	1357.05	52.08	1582.07	27.61	0.26	0.35	483	436	1.12	1.7	6
VGPS70	1355.82	59.61	1580.68	27.36	0.30	0.41	456	383			
VGPS72	1350.34	54.02	1581.54	30.43	0.32	0.28	515	529			
VGPS78	1357.15	78.33	1581.34	28.87	0.28	0.46	435	327			
VGPS79	1353.57	77.99	1581.62	25.65	0.31	0.52	411	276			
VGPS84	1352.67	91.26	1582.48	26.23	0.33	0.56	394	241			
VGPS85	1358.41	69.50	1582.68	26.32	0.33	0.49	424	315			
VGPS86	1359.55	58.01	1582.16	26.99	0.33	0.45	440	353			
VGPS87	1357.33	55.17	1581.83	27.36	0.29	0.40	463	395			
VGPS91	1359.27	59.77	1581.99	26.52	0.32	0.45	440	349			
VGPS92	1353.15	58.88	1581.69	28.86	0.34	0.44	446	370			
VGPS93	1355.6	56.63	1581.92	26.56	0.36	0.46	436	351			
VGPS101	1356.71	51.53	1582.42	27.15	0.29	0.38	471	417			
VGPS103	1347.48	53.94	1582.61	28.28	0.42	0.47	432	356			
VGPS104	1352.52	54.12	1580.29	32.03	0.39	0.43	451	395			
VGPS105	1355.14	50.28	1582.31	27.04	0.36	0.43	450	385			
VGPS106	1357.03	50.40	1582.28	25.53	0.36	0.42	453	391			
VGPS112	1355.98	48.26	1582.94	27.12	0.45	0.45	439	383			
VGPS114	1355.53	46.47	1582.7	26.99	0.45	0.45	443	391			
VGPS120	1355.28	47.74	1582.76	27.48	0.43	0.44	444	388			
RGZ1	1359.06	47.98	1582.63	21.98	0.29	0.39	386	402	0.29	0.01	15
RGZ2	1354.57	62.21	1584.68	26.96	0.22	0.38	398	403			
RGZ3	1351.86	91.17	1582.31	27.31	0.19	0.43	364	339			

Acq.: Acquisition, R1=D1/G (peak intensity ratio), R2=D1/(G+D1+D2) (peak area ratio), VGPS: Variably graphitic pelitic schist, RGZ: Red/green zone, T1: Temperature after Beyssac et al. 2002, T2: Temperature after Rahl et al. 2005, VGPS2 to VGPS46 are in sample SW17-415.1, VGPS60 to VGPS120 are in sample SW18-495, and RGZ1 to RGZ3 are in sample SW10-389.5

Moreover, in these rocks, the R1 and R2 ratios are relatively low and vary from 0.26 to 0.60 and from 0.28 to 0.57 respectively. There is some heterogeneity within each sample, although still indicative of well-crystallized carbon species.

In the RGZ, Raman spectra revealed the presence of spectra with the G, D1 and D2 bands in the first-order region, associated with spectra in the second-order region showing the S1 band and the S2 band, with the former stronger than the latter (Fig. 2-7b). This kind of spectra is rare in the samples from the RGZ and, in particular, these spectra have been identified in sample SW10-389.5 from the upper part of the RGZ (*i.e.* the red zone). Other spectra more common in the samples from the green zone to the red zone, revealed the presence of the G, D1 and D2 bands, as well as some spectra which exhibit an indistinct G band and very wide D1 band with low intensity (Fig 2-7b- spectrum 2). The latter spectra are characteristic of amorphous carbon species and they also exhibited a high luminescence, which is due to the presence of silicates. This first-order region is associated with S1 and S2 bands in the second-order region, with, in this case, the S2 band stronger than the S1 band (Fig. 2-7b). This type of second order spectra provides evidence for the presence of very weak structural organization, and is similar to spectra from bitumen (Jehlicka *et al*. 2003). A small peak can be present around 2880 cm^{-1}, associated with the S2 band, and suggests the presence of an organic compound.

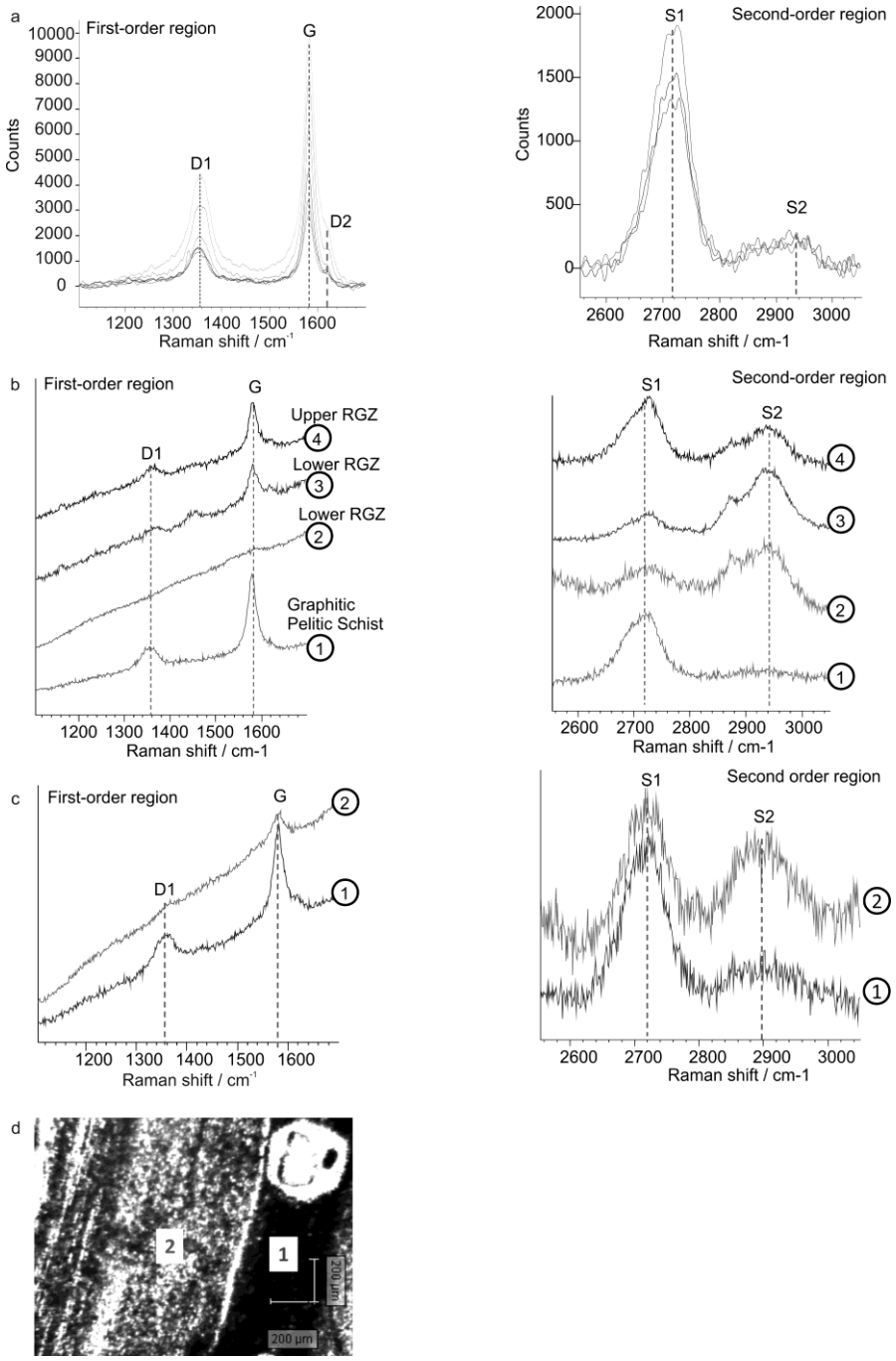

Figure 2-7. Different Raman spectra in the basement rocks. (a) Raman spectra of well-crystallised carbon species in the graphitic pelitic schists (baseline corrected). (b) Raman spectra in the first- and second-order region of carbon species in the different zones of the basement. Spectra 1 are from the graphitic pelitic schists (SW17-415.1), 2 and 3 are from the lower part of the RGZ (SW18-409.5, SW17-385.1, respectively), 4 are from the upper part of the RGZ (SW30-389.5). (c) Different type of carbon species within a same sample from the graphitic pelitic schists (SW18-495). The spectra from the region 1 show more crystallinity than the spectra from region 2 which show a lot of luminescence due to silicates and are located in a zone with lot of chlorite

The samples from the red zone have spectra with a stronger S2 band in the second-order region compared to those from the graphitic pelitic schists, indicating that the carbon-species are less well-ordered. The data of the decomposition of spectra show no major changes compared to the carbon species in the graphitic pelitic schists. The G band slightly shifts to 1582-1584 cm^{-1} and the width is mainly around 25-27 cm^{-1}. R1 and R2 ratios from this sample have been determined on the few carbon species found and vary between 0.19-0.29 and 0.38-0.43 respectively. Both of R1 and R2 ratios are quite similar to both R1 and R2 ratios of the graphitic pelitic schists. The similar R1 ratio with the well-crystallized carbon from the graphitic pelitic schists could be due to the D1 band that appears as a very wide band, but with a low relative intensity. The Raman parameters R1 and R2 of the other spectra have not been determined, due to a high luminescence in the sample and a very wide D1 band with a low relative intensity, which make the collection of the peak area and intensity data difficult with the software and thus interpretations unreliable.

Whole-Rock Geochemistry

The major-, trace-, and rare earth element geochemistry, including carbon (C), sulfur (S), and boron (B), of variably graphitic schists and graphite-depleted altered schists in the RGZ were determined from samples collected in eight selected drill holes. Results are presented in Tables 2-2, 2-3 and 2-4. The complete results are found in supplementary Appendix F.

The pelitic schists have a total carbon content that varies between 0.08 (SW20-397.5) and 5.37 (SW17-412.4) wt%, which correlates well with the amount of visually estimated graphite in each sample. Also, the samples exhibit a positive correlation between total

carbon and total sulfur (Fig. 2-8a), with sulfur reflecting the pyrite content of the schists. However, the samples from the RGZ, including the green zone to the red zone, and the bleached zone have low but variable C content (mainly between 0.08 and 0.98 wt%, but as high as 1.99 wt%) compared to the variably graphitic pelitic schists (0.48 to 5.37 wt%), whereas S is completely depleted in all the altered rocks (Fig. 2-8a). Although the C content in the RGZ is sometimes similar to the lower C content in the variably graphitic pelitic schist, there are no samples from the RGZ that have high C content comparable to the variably graphitic pelitic schist. The lowest C content can be correlated with the loss of graphite upward into the bleached zone, and can be related to carbonates such as siderite as observed in the RGZ (Fig. 2-5c). Figure 2-9 shows that the least altered graphitic pelitic schists have a variable amount of carbon. This could reflect primary sedimentological heterogeneity. The Fe^{2+}/Fe^{3+} ratio is close to 1 in the upper part of the RGZ and less than 1 in the bleached zone, whereas the lower part of the RGZ and the graphitic pelitic schists are variably reduced (Fe^{2+}/Fe^{3+} >1) (Table 2-3, Fig. 2-9).

The graphitic pelitic schists are highly variable in composition. SiO_2 contents vary between 37.5 and 70.3 wt%, with TiO_2 values ranging from 0.46 to 1 wt%, Al_2O_3 values from 11.4 to 22.1 wt%, Fe_2O_3 values from 4.14 to 26 wt%, MgO values from 1.87 to 7.22 wt%, and K_2O values from 0.17 to 5.6 wt%. The low-SiO_2 samples have the highest C, S, Fe_2O_3, and MgO contents; typical of black shales. The average concentrations of Cr, La, Ni, Th and V are comparable to Cr, La, Ni, Th and V of typical shales (Condie 1993).

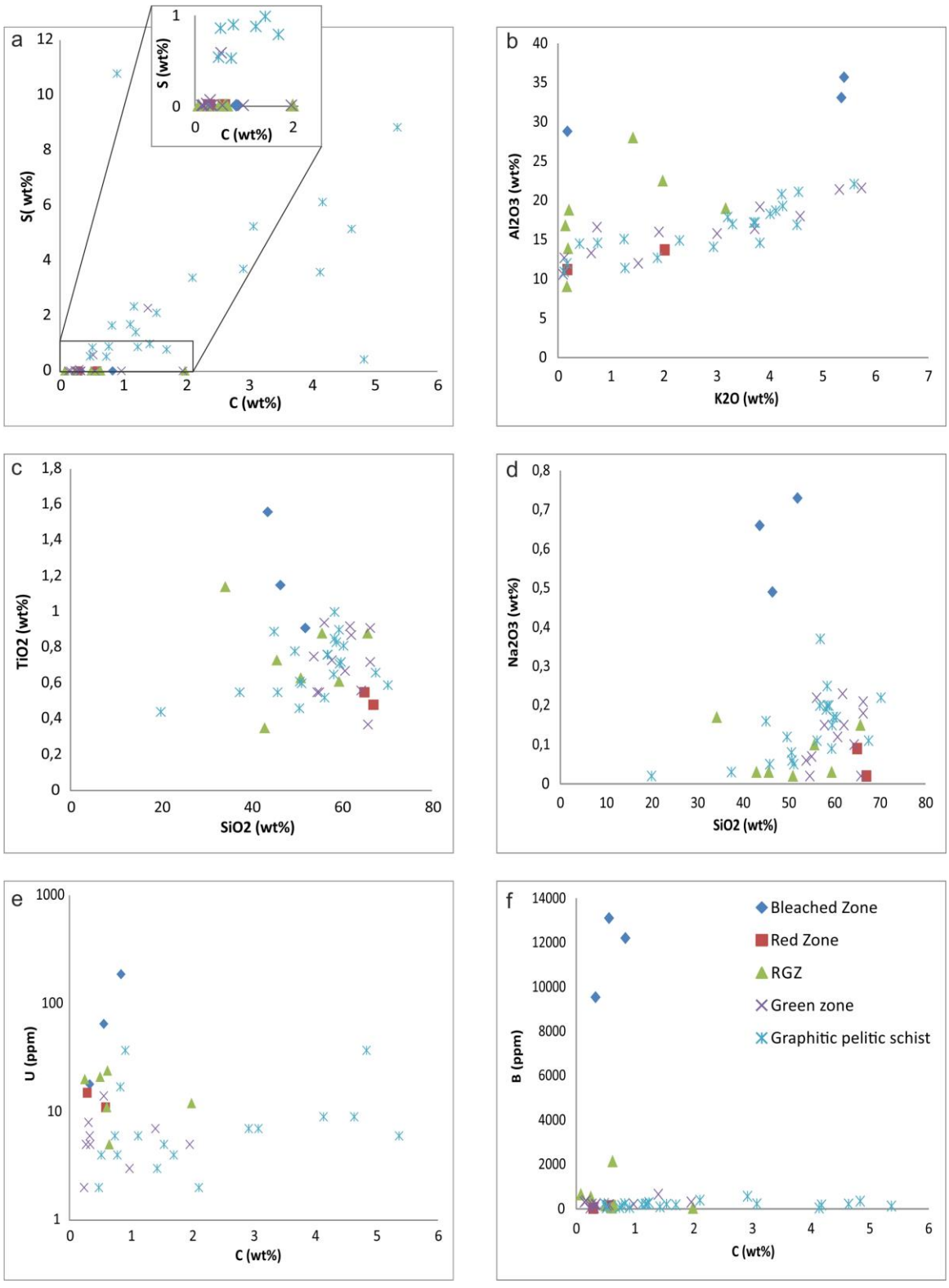

Figure 2-8. Major elements composition of the graphitic and graphite depleted rocks of the different zones of the basement. The inset in (a) shows that C content is sometimes similar in the VGPS and the RGZ, but the latter is always low

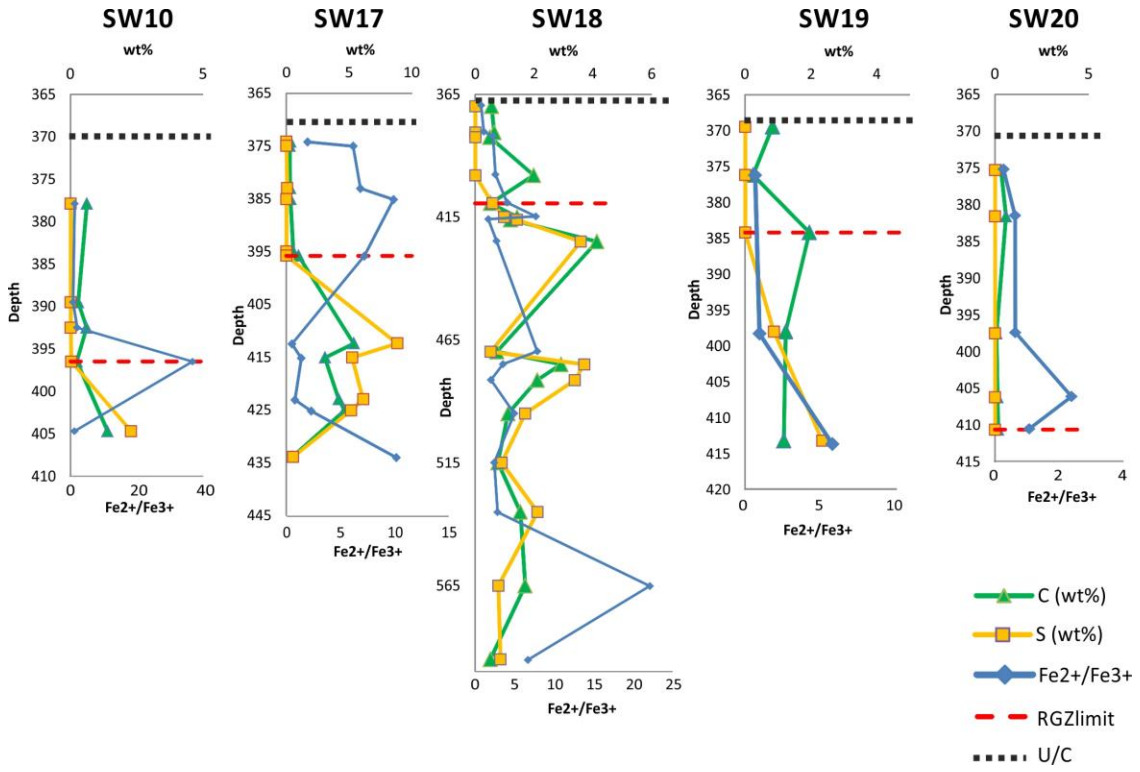

Figure 2-9. C and S element variation in wt%, as well as ferrous/ferric iron ratio variations along the studied DDH from Dufferin Lake Zone

Major element geochemistry of samples from the RGZ, including the green zone and the red zone, is quite similar to that of the graphitic pelitic schists. The major element composition of the green zone, in particular, is indistinguishable from the variably graphitic schists (Fig. 2-8). A lower SiO_2 content (down to 20 wt%) and a higher MgO content (up to 16.9 wt%) may be observed in the rocks from the RGZ and is related to the chlorite alteration. Fig. 2-8b shows a positive correlation between Al_2O_3 and K_2O, for graphitic pelitic schists and the green zone whereas samples from the red/green transition zone, the red zone and the bleached zone do not. The transition zone and in particularly the hematite zone, does not show a higher Fe_2O_3 content relative to the other rocks (Table 2-2).

In contrast, the samples from the bleached zone have higher Al_2O_3, K_2O, TiO_2, and Na_2O content (Figs. 2-8 b, c, d). The Na enrichment may result from the possible growth of fine-grained hydrothermal dravite within the clay mineral assemblage. The pelitic schists from the bleached zone are weakly mineralized (U up to 187 ppm) (Fig. 2-8e) with the presence of small amounts of hydrothermal uraninite along fractures. Usually, there is a close relationship between carbon and uranium (Landais 1996), but the bleached zone and the RGZ have been enriched in U content relative to the less altered graphitic pelitic schists (Fig. 2-8e). Also, the samples from the bleached zone have very high boron content (from 30 ppm to 13.100 ppm) (Fig. 2-8f) due to their high dravite content. Thus, the high uranium content and high boron content in the bleached zone appears to be related, although the sample with the highest uranium content (SW19-369.5) is not the one with the highest boron content (SW18-369.9) (Table 2-2 and 2-3).

Samples from the less altered basement rocks, the RGZ, and the bleached zone have very similar chondrite normalized REE patterns (Fig. 2-10), except for one sample that will be described below. They show higher LREE content, with (La/Yb)N varying from 1.2 to 36.9, and a negative Eu anomaly (Fig. 2-10). Furthermore, the HREE/LREE ratio is less than 1 (0.02 to 0.54) (Table 2-4, Appendix F). These observations are typical of the basement alteration halo associated with unconformity-type mineralization (Fayek & Kyser 1997, Mercadier *et al*. 2011). Also, these chondrite-normalized REE patterns, and the presence of a well-pronounced Eu anomaly, are similar to the chondrite-normalized REE distributions found in average post-Archean shales (Condie 1993) and to the graphitic pelitic gneisses of the basal Wollaston Group below the eastern Athabasca Basin (Madore & Annesley 1997).

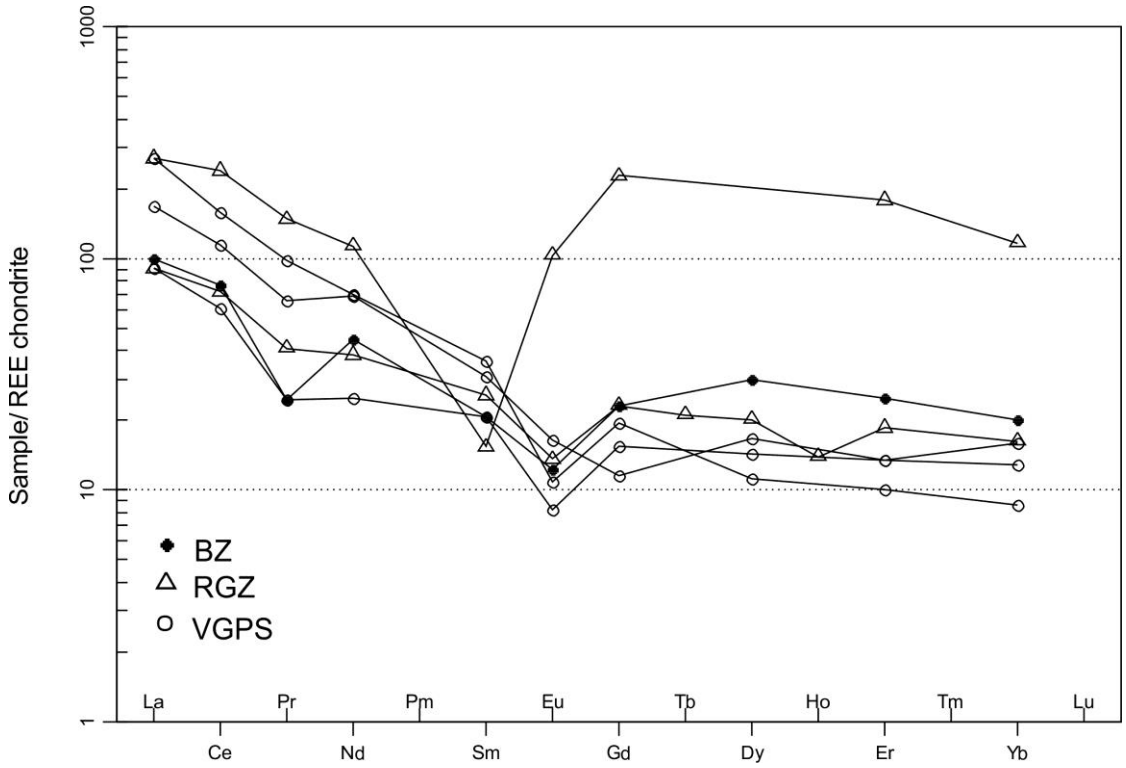

Figure 2-10. Representative chondrite-normalized REE patterns, using the values of Boynton (1984), of samples from the bleached zone (BZ), the red/green zone (RGZ) and the variably graphitic pelitic schists (VGPS)

The highest concentrations of the HREE are observed in one sample from the RGZ with the REE pattern differing with almost up to ten times more HREE than the other patterns. This may be related to the presence of xenotime. LREE abundance could be due to aluminium–phosphate–sulphates (APS) phases (Mercadier *et al*. 2011). Usually, the samples from the bleached zone and the RGZ have a slightly higher HREE content than the variably graphitic pelitic schists (Table 2-4).

Table 2-2. Major and trace elements geochemistry of the graphitic and graphite-depleted rocks

Name	DF60	SW10	SW10	SW10	SW17	SW17	SW17	SW17	SW19	SW19	SW19	SW19	SW20	SW20	SW20	SW20
Depth	384.2	389.5	392.5	396.5	385.1	395	412.4	415.1	369.5	376.2	384.2	413.2	375.3	381.6	397.5	406.2
Zone	VGPS	RZ	RGZ	GZ	GZ	GZ	VGPS	VGPS	BZ	RGZ	GZ	VGPS	BZ	RGZ	RGZ	GZ
wt%																
SiO_2	59.5	67.1	51	65.9	56.2	55.1	37.5	56.3	43.7	65.8	57.9	50.8	46.5	65.1	55.7	62.2
TiO_2	0.9	0.48	0.63	0.37	0.94	0.55	0.55	0.52	1.56	0.88	0.73	0.61	1.15	0.55	0.88	0.87
Al_2O_3	14.9	11.2	16.8	10.6	21.4	13.3	12	12.7	35.7	19	15.8	15.1	33.1	13.7	22.5	19.2
Fe_2O_3	7.42	6.7	11	12.5	6.07	11.2	26	12.8	1.9	1.61	8.71	18.4	2.13	4.96	3.27	3.91
MnO	0.06	0.07	0.07	0.12	0.05	0.09	0.09	0.07	0.01	<0.01	0.04	0.11	0.01	0.04	<0.01	<0.01
MgO	5.68	7.43	11.8	5.67	4.6	10	6.52	3.8	4.76	4.87	4.7	6.26	5.62	6.47	7.96	4.95
CaO	0.1	0.09	0.16	0.34	0.14	1.28	0.7	0.67	0.09	0.04	0.32	0.18	0.07	1.29	0.1	0.06
Na_2O	0.09	0.02	0.02	0.02	0.22	0.07	0.03	0.11	0.66	0.15	0.15	0.06	0.49	0.09	0.1	0.15
K2O	2.3	0.18	0.14	0.1	5.32	0.63	0.17	1.88	5.41	3.17	3.01	1.25	5.36	2.02	1.98	3.82
P_2O_5	0.04	0.04	0.05	0.14	0.07	0.87	0.44	0.56	0.14	0.05	0.04	0.13	0.04	0.16	0.21	0.03
LOI	9.2	5.6	8.5	4.4	5.1	6.4	16.6	9.7	5.9	5.2	8.9	7.2	5.5	6.1	7.5	5.0
Total	100.19	98.91	100.17	100.16	100.11	99.49	100.6	99.11	99.83	100.77	100.3	100.1	99.97	100.48	100.2	100.19
Fe2O3 calc.	0.45	3.30	3.38	0.33	0.56		17.71	5.50		0.97		2.73	1.65	3.02	1.98	1.15
FeO	6.27	3.06	6.86	10.95	4.96		7.46	6.57		0.58		14.1	0.43	1.75	1.16	2.48
Fe^{2+}/Fe^{3+}	15.45	1.03	2.26	36.83	9.91		0.47	1.33		0.67		5.75	0.29	0.65	0.65	2.39
C	4.84	0.29	0.61	0.24	0.34	0.56	5.37	3.08	0.84	0.25	1.96	1.18	0.33	0.59	0.08	0.14
S	0.43	0.01	0.01	0.03	0.01	0.01	8.84	5.25	0.01	0.01	0.01	2.35	0.01	0.01	0.01	0.01
ppm																
B	344	35	55	36	211	185	120	215	12200	523	302	207	9530	119	642	304
Ba	182	10	3	1	806	145	17	370	683	371	381	197	598	255	181	478
Ga	19	15	26	15	28	23	24	20	52	29	24	18	52	20	21	26
As	104	20	25	<1	2	6	79	175	1	2	<1	15	<1	<1	<1	<1
Cr	276	74	62	102	248	152	82	144	215	153	106	99	193	74	167	144
V	224	78	87	96	132	190	245	151	197	127	127	115	190	96	105	167

Name	DF60	SW10	SW10	SW10	SW17	SW17	SW17	SW17	SW19	SW19	SW19	SW19	SW20	SW20	SW20	SW20
Depth	384.2	389.5	392.5	396.5	385.1	395	412.4	415.1	369.5	376.2	384.2	413.2	375.3	381.6	397.5	406.2
Zone	VGPS	RZ	RGZ	GZ	GZ	GZ	VGPS	VGPS	BZ	RGZ	GZ	VGPS	BZ	RGZ	RGZ	GZ
Li	201	91	171	170	116	144	206	83	41	75	83	164	38	93	142	80
Ni	99	161	318	120	53	92	253	87	44	84	61	85	66	113	82	51
Co	45	39	75	36	33	21	178	65	18	23	24	31	26	50	6	7
Cu	67	4	118	59	3	3	84	14	31	<1	6	10	21	6	6	9
Be	2.1	1.6	2.9	2.4	2.6	4.2	2.8	1.4	8.4	2	2.1	2.6	6.9	2.6	2.6	2.1
Sc	17	11	9	10	25	9	11	12	31	19	15	13	27	12	16	19
Zr	118	95	135	83	138	105	127	104	270	141	161	90	216	114	143	154
Sr	24	51	14	27	86	21	14	16	320	106	103	19	73	20	102	35
Y	21	38	38	53	38	29	28	21	41	16	40	25	22	16	461	24
Pb	13	11	9	10	21	22	38	27	56	12	10	15	18	11	11	20
Nb	9	9	11	8	5	10	14	7	17	10	8	9	16	6	8	10
Mo	11	<1	<1	<1	<1	1	11	3	<1	<1	<1	1	<1	<1	<1	<1
Ag	<0.2	<0.2	0.5	0.6	<0.2	<0.2	2	0.2	1.3	0.5	0.4	<0.2	0.6	0.3	0.3	0.3
Cd	1	1	1	1	1	1	2	1	2	1	1	2	2	1	1	1
Sn	6	5	5	5	6	<1	8	9	9	6	6	5	8	4	4	7
Hf	3	4	4	2	4	3	3	2	7	4	5	8	6	4	4	5
Ta	<1	<1	<1	<1	<1	<1	<1	<1	1	<1	<1	<1	<1	<1	<1	<1
W	<1	<1	<1	<1	<1	5	6	2	<1	<1	<1	<1	<1	<1	<1	<1
Bi	1	<1	6	15	<1	4	138	27	<1	<1	7	5	2	2	<1	2
Th	8	9	8	10	11	10	14	10	19	9	9	7	17	6	16	10
U	37	15	11	2	5	14	6	7	187	20	5	<2	18	11	<2	<2
Zn	80	64	156	191	97	171	263	114	32	30	36	62	28	22	15	23

BZ: Bleached zone, RZ: Red zone, RGZ: Red/green zone, GZ: Green zone, VGPS: Variably graphitic pelitic schist

Table 2-3. Geochemical data of major and trace elements, and density measurements of samples used for mass-balance calculations

Name	SW18	SW18	SW18	SW18	SW18	SW18	SW18	SW18	SW18	SW18	SW18	SW18	SW18	SW18	SW18
Depth	369.9	380.6	382.5	398	409.4	415	416.1	425	475	481.4	495	515	535.1	565.1	595.1
Zone	BZ	RGZ	RGZ	RGZ	GZ	VGPS	VGPS	VGPS	VGPS	VGPS	VGPS	VGPS	VGPS	VGPS	VGPS
Density	2.78	2.72	2.69	2.97	2.74	2.82	2.78	2.77	2.84	2.83	2.8	2.77	2.79	2.84	2.8
wt%															
SiO2	52	45.7	59.5	43	66.4	58.9	58.5	58.3	49.7	45.1	59.6	70.3	56.9	59.9	57
TiO2	0.91	0.73	0.61	0.35	0.72	0.83	0.85	0.65	0.78	0.89	0.71	0.59	0.76	0.72	0.76
Al2O3	28.8	18.8	13.9	9.05	16.4	18.3	18.7	16.9	17.9	20.8	17.2	14.6	19.3	17	21.1
Fe2O3	2.85	7.67	6.57	24.7	5.48	8.18	8.35	8.25	13.8	14.2	9.49	4.14	8.48	8.84	7.95
MnO	<0.01	0.1	0.05	0.19	0.07	0.1	0.1	0.07	0.12	0.11	0.09	0.03	0.1	0.11	0.06
MgO	9.04	16.9	11.4	9.98	2.64	3.4	3.09	1.95	4.51	4.5	3.53	1.87	3.44	3.43	3.1
CaO	0.13	0.14	0.29	1.12	0.05	0.14	0.12	0.26	0.14	0.14	0.14	0.12	0.17	0.18	0.16
Na2O	0.73	0.03	0.03	0.03	0.18	0.2	0.2	0.19	0.12	0.16	0.15	0.22	0.2	0.17	0.37
K2O	0.18	0.21	0.19	0.17	3.72	4.01	4.12	4.52	3.21	4.23	3.7	3.82	4.25	3.3	4.55
P2O5	0.1	0.04	0.11	0.46	<0.01	0.1	0.08	0.13	0.11	0.1	0.1	0.06	0.14	0.16	0.12
LOI	6.1	10.6	7.6	10.9	4.2	5.9	6.0	9.3	9.5	9.0	6.0	4.1	6.8	5.8	5.1
Total	100.84	100.92	100.25	99.95	99.86	100.06	100.11	100.52	99.89	99.23	100.71	99.85	100.54	99.61	100.27
Fe2O3 calc.	1.64	3.69	2.02	6.97	1.09	0.95	3.15	2.24	3.06	4.77	1.60	1.22	2.22	0.38	1.04
FeO	1.09	3.58	4.09	15.95	3.95	6.51	4.68	5.41	9.66	8.49	7.1	2.63	5.63	7.61	6.22
Fe^{2+}/Fe^{3+}	0.74	1.08	2.25	2.55	4.04	7.67	1.66	2.69	3.51	1.99	4.95	2.41	2.82	22.14	6.68
C	0.56	0.65	0.5	1.99	0.53	1.43	1.21	4.14	2.92	2.11	1.12	0.78	1.54	1.7	0.52
S	0.01	0.01	0.01	0.01	0.59	0.99	1.42	3.59	3.71	3.39	1.7	0.9	2.12	0.79	0.86
ppm															
B	13100	148	142	35	143	88	216	32	562	387	190	140	205	175	39
Ba	15	9	6	<1	609	608	605	815	358	527	558	678	619	521	619
Ga	41	28	21	23	23	24	27	24	25	30	24	18	26	22	27
As	8	2	21	108	29	20	19	4	72	62	33	83	17	23	8
Cr	234	115	87	48	131	207	136	175	246	151	213	168	209	212	189
V	130	151	109	168	104	114	134	296	211	188	138	99	145	137	131
Li	92	412	256	146	57	73	105	45	109	76	81	36	63	65	71
Ni	389	565	220	201	63	67	56	69	113	97	69	44	57	40	49

Name	SW18	SW18	SW18	SW18	SW18	SW18	SW18	SW18	SW18	SW18	SW18	SW18	SW18	SW18	SW18
Depth	369.9	380.6	382.5	398	409.4	415	416.1	425	475	481.4	495	515	535.1	565.1	595.1
Zone	BZ	RGZ	RGZ	RGZ	GZ	VGPS	VGPS	VGPS	VGPS	VGPS	VGPS	VGPS	VGPS	VGPS	VGPS
Density	2.78	2.72	2.69	2.97	2.74	2.82	2.78	2.77	2.84	2.83	2.8	2.77	2.79	2.84	2.8
Co	90	120	86	148	35	24	28	36	50	42	27	29	27	17	14
Cu	167	56	18	16	11	194	251	258	74	16	54	14	14	80	23
Be	13.2	6.5	4.6	3.3	1.5	2	1.6	1.8	2.5	1.5	2	1.7	1.7	1.7	1.8
Sc	26	19	13	12	18	18	18	20	21	20	17	11	18	16	18
Zr	166	171	133	69	118	130	151	123	131	123	114	145	125	102	154
Sr	225	48	46	35	19	25	31	28	24	31	31	28	45	27	49
Y	54	54	38	49	15	14	17	33	21	15	18	12	26	19	18
Pb	26	10	10	8	17	11	16	21	14	23	12	17	15	9	13
Nb	12	14	11	8	7	4	10	12	9	11	6	7	5	4	6
Mo	<1	<1	<1	<1	<1	<1	1	16	5	2	4	2	2	1	<1
Ag	0.8	0.4	0.4	<0.2	0.6	<0.2	0.6	<0.2	0.2	<0.2	<0.2	<0.2	<0.2	<0.2	<0.2
Cd	1	1	1	2	1	1	1	1	2	2	1	1	1	1	1
Sn	6	4	4	3	6	7	8	8	7	6	7	7	4	5	7
Hf	5	5	4	2	3	3	4	3	3	8	3	4	3	3	4
Bi	2	3	5	12	<1	<1	<1	<1	<1	5	2	7	<1	<1	1
Th	18	14	12	9	9	10	11	12	12	10	10	10	11	8	13
U	65	5	21	12		3		9	7	2	6	4	5	4	4
Zn	81	58	44	237	74	79	119	50	101	92	66	61	90	115	115
La	31	30	29	55	20	32	36	52	32	26	46	9	54	28	32
Ce	62	52	57	97	46	63	70	92	75	49	83	18	104	58	61
Pr	3	3	4	9	2	4	6	8	5	3	6	<1	8	4	4
Nd	27	22	24	34	19	26	29	41	31	19	30	5	41	22	25
Sm	4	4	5	2	4	4	2	6	5	2	4	<1	5	3	3
Eu	0.9	1.1	1.1	1	0.6	0.8	0.9	1.2	1.2	0.6	0.9	0.3	1.3	0.9	0.9
Gd	6	7	6	10	3	1	5	3	<1	3	<1	<1	2	<1	1
Dy	9.7	8.1	6.1	8.1	2.7	2.7	3.4	5.4	4.3	3	3.5	1.9	4.4	3.6	3.1
Er	5.2	5.2	3.6	4.3	1.8	1.3	2.2	2.8	2	3.3	1.8	1.1	2.1	1.8	1.6
Yb	4.2	4.8	3	4.2	1.8	1.6	1.9	3.3	2.5	1.9	2	1.3	2.2	2	1.9

BZ: Bleached zone, RZ: Red zone, RGZ: Red/green zone, GZ: Green zone, VGPS: Variably graphitic pelitic schist

Table 2-4. Rare Earth Elements geochemistry of the graphitic and graphite-depleted rocks

Samples	Zone	La *(ppm)*	Ce	Pr	Nd	Sm	Eu	Gd	Tb	Dy	Ho	Er	Yb	Total REE	LREE	HREE	HREE/ LREE
DF60-384.2	VGPS	15	30	1	12	1	0.4	<1	<1	3.4	<1	1.8	2.1	66.7	59.4	7.3	0.12
SW10-389.5	RZ	60	112	11	50	8	1.8	7	<1	6.8	2	4.7	3.2	266.5	249.8	16.7	0.07
SW10-392.5	RGZ	28	58	5	23	5	1	6	1	6.5	1	3.9	3.4	141.8	126	15.8	0.13
SW10-396.5	GZ	43	77	8	31	4	1.3	8	1	8.9	1	4.8	4.2	192.2	172.3	19.9	0.12
SW17-385.1	GZ	52	92	5	29	3	0.8	2	<1	5.6	1	3.2	3.4	197	183.8	13.2	0.07
SW17-395	GZ	5	15	<1	9	3	0.9	<1	<1	5	1	2.5	2.9	44.3	32.9	11.4	0.35
SW17-412.4	VGPS	66	137	15	54	9	1	9	<1	5.9	1	3	3.1	304	291	13	0.04
SW17-415.1	VGPS	9	19	<1	7	1	0.3	<1	<1	3.7	<1	1.8	2	43.8	36.3	7.5	0.21
SW19-369.5	BZ	115	193	24	106	8	3	12	2	8.7	1	5	3.1	480.8	461	19.8	0.04
SW19-376.2	RGZ	47	99	9	49	8	1.6	5	<1	2.8	1	3.2	1.6	227.2	218.6	8.6	0.04
SW19-384.2	GZ	59	95	14	59	1	1.9	9	1	6.9	1	3.8	3.2	254.8	238.9	15.9	0.07
SW19-413.2	VGPS	35	68	6	29	4	0.9	4	<1	4.7	1	3.6	2.7	158.9	146.9	12	0.08
SW20-375.3	BZ	22	31	1	17	46	0.6	3	<1	3.7	<1	3.1	2.7	130.1	120.6	9.5	0.08
SW20-381.6	RZ	9	18	<1	9	17	0.6	4	<1	3.2	<1	1.7	1.5	64	57.6	6.4	0.11
SW20-397.5	RGZ	84	194	18	68	3	7.6	59	13	88	15	37.5	24.4	611.5	433.6	177.9	0.41
SW20-406.2	GZ	21	44	2	19	1	1.1	5	<1	4.1	<1	2.8	2.3	102.3	93.1	9.2	0.10

BZ: Bleached zone, RZ: Red zone, RGZ: Red/green zone, GZ: Green zone, VGPS: Variably graphitic pelitic schist, LREE=La+Ce+Pr+Nd+Sm+Eu+Gd, HREE= Tb+Dy+Ho+Er+Yb

Mass-Balance Calculations

Mass-balance calculations, using the Grant method (Grant 1986), were carried out to determine the geochemical gains and loss between the rocks depleted in graphite and the original host graphitic pelitic rocks. Elements that remain immobile during fluid-rock interactions plot on a line called an isocon, which gives the relation between the altered rock and the unaltered rock compositions. Element concentrations plotting above the isocon line indicate enrichment in the altered rock relative to the immobile element, and depletion if they plot below the isocon. Isocons can also be determined based on constant mass or volume. The slope variation of the isocon reflects either a change in concentration, or mass, and hence volume in the alteration (Grant 1986). The determination of the density of the rocks is useful in the determination of the mass and volume changes. There are significant variations of density between the graphitic pelitic schists, the RGZ and the bleached zone. The graphitic pelitic schists have higher densities than the rocks from the RGZ and the bleached zone, varying between 2.77 and 2.84 g/cc. The rocks in the RGZ have densities between 2.69 and 2.74 g/cc, although sample (SW18-398) has an anomalous high density of 2.97 g/cc but contains abundant and dense specular hematite (Table 2-3). The density for the sample from the bleached zone is 2.78 g/cc. The gains and losses are expressed in wt% for major elements or ppm for trace elements, and representative examples are shown in Fig. 2-11 and Table 2-5.

Table 2-5. Representative mass-balance calculations for the comparison of the variably graphitic pelitic schists (VGPS) with the bleached zone (BZ) (a), and the red/green zone (RGZ) (b)

a)

Sample	Unaltered VGPS SW18-535	Altered BZ SW18-369.9	Gain/Loss in wt.% or ppm ΔC_i	% changes
wt%				
SiO2*0.1	5.69	5.20	-0.51	-8.61
TiO2*10	7.60	9.10	1.47	+19.74
Al2O3*0.1	1.93	2.88	0.94	+49.22
Fe2O3	8.48	2.85	-5.64	-66.39
MnO*10	1.00			
MgO	3.44	9.04	5.57	+162.79
CaO*10	1.70	1.30	-0.40	-23.53
Na2O*10	2.00	7.30	5.27	+265.00
K2O	4.25	0.18	-4.07	-95.76
P2O5*10	1.40	1.00	-0.40	-28.57
C	1.54	0.56	-0.98	-63.64
S	2.12	0.01	-2.11	-99.53
ppm				
Ba*0.01	6.19	0.15	-6.04	-97.58
Co*0.1	2.70	9.00	6.27	+233.33
Cr*0.01	2.09	2.34	0.24	+11.96
Cu*0.1	1.40	16.70	15.24	+1092.86
Ga*0.1	2.60	4.10	1.49	+57.69
Hf	3.00	5.00	1.98	+66.67
Li*0.1	6.30	9.20	2.87	+46.03
Nb	5.00	12.00	6.96	+140.00
Ni*0.01	0.57	3.89	3.31	+582.46
Pb	15.00	26.00	10.91	+73.33
Sc	18.00	26.00	7.91	+44.44
Th	11.00	18.00	6.94	+63.64
U*0.1	0.50	6.50	5.98	+1200.00
V*0.1	14.50	13.00	-1.55	-10.34
Y*0.1	2.60	5.40	2.78	+107.69
Zn*0.1	9.00	8.10	-0.93	-10.00
Zr*0.1	12.50	16.60	4.04	+32.80
La*0.1	5.40	3.10	-2.31	-42.59
Ce*0.1	10.40	6.20	-4.22	-40.38
Nd*0.1	4.10	2.70	-1.41	-34.15
Sm	5.00	4.00	-1.01	-20.00
Dy	4.40	9.70	5.27	+120.45
Er	2.10	5.20	3.08	+147.62
Yb	2.20	4.20	1.98	+90.91
B*0.001	0.21	13.10	12.85	+6138.10

b)

Sample	Unaltered VGPS SW18-535	Altered RGZ SW18-382.5	Gain/Loss in wt.% or ppm ΔC_i	% changes
wt%				
SiO2*0.1	5.69	5.95	0.05	+4.57
TiO2*10	7.60	6.10	-1.72	-19.74
Al2O3*0.1	1.93	1.39	-0.59	-27.98
Fe2O3	8.48	6.57	-2.15	-22.52
MnO*10	1.00	0.50	-0.52	
MgO*0.1	0.34	1.14	0.76	+235.29
CaO*10	1.70	2.90	1.10	+70.59
Na2O*10	2.00	0.30	-1.71	-85.00
K2O	4.25	0.19	-4.07	-95.53
P2O5*10	1.40	1.10	-0.34	-21.43
C	1.54	0.50	-1.06	-67.53
S	2.12	0.01	-2.11	-99.53
ppm				
Ba*0.01	6.19	0.06	-6.13	-99.03
Co*0.1	2.70	8.60	5.59	+218.52
Cr*0.01	2.09	0.87	-1.25	-58.37
Cu	14.00	18.00	3.35	+28.57
Ga*0.1	2.60	2.10	-0.58	-19.23
Hf	3.00	4.00	0.86	+33.33
Li*0.01	0.63	2.56	1.84	+306.35
Nb*0.1	0.50	1.10	0.56	+120.00
Ni*0.01	0.57	2.20	1.55	+285.96
Pb	15.00	10.00	-5.36	-33.33
Sc	18.00	13.00	-5.47	-27.78
Th	11.00	12.00	0.57	+9.09
U*0.1	0.50	2.10	1.52	+320.00
V*0.1	14.50	10.90	-3.99	-24.83
Y*0.1	2.60	3.80	1.06	+46.15
Zn*0.1	9.00	4.40	-4.76	-51.11
Zr*0.1	12.50	13.30	0.32	+6.40
La*0.1	5.40	2.90	-2.60	-46.30
Ce*0.1	10.40	5.70	-4.90	-45.19
Nd*0.1	4.10	2.40	-1.79	-41.46
Sm	5.00	5.00	-0.18	0.00
Dy	4.40	6.10	1.48	+38.64
Er	2.10	3.60	1.37	+71.43
Yb	2.20	3.00	0.69	+36.36
B*0.01	2.05	1.42	-0.68	-30.73

TiO_2 has already been considered as immobile element in the eastern Athabasca Basin (Mercadier *et al.* 2011, Lorilleux *et al*. 2003), and in the rocks within the study area, TiO_2 shows the least variation, and it appears to represent a relatively immobile element oxide. Thus, the calculated gain and loss of an element relative to the TiO_2 content of the rocks represents an isocon. The position of this isocon, based on TiO_2, is clearly distinct from the other isocons corresponding to either constant mass (CM) or constant volume (CV). In the RGZ, a significant gain in mass and volume was noted (Figs. 2-11c, d), whereas in the bleached zone, a loss in mass and volume is observed (Figs. 2-11e, f). In the green zone, a slight gain in mass and volume is observed but is not significant. The variation between the isocon traced using TiO_2, and the CM and CV isocons does not really cause much variation in the elements that appear to be gained or lost, except when comparing the RGZ and the bleached zone. Thus, the gains and losses of elements are described relative to the isocon based on TiO_2.

Mass-balance calculations confirm the loss of carbon and sulfur in the RGZ, including the green zone, and the bleached zone relative to the variably graphitic pelitic schists (Figs. 2-11a, c, e), and a large gain of boron in the bleached zone (Fig. 2-11f), compared to an insignificant variation in the RGZ (Fig. 2-11d) and the green zone.

The lower part of the RGZ, *i.e.* the green zone, does not show many significant variations in the element concentrations compared to the variably graphitic pelitic schists (Figs. 2-11a, b). Some variations include loss of Fe_2O_3, MgO, CaO, C and S, and a slight gain of SiO_2 (Fig. 2-11a). Trace elements also do not show many significant variations, except for depletion in V, Th, Zn, LREE, with slight HREE loss, and slight gain in Pb, Nb and Co (Fig. 2-11b).

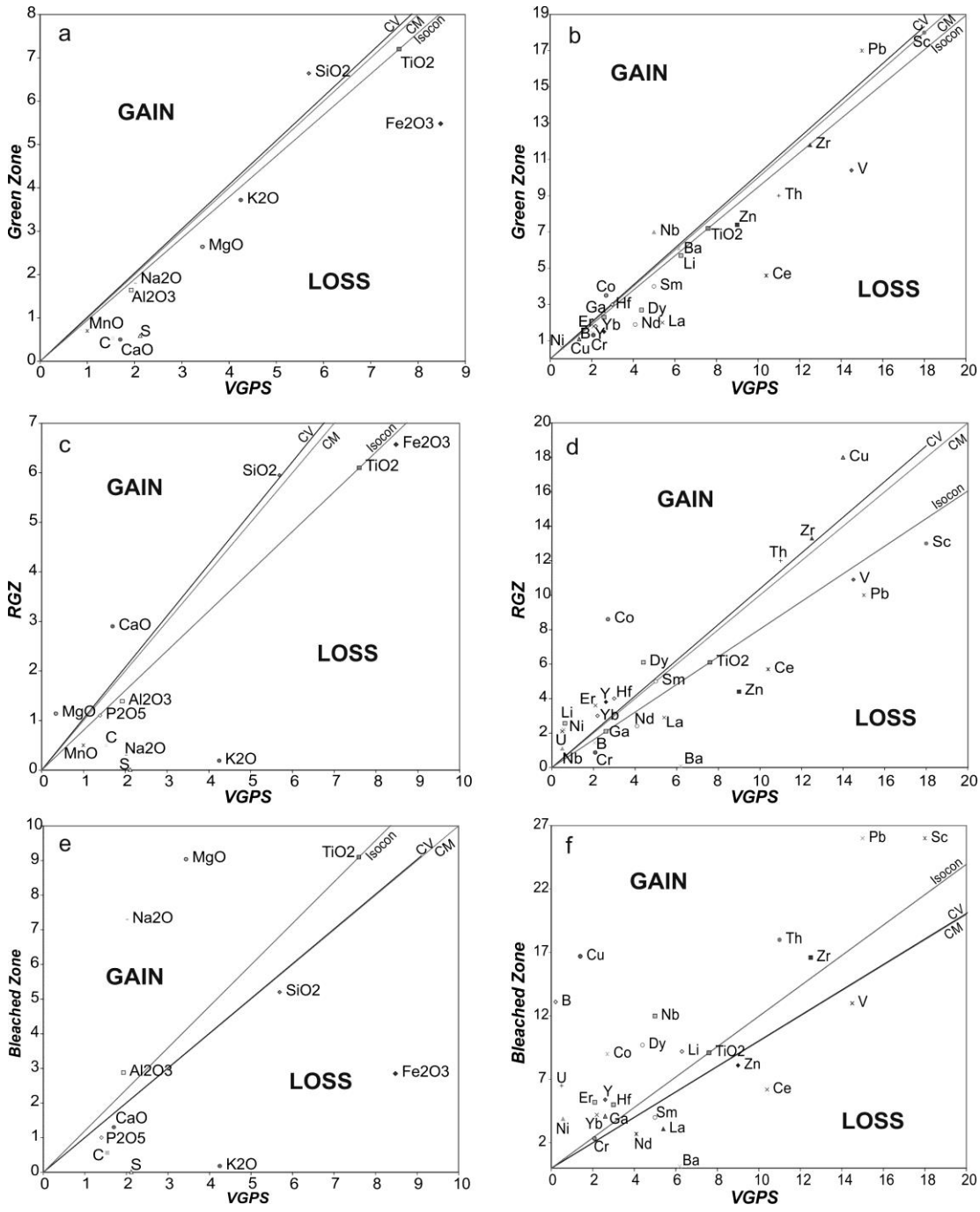

Figure 2-11. Isocon diagrams showing mass-balance calculations performed between least altered rocks from the variably graphitic pelitic schists (VGPS; SW18-535.1) and rocks from (a-b) the green zone (SW18-409.4), (c-d) the middle part of the red/green zone (RGZ; SW18-382.5), and (e-f) the bleached zone (SW18-369.9). The concentration of some component was multiply by a convenient factor for both the unaltered and altered rock, with a different factor for each component, to be represented in the graph. The major (a-c-e) and trace (b-d-f) elements are shown by weight percent and ppm, respectively. CV and CM represent constant volume and constant mass, respectively

However, the middle part of the RGZ shows more significant variations with the variably graphitic pelitic schists (Figs. 2-11c, d). Major elements such as K_2O and Na_2O are significantly lost relative to TiO_2 as well as C and S, and enrichment in SiO_2, CaO and MgO is observed (Fig. 2-11c). A gain in mass and volume is also observed and can be related to a gain in SiO_2 (Figs. 2-11c), as discussed below. The trace elements show significant losses in Zn, Ba and LREE (except for Sm) and significant gains in Cu, Th, Zr, Co, Li, HREE and U (Fig. 2-11d) relative to TiO_2.

The bleached zone is the zone which shows the most significant variations when compared to the other zones (Figs. 2-11e, f). Compared to the variably graphitic pelitic schist, this zone shows significant gains of Na_2O and MgO and depletions of Fe_2O_3, K_2O, SiO_2, C and S (Fig. 2-11e). The loss in mass and volume can be due to the loss of SiO_2, in contrast to the RGZ (Fig. 2-11e). Trace elements show significant variations as well with significant gains in B, Cu, Th, Co, HREE and U, for example. The most significant losses include V, Zn, Ba and LREE (Fig. 2-11f). The bleached zone overprints the RGZ and is therefore a younger alteration event. This alteration resulted in an enrichment of Na_2O, B, Cu and U, and a loss of Fe_2O_3, SiO_2 and CaO, compared to the RGZ.

Discussion

In this study, we examined graphite-bearing pelitic rocks and their equivalents that have been depleted in graphite and sulfides below uranium mineralization in the Dufferin Lake Zone, south-central Athabasca Basin. The aim was to characterize the different types of carbon species present in the rocks, and to provide constraints on the processes that may have led to the consumption of graphite (and sulfides) in the basement rocks underlying uranium mineralization.

Origin of Graphitic Species

The graphitic species concentrated in the matrix of the basement pelitic schists were likely derived from organic-rich black shale (Madore & Annesley 1997, Wilson *et al*. 2007) by the process of graphitization (Wopenka & Pasteris 1993, Beyssac *et al*. 2002a, Crespo *et al.* 2004, Ray 2009). This transformation is the result of the metamorphism of organic material present in the rock, resulting in formation of highly ordered graphite (Luques *et al.* 2012). The crystallinity of the resulted graphite depends on the metamorphic grade (temperature, pressure) and type of carbon precursor (Beyssac *et al*. 2002a, Nover *et al*. 2005) as well as strain and time (Nover *et al.* 2005). Graphite located along fault zone can also be the result of precipitation from saturated carbon-bearing fluids such as CO_2, CO, and CH_4 (Wopenka & Pasteris 1993, Crespo *et al*. 2004, Ray 2009), resulting from the following suggested precipitation reactions:

$CH_4 = C + 2H_2$

$CH_4 + CO_2 = 2C + 2H_2O$

and $CO_2 + 2H_2 = C + 2H_2O$ (Luque *et al*. 1998, Ortega *et al*. 2010). These reactions result in graphite with high crystallinity (Luque *et al*. 2012).

Graphite Geothermometry and Constraints on PT-t Path

The presence of graphite in a mineral assemblage provides an additional constraint on the conditions of temperature and pressure in which the assemblage formed (French 1966). Raman analyses is used as geothermometer (Pasteris & Wopenka 1991, Wopenka & Pasteris 1993, Yui *et al*. 1996, Beyssac *et al.* 2002a, 2002b) to determine the peak metamorphic temperature, because the graphitization process is assumed to be irreversible, as there is apparently no effect on carbonaceous material during retrograde metamorphism. Temperature can be estimated to +/- 50°C in the range 330–650°C. More specifically, metamorphic temperatures have been

calculated using the R2 parameter after the equation from Beyssac *et al*. (2002a), and R1 and R2 ratios after the equation of Rahl *et al.* (2005). Thus, the temperature can be estimated using these equations:

(1) T(°C) = -445R2 + 641 and

(2) T(°C) =737.3 +320.9R1 – 1067R2 – 80.638 R12

after Beyssac *et al*. (2002a) and Rahl *et al*. (2005), respectively. By applying equation (1), the temperatures obtained from graphite in the graphitic pelitic schists varies from 388 to 515 +/-50 °C, whereas the temperatures obtained from graphitic particles in the RGZ vary between 221 and 398 +/-50°C. Equation (2) gives temperatures between 241 and 529 +/-50°C for the graphitic pelitic schists and between 339 and 403 +/-50°C for samples from the RGZ.

The second equation is thought to provide more accurate calculations in lower temperature (down to 100°C) metamorphic rocks (Rahl *et al*. 2005), compared to the equation from Beyssac *et al*. (2002a). Lower temperatures have been determined for the samples from the RGZ, compared to those from the graphitic pelitic schists. The latter are interpreted as preserving metamorphic temperatures in the basement rocks in the DLZ; with the highest temperatures being recorded within the least altered samples. Similar temperatures of 500-550°C have been determined in Hearne province rocks to the east of the present study area, but are interpreted as retrograde temperatures along metamorphic P–T paths constructed for the western margin of the Trans-Hudson Orogeny (Orrell *et al*. 1999, Annesley *et al*. 2005) at pressures estimated to be 200–250 MPa.

The temperatures deducted from the equations (1) and (2) suggest that the peak metamorphic temperature is about 530 +/-50°C, indicating that the rocks in the Dufferin Lake Zone have undergone peak metamorphism in amphibolite facies. Moreover, petrographic observations show

strongly altered garnet, staurolite, and andalusite, replaced by quartz and/or clay minerals, even in the least altered graphitic pelitic schists. This suggests that the system has been totally altered under greenschist-facies conditions. These results allow the determination of the retrograde part of a P-T-t path (Fig. 2-12). The basement rocks were exposed at surface to allow the development of a paleoweathering profile (star in Fig. 2-12), prior to burial as the Athabasca Basin started to fill at about 1750 Ma (Fig. 2-12).

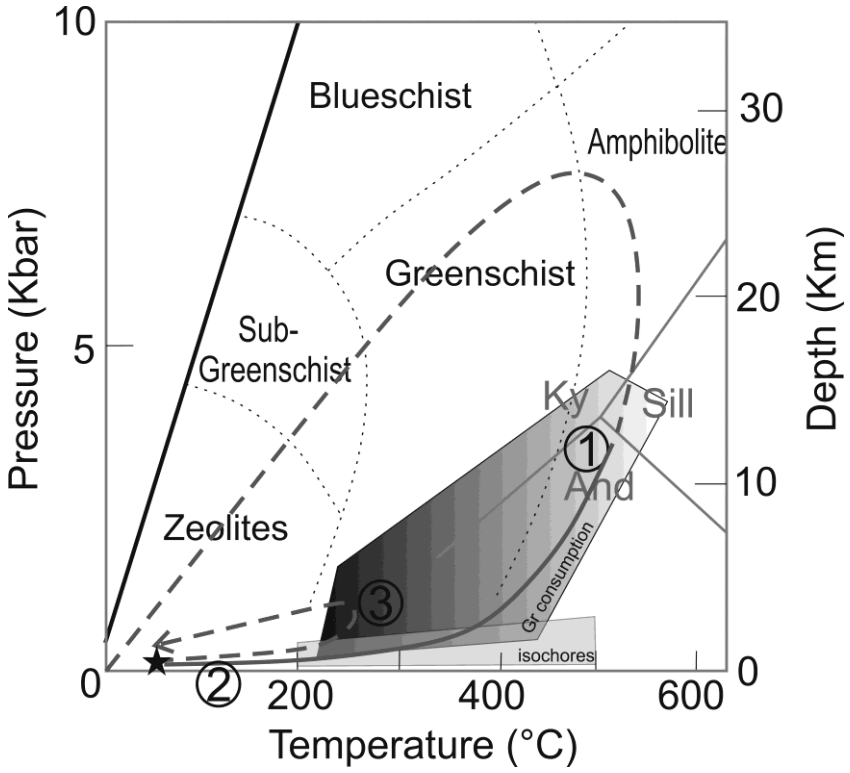

Figure 2-12. Pressure - Temperature diagram with the pathway of the conditions of pressure and temperature determined from the observations of this study is represented. The upper dashed line represents the hypothetical prograde part of the PT path. The lower dashed line represents the reburial and subsequent uplift of the basement rocks after paleoweathering and syn/post Athabasca deposition. The field of fluid inclusions isochores of graphitic pelitic schists (Pascal *et al*. 2013) is shown. The star represents the moment when the basement rocks were at the surface followed by the burial of the rocks due to the deposition of the Athabasca Group leading to an increase in pressure and temperature. This star suggests the initiation of the paleoweathering. Graphite consumption increases with decreasing pressure during retrograde metamorphism, with incipient graphite consumption due to C-O-H fluids during retrograde metamorphism (1) followed by weathering events (2) and basin diagenesis and multiple hydrothermal mineralization events (3)

Graphitic vs. Graphite-Depleted Rocks

The whole-rock composition, and in particular, the REE patterns and Eu anomalies, of the graphitic pelitic schists suggests that they are metamorphosed shales, similar to the post-Archean shales of Condie (1993). Additionally, if we consider the amount of carbon in these rocks (up to 5.37 wt%), then we can interpret them to be black shales, possibly related to the worldwide ca. 2.05 Ga Shunga oxidation event (Cuney 2010). The strongly altered zones immediately below the unconformity (*i.e.* the bleached zone and the different parts of the RGZ) overprint these metamorphosed black shales, based on their textural similarity.

The pelitic schists in the RGZ are texturally similar to the variably graphitic pelitic schists, and have similar major element composition. However, there are differences in mineralogy and loss and gains in elements have been observed, likely related to fluid-rock interaction during the development of the different zones of the RGZ and the bleached zone.

The variably graphitic pelitic schists gradually became altered by chlorite in the green zone at the base of the RGZ. The elemental variations in the green zone, when compared to the graphitic pelitic schists, are less significant than the overlying zones, which may imply less fluid circulation. However, graphite is less common and more amorphous than in the variably graphitic pelitic schists.

Fluids circulating through the middle RGZ introduced MgO, CaO, Na_2O, Fe_2O_3, some metals and Th, but leached out K_2O, C, S, Ba, and Zn relative to TiO_2. The enrichment in CaO could be the result of late crystallization of carbonates, and enrichment in Fe_2O_3 compared to the green zone is associated with the formation of hematite or Fe-bearing chlorite (Fig. 2-5). The gain in mass and volume could be the result of the different quartz vein generations. The gain in MgO could be associated with the formation of Mg-bearing chlorite (Fig. 2-5). This RGZ, which has been historically interpreted to be the result of paleoweathering, is also thought to be the result of

interaction with post-Athabasca hydrothermal fluids, potentially responsible for uranium mineralization (Cuney 2003), as well as later meteoric fluids (Mercadier *et al*. 2011).

The bleached zone is situated just below the unconformity, and consists of clay alteration, dravite, and elevated uranium concentrations. This zone is interpreted to increase in intensity close to hydrothermal uranium mineralization (*e.g*. Macdonald 1985). Bleaching in the Dufferin Lake Zone area is not preferentially associated with fault zones, which suggests that it formed from hydrothermal fluids circulating along and adjacent to the unconformity surface. This bleaching alteration is interpreted to be the equivalent of one or more of the alteration events associated with uranium mineralization in the Athabasca Basin (Macdonald 1980, Mercadier *et al*. 2011). In this zone, higher variations in elements have been observed compared to the RGZ, reflecting the variation of the redox conditions due to the circulation of several fluids. The hydrothermal fluids have brought mainly Na_2O, MgO, B and U, as well as Cu, Th and HREE, among others, whereas SiO_2, Fe_2O_3, K_2O and Ba were leached out. Strong SiO_2 depletion, which is associated with quartz dissolution and resulted in subsequent volume loss, is an indication of major fluid-rock interactions within this zone. This volume loss explains the high TiO_2 and Al_2O_3 content (Fig. 2-8), relative to the RGZ and the variably graphitic pelitic schists. Fe_2O_3 depletion results from hematite leaching, whereas the gain in Mg and B can be associated with the formation of Mg-chlorite (Fig. 2-5) and dravite, respectively. The Na enrichment has been suggested to be the result of the possible growth of fine-grained dravite within the clay mineral assemblage. The quartz dissolution results in an increase of permeability in this zone, allowing enhanced fluid circulation (Lorilleux *et al*. 2003), and related fluid-rock interactions and associated mineralization.

Graphitic and Graphite-Depleted Rocks and their Carbon Species

Petrography, geochemistry and Raman analysis confirmed the presence of carbon species in the graphitic pelitic schists and a loss of carbon in the RGZ and the bleached zones. Also, this study emphasizes the correlation between C and S content.

Variably graphitic pelitic schists

In addition to geochemistry and petrography which show a variable amount of carbon (and sulfur) and carbon species within the variably graphitic pelitic schist, Raman analysis revealed different types of carbon species that are not detectable using only reflected light microscopy. Well-ordered carbon species corresponding to graphite to semi-graphite are present, although the presence of defect bands D1 and sometimes D2 confirms that there are still structural defects. The variation of carbon type could be due to the original chemical composition of the parent material, which may play a role in the type of graphite formed, and recrystallization during later metamorphism (Kribek *et al*. 1994, Kwiecińska & Nowak 1997). Moreover, these rocks record a peak metamorphic temperature in amphibolite facies (up to about 530°C), which is comparable to early retrograde temperatures (500-550°C) from the western margin of the Trans-Hudson Orogeny (Orrell *et al*. 1999, Annesley *et al*. 2005).

Red/green zone

Despite being texturally similar to the variably graphitic pelitic schists, and having similar major element composition, no macroscopic and only rare microscopic carbon species were observed in these rocks, as also suggested by depletion in carbon and associated sulfur. Highly amorphous carbons are the most common carbon species in the RGZ, although Raman analysis revealed the presence of rare semi-graphite to CM. Even in the green zone, which is strongly

chloritic and is interpreted to have preserved more reducing conditions in which graphite may have been preserved, amorphous carbon is the most common carbon species. The presence of rare ordered carbon species in the upper part of the RGZ could be the result of the formation of younger hydrothermal graphite and/or graphite recrystallization. The amorphous carbon observed in the RGZ has not been observed in the underlying graphitic pelitic schists. The amorphous carbon could be interpreted as being the result of recrystallization of original graphite along the retrograde part of the PT-t path (Fig. 2-12), or by graphite consumption and alteration via fluid-rock interactions, both of which led to the formation of a lower crystallinity carbon species.

The textural and major element geochemical similarity between the rocks in the RGZ and in the graphitic pelitic schists indicate that they were originally the same type of rock, and that it was likely that graphite and sulfides were present in the RGZ and then removed by some processes. The relative absence of well-crystallized graphite in the lower part of the RGZ (the green zone) suggests that the transition from graphitic pelitic schists to non-graphitic pelitic schists is sharp, and thus the removal of graphite could not have been related to a gradual process.

Petrography revealed that graphite is mainly absent in the upper RGZ, particularly in areas in which quartz and hematite are common. This could suggest that a silica-rich and/or the oxidized fluid which precipitated hematite could be responsible for the consumption of graphite. The red hematite alteration is interpreted to have occurred during diagenesis (Cuney *et al.* 2003) which suggest that the base of this zone may represent a redox front controlled by the degree of percolation of the oxidized diagenetic brines into the basement (Jefferson *et al.* 2007). This is

confirmed by the Fe^{2+}/Fe^{3+} ratio which shows that the upper RGZ and the bleached zone are oxidized. This is probably the result of the interaction with oxidized basinal brines.

Bleached zone

The bleached zone situated just below the unconformity, which is interpreted to be the end result of several fluid-rock interactions, contains no graphite. The complete lack of graphite might suggest that the fluids that formed the bleached horizon destroyed any graphite that may have still been present.

Mechanism(s) Responsible for Graphite Depletion

The similarities in textures and geochemical composition suggest that graphite was present in all the basement rocks, even those now depleted in graphite and sulfides. Raman analysis indicates the presence of minor quantities of amorphous carbon species in the graphite-depleted rocks of the RGZ. All the graphite-depleted rocks record fluid events leading to the formation of hematite, chlorite, quartz, clay minerals, and dravite in various zones. Overall, there a number of different events that occurred after the peak of metamorphism in the basement that could be related to the consumption of graphite below the unconformity. These include:

- Interaction with C-O-H fluids
- Surficial events, during paleoweathering
- Interaction with an oxidizing fluid from which hematite formed and/or with a silica-rich fluid
- Interaction with diagenetic hydrothermal fluids during U-mineralization

- Or a combination of processes operating during multiple fluid events

Basement-derived C-O-H fluids

Recent thermodynamic modeling indicates that graphite is not inert but reacts, either being consumed or precipitated when C-O-H fluid is present, during retrograde metamorphism (Huizenga 2010, Huizenga & Touret 2012).

Huizenga (2010) explained that the cooling of C-O-H fluids can precipitate or consume graphite depending on a variety of parameters, including mole fractions of components, pressure and temperature in either an open or closed system. In an open system, fluids that have a low atomic O/(O+H) ratio will consume graphite during cooling as a result of the dominant net reactions :

$C+2H_2 = CH_4$

$C+2H_2O = CH_4+O_2$

Cooling combined with decompression of medium- to low-temperature open fluid systems will always result in graphite consumption, (Huizenga 2010). Thus, fluids could have precipitated graphite and then after cooling, consumed graphite during retrograde metamorphism (Fig. 2-12). This would suggest incipient graphite-consumption before the deposition of the Athabasca basin (step 1 - Fig. 2-12), and thus playing no role in uranium mineralization.

Graphite can be partly consumed by water generated during hydration reaction creating CO_2 and CH_4 enriched fluids during retrograde metamorphism (Annesley & Wheatley 2011, Card & Annesley 2012, Ault & Selverstone 2008). Annesley & Wheatley (2011) suggest that graphite/carbon can be consumed and/or precipitated along the retrograde P-T-t path of appropriate basement lithologies from 600°C to 250°C.

CH_4-rich fluid inclusions have been observed in the graphitic pelitic schists, which may have been generated by the breakdown of graphite (Pascal *et al.* 2013). Thus, this C-O-H fluid could then be responsible for precipitation as well as consumption of graphite in the basement, and in the RGZ, along the retrograde part of the P-T-t path.

Surficial events

Before the start of sedimentation in the basin, tropical weathering occurred leading to the formation of a paleoweathering horizon (MacDonald 1980, 1985). Graphite is supposed to be resistant during weathering (Spence 1920) but a small amount of graphite could be consumed by meteoric oxygen-rich water (Landais 1996), using the equation:

$C + 2H_2O = CH_4 + O_2$

or $2C + 2H_2O = CH_4 + CO_2$.

These species could have migrated into the atmosphere as gas species, and then would not be related to uranium mineralization.

Interaction with a silica-rich fluid and/or with an oxidizing fluid from which hematite formed

Petrography indicates the absence of carbon species, especially where hematite and quartz have replaced the pre-existing fabric. Thus an oxidizing and/or silica rich fluid could have interacted with the graphite, resulting in its removal. An oxidizing fluid could have been present during the development of the paleoweathering profile. However, the depletion of graphite is also observed in the green zone, where hematite is not abundant. This suggests that interaction with an oxidizing fluid was not the only event responsible for the depletion of graphite.

There are a number of quartz vein generations in the altered and relatively unaltered basement rocks, and thus graphite loss could have occurred during some of the silicification/quartz vein

events. The earliest quartz vein event occurred during retrograde metamorphism and prior to the initiation of the basin, whereas the two youngest quartz vein events could potentially be related to uranium mineralization (Pascal *et al*. 2013). Graphite depletion occurred after the formation of the earliest quartz veins, but could have also occurred during the formation of the later quartz veins, which leads to the possibility that the consumption of graphite and uranium mineralization are related.

Syn-mineralization fluids

The presence of basinal fluids, considered to be responsible for uranium mineralization, have been recognized in quartz veins in the bleached zone and RGZ (Pascal *et al*. 2013). Similar fluids have been interpreted to be responsible for the development of the bleached zone (Hoeve *et al*. 1980) as well as the red alteration in the RGZ (Cuney *et al*. 2003). In the bleached zone and the RGZ, the intensity of alteration is greater than in the green zone and the underlying graphitic pelitic schists, and carbon species are typically absent meaning that these fluids could be responsible for graphite consumption.

However, the presence of some disordered carbon species in the RGZ and rare well-ordered carbon species could be interpreted as the alteration of ordered-graphite by hydrothermal fluids along fluid conduits, as suggested by Landais & Dereppe (1985). Annesley *et al*. (2001) have also documented an increase in alteration of graphite adjacent to mineralizing conduits.

Combination of processes

Different events over time may have removed graphite in the RGZ and the bleached zone, with the circulation of different fluids altering the basement rocks repeatedly through time. Incipient graphite-consumption before the deposition of the Athabasca basin and before the

weathering event *i.e.* during the uplift, as the result of C-O-H fluids (step 1 in Fig. 2-12), followed by the pre-Athabasca weathering event (step 2 in Fig. 2-12), then proceeding through the post-Athabasca oxidized diagenetic brines, and multiple hydrothermal mineralization events (step 3 in Fig. 2-12). Each of the different fluids is potentially responsible for graphite loss. However, lower temperature fluids with decreasing pressure within major brittle conduits are more conducive to graphite consumption (Ault & Selverstone 2008). Thus, the last step might be the most important in the consumption of graphite. The heterogeneous C-O-H fluids from the basement could also be responsible for graphite loss, by cooling as they approach the unconformity (Huizenga 2010). For example, Annesley & Millar (2011) and Card & Annesley (2012) interpreted four or five major events over ca. 50Ma in the eastern Athabasca Basin that co-precipitated graphite, sulfide and tourmaline, but also some of these events along the lower temperature part of the retrograde PT-t path could also be responsible for the depletion of graphite. Mass-balance calculations also provide evidence for strong fluid circulations in the RGZ and in the bleached zone where graphite is totally missing; confirming that the multiple fluids along the unconformity and possibly related to uranium mineralization could be the ones mainly responsible for consuming graphite. In addition, meteoric fluids are still circulating in the basement rocks along the main structures (Mercadier *et al.* 2011, Alexandre *et al*. 2012), and thus, late meteoric fluid events may also be responsible for some consumption of graphite and/or precipitation of new C species.

Role of Carbon Species in Uranium Mineralization

Graphite, or CH_4 and CO_2 derived from basement graphitic lithologies, have been proposed as a reductant for U^{6+} in the Athabasca Basin (Hoeve & Sibbald 1978, Landais 1996, Alexandre *et*

al. 2005). Other possible species could also have acted as reductant, such as H_2S, H_2 and N_2 (Pascal *et al*. 2013, Yeo and Potter 2010)

Uranium deposits can show spatial relationship with graphitic rocks, and in most deposits mineralization is associated with carbonaceous matter (Hoeve & Sibbald 1978, Landais *et al.* 1993, Landais 1996). However, uranium deposits can also be located in non-graphitic zones, such as in the sandstone at Dufferin Lake Zone (Fig. 2-3a; Jiricka *et al*. 2007). Moreover, graphite is consumed in the alteration of host rocks. Thus, Hoeve & Sibbald (1978) suggested the action of a mobile reductant derived from graphite: CH_4 and/or CO_2. This reductant may result from the interaction of heated diagenetic solutions with graphitic lithologies. The proportion of methane and carbon dioxide generated depends on oxygen fugacity (French 1966). Mineralization may thus have resulted from interaction of reducing methane-bearing solutions and the oxidizing diagenetic solutions. Other studies suggest that graphite alteration could generate the bitumen that is sometimes associated with uranium mineralization (Landais *et al*. 1993).

Thus, graphite alteration and consumption in the upper part of the basement rocks, also observed in other studies (Hoeve & Sibbald 1978, Landais *et al*. 1993, Kyser *et al*. 1989), could be the result of a number of different fluid flow events by forming CO_2 and CH_4 following these equations: $2C + 2H_2O = CH_4 + CO_2$ and/or $2H_2O + CO_2 = CH_4 + 2O_2$, (Hoeve & Sibbald 1978, Kyser *et al*. 1989). Under more oxidizing conditions, water and carbon dioxide will become more important at the expense of methane (French 1966). However, CH_4 (observed in the basement rocks at Dufferin Lake; Pascal *et al.* 2013) would have been able to reduce uranium and precipitate it by migrating or being transported by fluids to the unconformity and above to the sandstone, where uranium mineralization was ultimately precipitated (Fig. 2-3a; Jiricka *et al*.

2007). Examples of migrated organic matter-mineralization relationship have been widely observed in uranium ore deposits (Landais *et al*. 1993, Landais 1996), and CH_4 and CO_2 have been identified in fluid inclusions in sandstone by Derome *et al*. (2003). However, no CO_2-rich fluid inclusions have been observed in the Dufferin Lake Zone, although minor amounts of CO_2 have been detected in fluid inclusions dominated by CH_4 and N_2 (Pascal *et al.* 2013). This suggests that the conditions were more reducing in this area in order to produce more CH_4 relative to CO_2, or that CO_2 has been consumed by another reaction such as precipitation of carbonates, which are observed in the RGZ.

Overall, the consumption of graphite leads to the production of methane or carbon-dioxide, which can act as reductant for uranium precipitation. A fluid pathway in the basement is necessary to allow the carbonic fluids (and gases) to reach and mix with the U bearing oxidized basinal fluids. This is facilitated using ductile/brittle to brittle structures and related damage zones, working as a pathway for fluids and allowing the reductants to migrate upward toward and above the unconformity. Moreover, these graphitic structure are particularly interesting because they are involved in the generation of mobile reductants (CH_4, CO_2), along/within this structural-geochemical pathway where mineralization ultimately forms. Methane might not be the most important parameter in the formation of uranium deposit, however, Aghbelagh and Yang (2014) demonstrated that the presence of CH_4 allows the formation of the deposit faster than without CH_4.

In this study, graphite consumption appears to have resulted in the formation of CH_4 (Pascal *et al*. 2013), following the reaction $2C+3H_2O = H^+ + HCO_3^- + CH_4$, which can have acted as a reductant following the equation $4UO_2^{2+} + 3H_2O + CH_4 = 4UO_2 + HCO_3^- + 9H^+$. Following these reactions and using the equation n = m/M; with n: number of mole, m: mass, M: molar mass, the

quantity of CH_4 can be assumed for the formation of a uranium deposit. Thus, for 1000 kg of U, 14.8 kg of CH_4 is necessary:

n_{UO2} = 1,000,000 / (238+16 x 2) = 3703.70 mol

n_{CH4} = 3703.70 / 4 = 925.93 mol

m_{CH4} = 925.93 x 16 = 14814.81 g = 14.81 kg

For example, for high grade uranium deposits such as McArthur River which hosts 192,085,000 kg of U (Jefferson *et al*. 2007), about 2,846,000 kg of CH_4 is necessary.

Thus, to produce 925.93 mol of CH_4, 2 x 925.93 = 1851.86 mol of C is needed, following the equation $2C+3H_2O = H^+ + HCO_3^- + CH_4$. This means that 1851.86 x 12 = 22.22 kg of C is needed. However, following the equation $C+2H_2 = CH_4$, 925.93 mol of C is needed; meaning that 925.93 x 12 = 11.11 kg of C is needed.

Do we have enough carbon in the basement for the formation of CH_4?

If we estimate a total volume of basement rock at DLZ as 5km long x 0.5km wide x 0.5km deep = 1.25 x 10^{15} cm^3 (volume).

These variably graphitic pelitic rocks (*i.e.* 100% of the original volume), which have an average density of 2.8 g/cm^3, would give a mass of 1.25 x 10^{15} cm^3 x 2.8g/cm^3 = 3.5 x 10^{15} g (*i.e.* 3.5 x 10^{12} kg).

If these graphitic rocks contain on average 5.0 wt% C, then 3.5 x 10^{12} x 5.0 x 10^{-2} = 1.75 x 10^{11} kg of C is available in the area.

If the graphitic rocks contain on average 7.5 wt% C, then 3.5 x 10^{12} x 7.5 x 10^{-2} = 2.6 x 10^{11} kg of C is available in the area.

If 5% of this is to be converted into CH_4, then this would give 750,000,000 kg C available for conversion to CH_4, whereas 10% would give 13,000,000,000 kg C.

Did we have enough C in the RGZ for the formation of CH_4, if we suggest the rock was originally graphitic?

Approximatively, the volume of the RGZ at DLZ can be estimated as 5km long x 0.5km wide x 0.1 km deep = 2.5 x 10^{14} cm^3 (volume).

The RGZ, originally a pelitic schist with a density of 2.8 g/cm^3, would give a mass of 2.5 x 10^{14} cm^3 x 2.8g/cm^3 = 7.0 x 10^{14} g (*i.e.* 7.0 x 10^{11} kg).

If the RGZ originally contained 5.0 wt% C, then 2.5 x 10^{14} cm^3 x 5.0% x 2.8g/cm^3= 3.5 x 10^{13} g of C is available in the area (*i.e.* 3.5 x 10^{10} kg of C).

If the RGZ originally contained 7.5 wt% C, then 2.5 x 10^{14} cm^3 x 7.5% x 2.8g/cm^3= 5.25 x 10^{13} g of C is available in the area (*i.e.* 5.25 x 10^{10} kg of C).

If 5% of this 7.5 wt% C is to be converted into CH_4, then this would give 125,000,000 kg C for conversion, whereas 10% would give 250,000,000 kg C for conversion.

From the very first calculation above, only 11.11kg of C is needed to produce a 1000 kg deposit. This means that enough graphite and enough carbon is available to act as reductant by producing CH_4. Thus, only a small amount of C is needed to produce large volume of CH_4, and thus could easily provide the small volume of CH_4 that is potentially needed to produce an economic grade uranium deposit (*e.g.* Richard *et al*. 2014).

Conclusions

The pelitic schists in the Dufferin Lake Zone are highly variable in mineralogy, textures, and composition, including their graphite and associated sulfide content, with C and S contents ranging from 0.08 to 5.37 wt% and from 0.01 to 10.79 wt%, respectively. The least altered pelitic schists are interpreted to be metamorphosed (now retrograded) black shales on the basis of

their relict mineralogy and whole-rock composition. Carbon content is typical for black shales that formed worldwide at ca. 2.1 Ga.

The pelitic schists contain different morphological/structural habits of graphite, semi-graphite, and carbonaceous matter. There is a relatively sharp change (*i.e.* depletion) in both graphite content and habit, as one moves upward in the drill holes from the least altered rocks through the presumed paleoweathered zone (*i.e.* green, red/green, and red zones – RGZ) into the strongly altered bleached zone, immediately below the unconformity and overlying sandstone-hosted uranium mineralization. The depletion/consumption of graphite is observed macroscopically in drill core by a noticeable reduction of visible graphite, as one moves upward through the RGZ into the bleached zone. This depletion/consumption has been confirmed microscopically via petrographic, geochemical, and Raman analysis of samples collected systematically through these zones. However, the depletion is not complete within the lower RGZ because some carbon species, mixed with chlorite and silica, have been observed in very low quantities. In the bleached zone, there is no recognizable carbon within the studied samples.

A geochemical comparison of the least altered pelitic schists with the RGZ and the bleached zone revealed the gains and losses of elements within each of the alteration zones. Mass-balance calculations between the least altered pelitic schists and the RGZ indicate important fluid-rock interactions and show the loss of C and S. The RGZ contains higher HREE concentrations and is variably depleted in C and S. The bleached zone contains the most highly altered rocks, due most likely to the interaction with several fluid events. It has significantly higher contents of Al, Ti, Na, K, B and U, with very low C and S content. The alteration assemblage of the bleached zone includes abundant dravite, with major removal of quartz and hematite. Mass-balance calculations

indicate significant Mg and B gain as well as U, at the expense of major SiO_2 and Fe_2O_3 depletion, with associated loss of mass and volume.

Our study shows that the alteration and consumption of graphite and associated sulfides could have occurred as the result of several events through time, and may have occurred at the time of uranium mineralization. It is likely that CH_4 was produced, which migrated upwards toward/above the unconformity, as fluid or gas, where it could have acted as a reductant for subsequent uranium mineralization. This could explain the presence of the mineralization in the sandstone. Thus, graphite could have a role in uranium mineralization by forming a mobile reductant (CH_4). In addition, the graphitic EM conductors (*i.e.* brittle fault zones), which act as a main conduit for fluids (and heat), are necessary as they represent zones in which fluid mixing and uranium precipitation can occur within favorable lithologies.

Several events could be responsible for this consumption of graphite (and sulfides) in the upper part of the basement. However, this study suggests that most of the carbon could be consumed during the circulation of basinal brines into the basement. Indeed, fluid inclusions in quartz veins within the basement indicate the presence of the regional basinal brine and an evolved brine in the graphite-depleted bleached zone and the RGZ (Pascal *et al*. 2013). This implies that the circulation of oxidized basinal brines into the basement could have had an impact in the consumption of graphite and sulfides and might have led to a thicker alteration profile, which overprinted the paleoweathering profile described by MacDonald (1980, 1985).

CHAPTER 3
FLUIDS PRESERVED IN VARIABLY ALTERED GRAPHITIC PELITIC SCHISTS IN THE DUFFERIN LAKE ZONE, SOUTH-CENTRAL ATHABASCA BASIN, CANADA: IMPLICATIONS FOR GRAPHITE LOSS AND URANIUM DEPOSITION

Introduction

The unconformity-type uranium deposits located in the Athabasca Basin (Fig. 3-1) of northern Saskatchewan include the world's highest grade uranium deposits. Most of these deposits are located at, or in the vicinity, of the unconformable interface between a Proterozoic sedimentary basin and an Archean to Paleoproterozoic basement complex. The deposits are usually situated close to faults that intersect (*i.e.* breach) the unconformity and are associated with graphitic rocks in the basement.

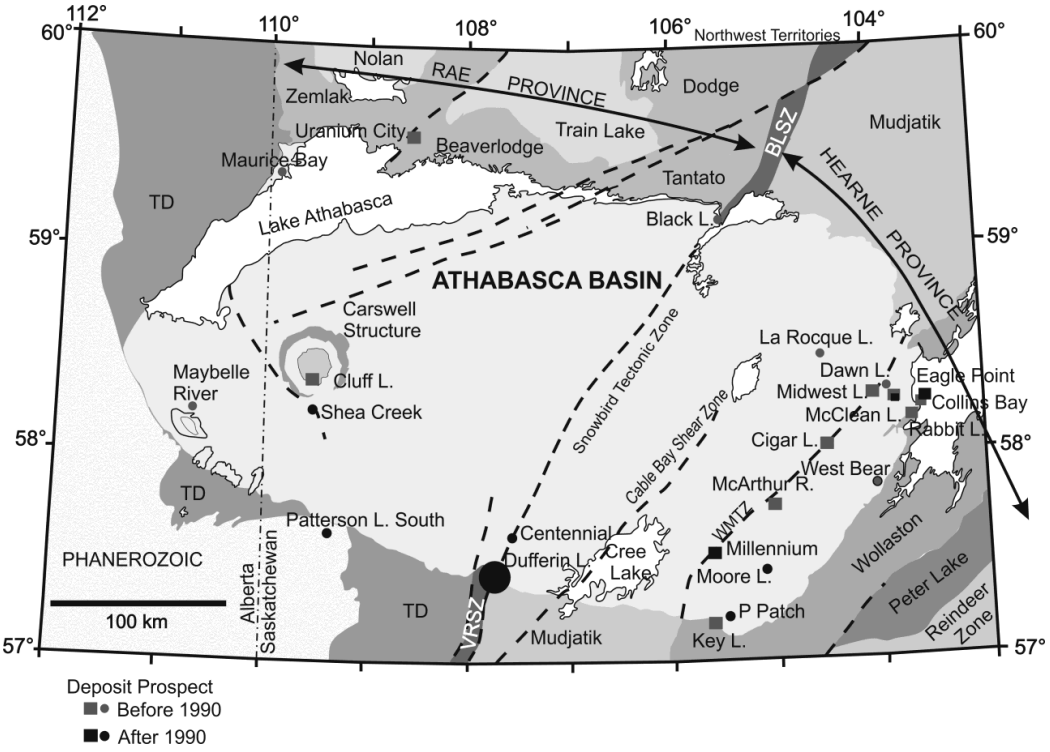

Figure 3-1. Simplified geological map of the Athabasca Basin and underlying tectonic domains (northern Saskatchewan and Alberta, Canada), showing the location of unconformity-associated uranium deposits and occurrences of the Athabasca Basin region of northwestern Canada (modified after Jefferson *et al*. 2007, Card 2012). Heavy dashed lines are selected major reactivated fault zones. The large circle shows the location of the study area, the Dufferin Lake Zone, zoomed in Fig. 2a. TD: Taltson Domain, WMTZ: Wollaston Mudjatik transition zone, VRSZ: Virgin River Shear Zone, BLSZ: Black Lake Shear Zone

These deposits are generally considered to be the result of mixing between oxidized basinal brines and basement-derived reduced fluids (Hoeve & Sibbald 1978, Hoeve & Quirt 1987, Kotzer & Kyser 1990, Kotzer & Kyser 1995, Derome *et al*. 2005, Richard *et al*. 2010), and/or by the interaction of basinal brines with reduced basement lithologies (Hoeve & Quirt 1984, Komninou & Sverjensky 1996, Fayek & Kyser 1997, Derome *et al*. 2005, Derome *et al*. 2007, Mercadier *et al*. 2010, Richard *et al*. 2010, Mercadier *et al*. 2012).

Although these uranium deposits have been the focus of numerous studies over the years, one of the many questions that remains unanswered is whether graphite and/or its breakdown products have any direct role in the formation of mineralization. More specifically, did the graphite act as a reductant for the uranyl complexes to precipitate uraninite (UO_2) to form these deposits (Hoeve & Sibbald 1978, Kyser *et al*. 1989, Landais *et al*. 1993, Raffensperger & Garven 1995, McCready *et al*. 1999a, 1999b, Annesley *et al*. 2001)? As proposed in the original model (Hoeve & Sibbald 1978), graphite and/or carbonaceous matter (CM) are often cited as the reducing media for the genesis of these deposits, releasing CH_4 or CO_2 during interaction with oxidized fluids.

In addition, graphite concentrations can be indicative of basement structures, as it is often concentrated along structures which can be identified as electromagnetic (EM) conductors. Thus, exploration for uranium deposits is often focused on the search for electromagnetic conductors as they can be considered as indicators of the presence of graphitic faults within which the deposits are hosted.

Exploration activity in the south-central Athabasca Basin is focused on the Snowbird Tectonic Zone (STZ), a regionally significant structural corridor that separates the rocks of the Hearne Province to the east from the Rae Province and Taltson Domain to the west (Fig. 3-1). This

exploration resulted in the discovery of the Centennial uranium deposit in 2004 within the Virgin River project area (Jiricka & Witt 2002, Jiricka & Leppin 2003, Powell *et al*. 2007). Additional mineralization was also identified in the Dufferin Lake Zone, and during drilling it was noted that the basement rocks consisted primarily of variably graphitic pelitic schists with a steeply-dipping fabric. However, extending to depths of about 20 to 30 m below the unconformity there is a sub-horizontal zone characterized by the absence of graphite in the basement rocks, even though these rocks are texturally similar, implying that some process must have removed the graphite from these rocks. This zone consists of variably bleached rocks, a few metres thick, immediately below the unconformity, and strongly hematite- and chlorite- altered rocks, tens of metres thick, termed the Red/Green zone (RGZ), underlying the bleached zone. The RGZ has been interpreted to be a paleoweathering profile, as described elsewhere by MacDonald (1980, 1985). More recently, an alternative post-Athabasca hydrothermal origin for the RGZ has also been postulated (Cuney *et al*. 2003). The consumption of graphite may have resulted in the production of a mobile reductant (gas and/or fluid) which may have played a role in the deposition of uranium mineralization.

The purpose of this study is to document the characteristics of the fluids, using microthermomety and Raman analyses of fluid inclusions, that have interacted with the variably graphitic pelitic schists in the basement rocks of the Dufferin Lake Zone. The present study is part of a project designed to examine the processes that may have led to the consumption of graphite in the basement rocks and its consequences. The aim is to determine whether any of the fluids observed in the graphite-depleted zone could be related to the destruction of graphite, and whether there is a potential temporal relationship of these fluids with uranium mineralization in the overlying sandstones. Fluid inclusion studies have been used to understand the origin of the

diagenetic and mineralizing fluids, their chemistry and the conditions for U transport in the Athabasca basin (Pagel & Jaffrezic 1977, Pagel *et al*. 1980, Kotzer & Kyser 1995, Derome *et al*. 2005, Richard *et al*. 2010, Richard *et al*. 2012), but there have been only a few studies of fluids from basement rocks underlying the basin (Pagel 1975, Mercadier *et al*. 2010, Richard *et al*. 2013, Richard *et al*. 2014).

Geological Setting

Regional Geology

The Athabasca Basin (Fig. 3-1) contains the world's highest grade uranium deposits (McArthur River, Cigar Lake), as well as numerous other significant deposits, which are spatially related to the unconformity between the Proterozoic sedimentary rocks and the underlying Archean to Paleoproterozoic basement rocks. The Athabasca Basin consists of a relatively undeformed late Paleoproterozoic to Mesoproterozoic quartz-rich clastic sequence (the Athabasca Group) that is dominated by oxidized (hematitic) quartz arenite. This Proterozoic basin is thought to have started forming at about 1750Ma (Kotzer *et al*. 1992).

Basement to the basin consists of the Rae Province and the Taltson Domain to the west, and the Hearne Province to the east, separated by the northeast-trending Snowbird Tectonic Zone (Hoffman 1988) (Fig. 3-1). The Hearne and the Rae provinces consist mainly of Archean gneisses that have been multiply deformed and metamorphosed at upper amphibolite to granulite grade in places (Card *et al*. 2007). The Rae Province of northern Saskatchewan is represented by several lithotectonic domains including from west to east the Zemlak, Beaverlodge and Tantato domains with the latter bounded to the east by the Black Lake Shear Zone (Fig. 3-1). The Taltson Domain, which includes the dominantly 2.0 to 1.9 Ga intrusive rocks of the Taltson Magmatic Zone in northeastern Alberta, has been metamorphosed during the Taltson Orogeny at ca. 1.9 Ga. This orogeny and the younger Trans-Hudson Orogen (ca. 1820-1790 Ma) have resulted in

extensive thermotectonic reworking of the basement rocks, although the effects of the latter are more significant in the Hearne Province (Thomas *et al*. 2000, Card *et al*. 2007). The Hearne Province consists of the Wollaston and the Mudjatik domains (Fig. 3-1). The Wollaston Domain is a northeast-trending fold-thrust belt that formed during the Trans-Hudson Orogen, and is composed of Paleoproterozoic Wollaston Group metasedimentary rocks overlying Archean granitoid gneisses, whereas the Mudjatik Domain is a northeast-trending belt consisting mainly of Archean felsic gneisses (Annesley *et al*. 2005, Yeo & Delaney 2007).

The majority of the known unconformity-type uranium deposits are located in the eastern part of the Athabasca Basin, in the vicinity of the graphite-rich Wollaston-Mudjatik Transition Zone (Annesley *et al*. 2005; Fig. 3-1). All of the structures that are associated with uranium deposits developed under ductile conditions during the Taltson-Thelon and Trans-Hudson orogenies, and were reactivated in the brittle regime during and after deposition of the Athabasca Group (Card *et al*. 2007).

Geology of the Dufferin Lake Zone

The Dufferin Lake Zone (DLZ) is located in the south-central Athabasca Basin, and is spatially associated with the southern-most part of the STZ, consisting of a 4.5 km wide zone of cataclasites and mylonites (Gilboy 1985a), named the Virgin River shear zone (VRSZ) (Hoffman 1990). This forms the boundary between the Mudjatik Domain to the east and the Taltson Domain to the west (Figs. 3-1, 3-2a).

The basement rocks in the Mudjatik Domain are composed mainly of felsic gneisses (Fig. 3-2a) (Gilboy 1985a) with lesser quartzite, pelitic and variably graphitic metasedimentary rocks, and deformed amphibolites, granitoids, and pegmatites that have been metamorphosed to upper greenschist to amphibolite grade. The oldest rocks in this domain are the granitoid gneisses,

which are considered to be Archean in age (Card *et al*. 2007). In this domain, D1 deformation is characterized by the development of a well-developed S_1 foliation and gneissosity that transposes layering in supracrustal rocks leading to rare intrafolial F2 folds (Card *et al*. 2008). Tight north-east-striking F_3 folds are gently folded by orthogonal north-west-striking F_4 folds, leading to the formation of domes and basins in the Mudjatik Domain (Card *et al*. 2008).

The Taltson Domain contains granulite-facies assemblages in the northwest part of the exposed basement and amphibolite-facies rocks near the VRSZ (Card *et al*. 2008). Rocks consist mainly of orthogneiss, dominated by granodioritic compositions (Card *et al*. 2007, Card 2002). In this domain, a gently northeast-dipping S1 foliation, resulting from the first well-defined deformation event (D1), and the D2 fabric with increasing intensity towards the VRSZ are well developed (Card *et al*. 2007). F3 folds accompanied by a S3 foliation oriented parallel to the mylonitic foliation of the VRSZ are also present. In the VRSZ, the D3 deformation consists of the D2 deformation fabric without the presence of folds, and records multiple ductile events (Card *et al*. 2007).

The D3 deformation event affected all the Taltson Domain basement rocks and is interpreted to have originated during formation of the earliest phase of the VRSZ (Card & Bosman 2007). F4 folds post-date the VRSZ and are most likely of Trans-Hudson age (Card & Bosman 2007). The VRSZ is interpreted as a suture that juxtaposed the Mudjatik Domain with the eastern part of the Taltson Domain. The core of the VRSZ contains medium-grade psammopelite to pelitic schist and amphibolite, known as the Virgin Schist Group (VSG) (Fig. 3-2a) (Card & Bosman 2007, Card *et al*. 2008, Johnson 1968), and the eastern part of the Taltson Domain (Card 2012). In the VSG, a S0/S1 foliation is developed, potentially equivalent to the S1 foliation in the eastern part of the Taltson Domain. Folding about a northwest-dipping axial surface overprinted

by northeast-trending folds with southeast-dipping axial surfaces is well developed in the DLZ (Card *et al.* 2007).

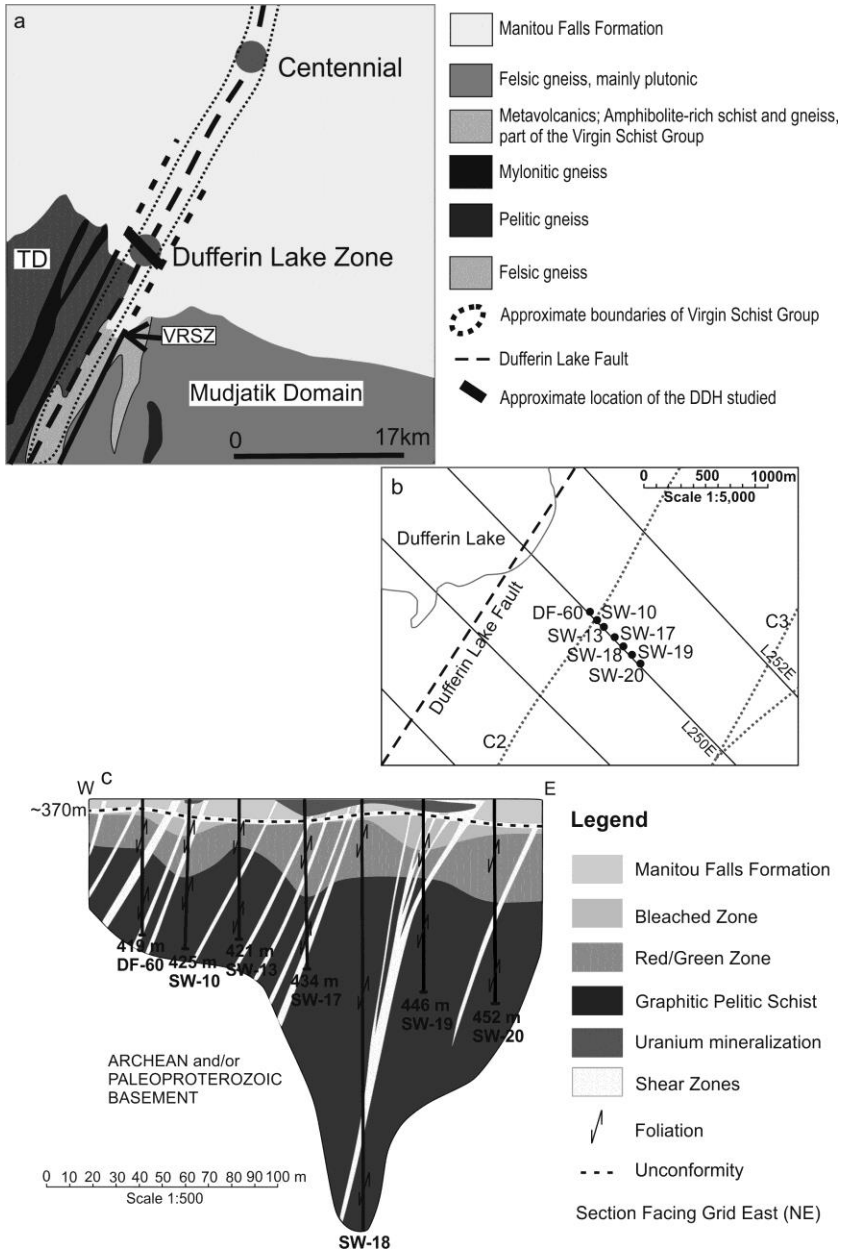

Figure 3-2. Geological relationships in the study area. (a) Geology of the Virgin River Trend showing the surface projection of the locations of the Dufferin Lake Zone and the Centennial deposit. TD: Taltson Domain, VRSZ: Virgin River Shear Zone (modified after Gilboy 1985b, Card 2009, Geological Atlas of Saskatchewan). The black line shows the location of the drillhole section in b and c. (b) The location of the DDHs studied along grid line L250E, relative to the conductors C2 and C3, and the Dufferin Lake Fault. (c) Geological cross section along grid line L250E, illustrating the presence of graphite-depleted (bleached zone and red/green zone) and graphite-rich (graphitic pelitic schists) zones

This area hosts two main of unconformity-type uranium deposits and showings the Centennial Deposit (Jiricka & Witt 2002, Jiricka & Leppin 2003, Reid *et al*. 2014) and the DLZ (Jiricka *et al*. 2007). The VRSZ was reactivated after the deposition of the Athabasca Group as a northwest-dipping reverse fault, named the Dufferin Lake fault (Figs. 3-2a, b), which offsets the unconformity by over 250 metres (Card *et al*. 2007, Powell *et al*. 2007). This fault probably had an important role in the development of uranium mineralization in the area, as it appears to have acted as a fluid conduit over an extended period of time (Thomas *et al*. 2000, Alexandre *et al*. 2012).

Graphitic-rich EM conductors are present in the area, as graphite- and sulfide-bearing pelitic rocks (Thomas 2002) in the footwall of the Dufferin Lake Fault (Fig. 3-2b), and which are parallel to this later brittle structure (Jiricka *et al*. 2007). These graphite-related EM conductors associated with the Dufferin Lake fault encouraged exploration in the area (Powell *et al*. 2007). Conductive rocks were intersected by drill holes in the DLZ (Thomas 2002, Jiricka *et al*. 2003, Card *et al*. 2007), and sub-economic uranium mineralization was intersected within the DLZ in diamond drill holes (DDH) SW10, SW13, SW17, SW18 and SW19 (Figs. 3-2b, c). Uranium mineralization is hosted by quartz arenite at the base of the Manitou Falls Formation (Fig. 3-2c), and is associated with bleaching and clay alteration of the sandstones (Jiricka *et al*. 2007).

The basement rocks directly underlying the DLZ are composed primarily of variably graphitic (locally sulphidic) pelitic schists (Fig. 3-2c). Pseudomorphs interpreted to be originally garnet, staurolite and/or andalusite (Wallis 1970) in the pelitic rocks, suggest that the metamorphic grade attained was at least lower amphibolite-grade (Pascal *et al*. 2013). In outcrop to the south of the DLZ, the VSG are interpreted to have been metamorphosed at middle amphibolite facies (Card *et al*. 2008). These graphitic pelitic schists have a primary layering (S0) and early foliation (S1)

refolded isoclinally. These rocks display a local crenulation cleavage which overprints this fabric, as observed by Card *et al*. (2007) and Card *et al*. (2008). Brittle and/or ductile faults with quartz (+/- carbonates) and pyrite veins crosscut this fabric.

Beneath the sub-Athabasca unconformity are zones in which graphite is not apparently present, namely the bleached zone and the RGZ (Fig. 3-2c). The transition from the RGZ to fresh rock occurs gradually with depth, and metamorphic textures and structures observed in the basement are preserved in the RGZ (Fig. 3-2c). From these observations it is interpreted that the variably graphitic pelitic schists once extended into the zone now identified as the RGZ. A strong foliation (S1?) and shear zones are oriented at 10° to 30° to core axis, albeit contorted and microfolded. The bleached zone is thickest in the vicinity of the larger shear zones (Fig. 3-2c). The lower part of the RGZ is more chlorite-rich than the upper part, which is more hematite-rich. The lower part records more reducing conditions since minor amounts of microscopic graphite, observed in thin sections, have been preserved in this part of the RGZ (Pascal *et al*. 2013). Late brittle/ductile deformation took place with the formation of quartz and hematite veinlets which crosscut the schistose fabric.

Quartz Generations

Within this study, four quartz generations (Q1, Q2, Q3, Q4) have been identified in the basement samples, based on drillcore and petrographic observations. Q1 represents the metamorphic quartz within the pelitic schist. This quartz is cut by quartz veins (Q2) which show evidence of ductile deformation, are oriented subparallel to the schistosity, and interpreted to have formed at high temperature. Q2 is subdivided into Q2a and Q2b. Q2a is strongly recrystallized and is pre- to syn- ductile deformation. Q2b shows similar textures to Q2a, but is clearer and slightly younger. Q3 is observed within brittle quartz veins consisting of druzy

quartz, clear quartz, and carbonates. Q4 occurs as late narrow quartz veinlets associated with carbonates, hematite, and pyrite; crosscutting all other generations of quartz.

Q1 grains, metamorphosed during the Hudsonian metamorphic event and Q2 veins (subparallel to the mylonitic fabric) are presumed to have formed before the deposition of the Athabasca Basin. However, Q3 and Q4 veins occur within later brittle fractures that could be related to post-Athabasca deformation and therefore could potentially be related to uranium mineralization. Graphite consumption in the RGZ and the bleached zone could have been the result of post peak metamorphic pre-, syn- or post Athabasca basin fluid events (Pascal *et al*. 2013), during the paleoweathering event or due to interaction with diagenetic fluids.

Two samples (SW18-382.5 and SW42-484.0) (Fig. 3-3), which show the different type of quartz generations, were selected for fluid inclusion microthermometry. Sample SW18-382.5 (Fig. 3-3a) comes from the RGZ, about 14 m below the unconformity, and below the mineralized area located in the sandstone above the unconformity. It is brecciated and is principally composed of hematite and chlorite with quartz boudins, and quartz veinlets. A simplified paragenetic sequence of minerals has been established based on thin and thick section observations. Chlorite and hematite overprinted the original fabric, during the development of the paleoweathering profile or later hydrothermal alteration. Two wafers for fluid inclusion study (SW18-382.5a and SW18-382.5b) have been prepared from quartz boudins and quartz veins from this sample. Both samples contain Q2, Q3 and Q4 (Figs. 3-4a, b, c, d), and fluid inclusions in Q2 and Q3 were studied in SW18-382.5a and SW18-382.5b respectively.

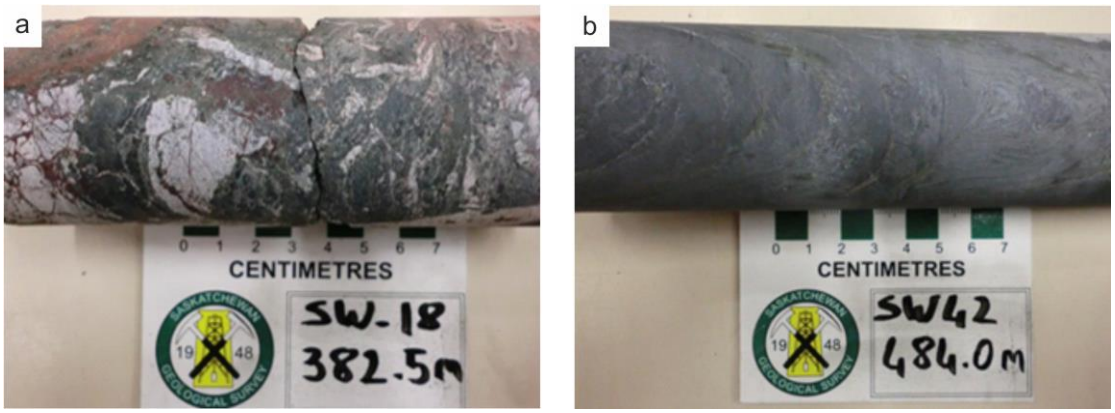

Figure 3-3. Samples studied from the Dufferin Lake Zone. (a) SW18-382.5 - pelitic schist from the RGZ. (b) SW42-484.0 – moderately graphitic pelitic schist

Sample SW42-484.0 (Fig. 3-3b) is a moderately graphitic pelitic schist containing rotated boudinaged quartz veins (Q2a), sulfides along fractures, and quartz veinlets (Q2b). Sericite, chlorite, graphite (+/- disseminated particles of fine-grained carbonaceous matter), and disseminated sulfides are elongated along the mylonitic fabric. In this sample, fluid inclusions have been studied in Q2 veins (Figs. 3-4e, f).

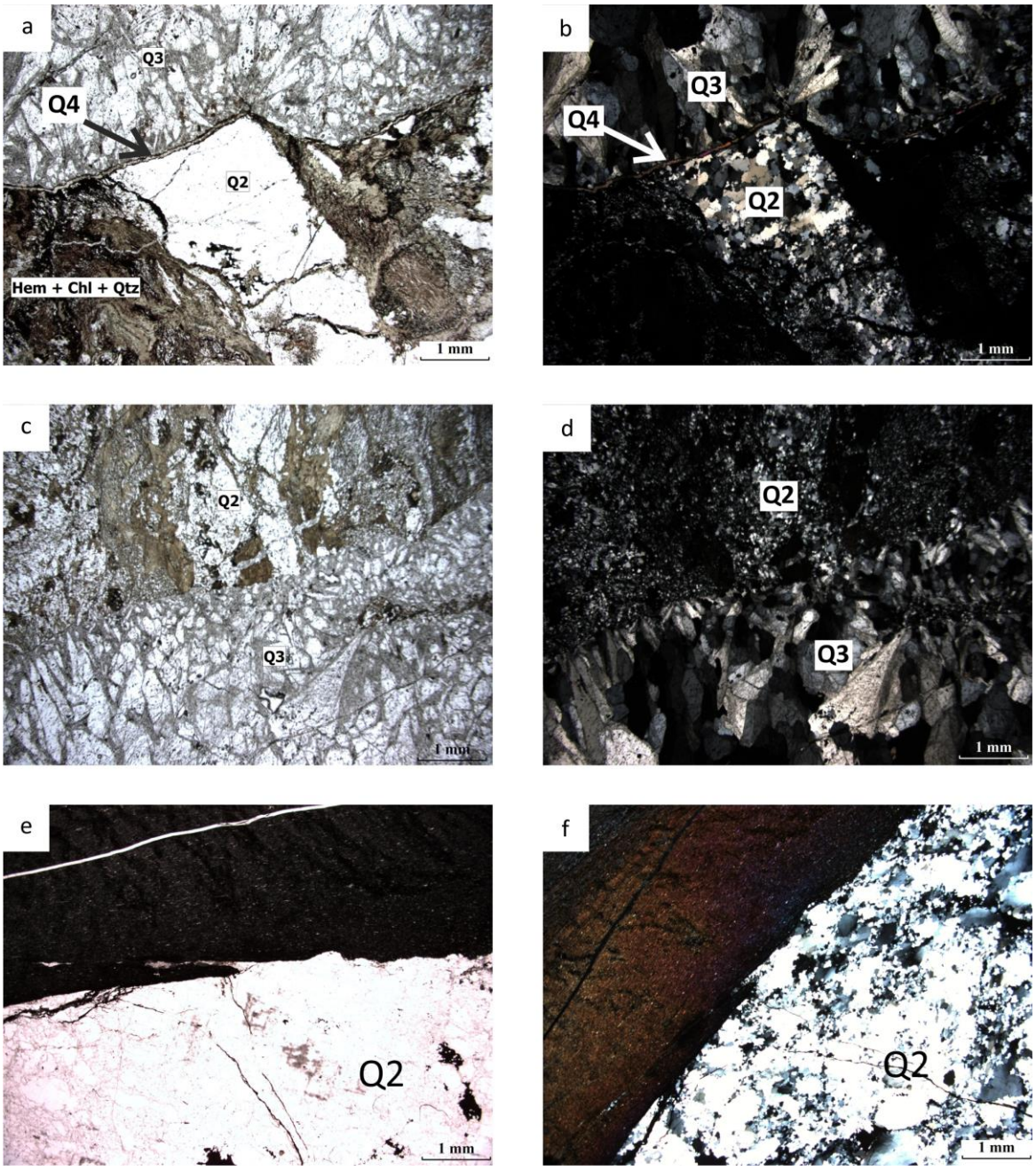

Figure 3-4. Photomicrographs of the different quartz generations. (a) Q2 vein is crosscut by Q3 vein and then are crosscut by the veinlet Q4 in samples SW18-382.5a from the RGZ in plan polarized light. Q3 is composed of clear quartz, druzy quartz and carbonates. (b) Same as a, but in crossed polarized light. Q2 vein is recrystallized. (c) Q2 vein is crosscut by Q3 vein in sample SW18-382.5b from the RGZ, in plan polarized light. (d) Same as c, but in crossed polarized light. (e) Q2 vein subparallel to the fabric in samples SW42-484.0 from the graphitic pelitic schist in plan polarized light. (f) Q2 vein subparallel to the fabric in samples SW42-484.0 from the graphitic pelitic schist in crossed polarized light

Fluid Inclusion Study

Analytical Methods

Doubly-polished fluid inclusion chips were prepared at the Thin Section Laboratory at the University of Saskatchewan. Microthermometry was carried out on a Linkam heating-cooling stage adapted to an Olympus microscope at the GeoRessources laboratory in Nancy, to observe ice melting (Tmice), halite dissolution (TmNaCl), and homogenization (Th) temperatures. The standards used were natural or synthetic fluid inclusions, including a pure CO_2 fluid inclusion with a Tmice known at -56.6°C and a H_2O-NaOH sample with a Tmice known at -0.4°C. According to the calibration curves, temperatures of phase changes are given with an accuracy of about ±0.1 °C for Tmice and ±1 °C for TmNaCl and Th. All the studied samples were cooled down to -180°C prior to heating up to ambient temperature and above.

The analysis of gas species present in monophase fluid inclusions was performed at room temperature with a Dilor-Labram Raman microspectrometer at GeoRessources in Vandoeuvre-lès-Nancy (France), on selected samples previously studied by microthermometry, following the procedure described by Dubessy *et al*. (1989). The 514.5 nm argon laser beam was focused on the fluid inclusion with the x80 objective lens of the microscope and a laser power of 200 mW.

Fluid Inclusion Petrography

Different types of secondary fluid inclusions (based on the criteria proposed by Roedder (1984) in quartz veins and boudins have been observed along grain boundaries of quartz grains (Figs. 3-5a, b) and in microfractures crosscutting grains (Fig. 3-5b). Unfortunately, no convincing primary fluid inclusions were recognized in any of the quartz samples.

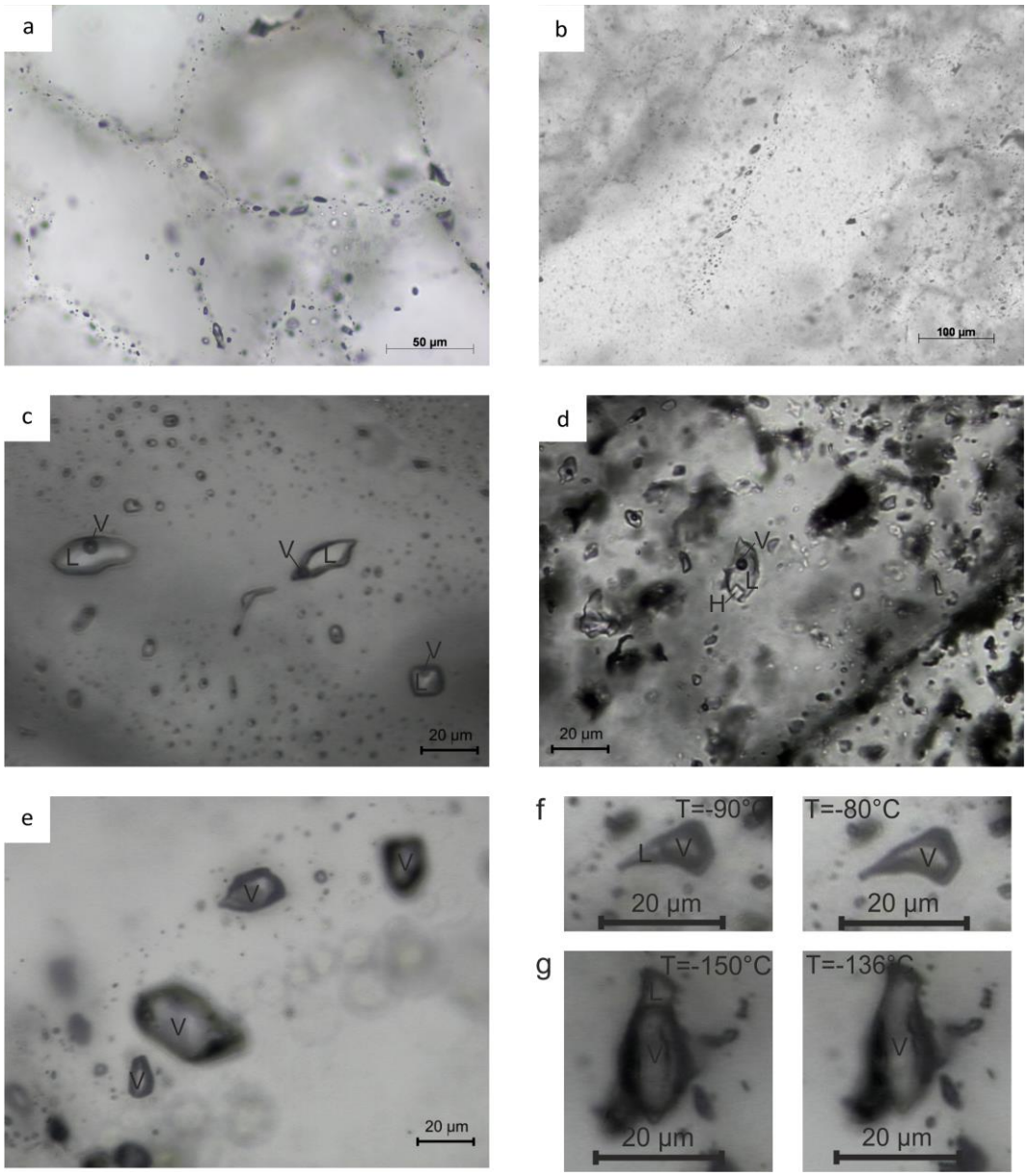

Figure 3-5. Location and types of the major fluid inclusions in quartz vein samples of this study (PPL transmitted light). (a) Repartition of fluid inclusions at the junction of quartz grains. (b) Repartition of fluid inclusions in plan section crosscutting quartz grain. (c) Two-phase (Liquid (L) +Vapor (V)) fluid inclusions present in the RGZ (sample SW18-382.5). (d) Three-phase (L+V+Halite (H)) fluid inclusions present in the RGZ (sample SW18-382.5). (e) Monophase vapor fluid inclusions from the graphitic pelitic schist (sample SW42-484.0). (f) Monophase vapor fluid inclusion from the variably graphitic pelitic schist, which homogenize to the vapor phase around -80°C. The picture on the left shows both liquid and vapor phase that become only vapor phase around -80°C (picture on the right). (g) Monophase vapor fluid inclusion from the variably graphitic pelitic schist, which homogenize to the vapor phase around -130°C The picture on the left shows both liquid and vapor phase that become only vapor phase around -130°C (picture on the right)

In the samples from the RGZ (SW18-382.5a and SW18-382.5b), three types of fluid inclusions are observed at room temperature. These types are listed below in order of decreasing abundance and seem to represent one fluid inclusion assemblage. The aqueous fluid inclusions have been named following the nomenclature of Derome *et al*. (2005), Mercadier *et al*. (2010) and Richard *et al*. (2010). Inclusions showing Tmice below -30°C and above -30°C are referred to as Lw'or Lw1 inclusions, respectively. Inclusions similar to Lw' and Lw inclusions but with a halite cube at room temperature are referred to as Lwh or Lwh' inclusions depending on the nature of the last phase to melt (hydrohalite or ice respectively). Type 1 fluid inclusions correspond to two-phase liquid (L)-rich secondary fluid inclusions (Lw1 or Lw') (Fig. 3-5c), and are the most abundant in Q2 and Q3. This type comprises about 80% of the fluid inclusions. The volume fraction of the vapor (V) phase in these inclusions is typically close to 10% (Fig. 3-5c). Type 2 fluid inclusions corresponds to three-phase (L+V+Halite (H)) (Lwh or Lwh') secondary fluid inclusions (10%) (Fig. 3-5d), and are also present in Q2 and Q3. Type 2 fluid inclusions are characteristic of a fluid saturated in halite at the trapping temperature. A very low number of monophase vapor (Vw) fluid inclusions (2%) have been observed in Q3, and represent a type 3 of fluid inclusions.

The fluid inclusions vary considerably in shape, from regular to irregular shape (Figs. 3-5c, d). The average size of the fluid inclusions is 10-20 μm.

In the quartz from the graphitic pelitic schist (SW42-484.0), dark monophase vapour-rich inclusions (Fig. 3-5e) similar to type 3 (Vw) fluid inclusions in the RGZ are the dominant type. The volume fraction of the V-phase in these inclusions is typically close to 95-100% (Figs. 3-5e, f, g) with less than 5% liquid suspected but not always visible. This suggests a very low density fluid.

Microthermometric Results

Tmice was determined after cooling the samples down to -180°C. Th(L), Th(V), and TmNaCl were determined by heating up to ambient temperature and above, up to +180°C (Table 3-1). The complete microthermometric data are found in supplementary Appendix G.

Table 3-1. Summary of microthermometric characteristics of the secondary fluid inclusions

Basement Rocks	Sample name	Depth below the U/C (m)	FI Type	Q-types	Range (°C)
			Two-phase (L+V)	Q2	-31.5 <Tmice< -16.4 107.5 <Th(L)< 275.0
				Q3	-35.5 <Tmice< -22.7 90.6 <Th(L)< 161.3
RGZ	SW18-382.5	382.5	Three-phase (L+V+Halite)	Q2	193.1 <TmNaCl< 217.7 69.1 <Th(L)< 93.7
				Q3	189.7 <TmNaCl< 239.0 100.3 <Th(L)< 125.3
			Monophase vapor	Q2	Th(V) ~137.3
VGPS	SW42-484.0	484.0	Monophase Vapor	Q2	-152.1 < Th(V)< -74.1

FI: Fluid inclusions, L: Liquid, V: Vapor, Tmice: Temperature of melting ice, Th(L): Temperature of homogenization to the liquid phase, Th(V): Temperature of homogenization to the vapor phase, TmNaCl: Temperature of halite dissolution

In sample SW18-382.5, the type 1 (Lw1 and Lw') fluid inclusions display Tmice ranging from -35.5°C to -16.4°C but with a dominant population between -26°C and -23°C (Fig. 3-6) for both Q2 and Q3. These ice melting temperatures indicate that salts other than NaCl are present in the fluid, and are similar to those observed by Derome *et al*. (2005). Thus, using the H_2O-NaCl-$CaCl_2$ system, and the software from Chi & Ni (2007), these temperatures yield a range of salinity between 27.4 and 19.8 wt% equivalent NaCl-$CaCl_2$ for all the type 1 fluid inclusions and between 24.6 and 23.7 wt% equivalent NaCl-$CaCl_2$ for the dominant population between -26 and

-23°C (Fig. 3-7). Two-phase fluid inclusions from both Q2 and Q3 are quite similar (Table 3-1), except that two-phase fluid inclusions from Q2 have slightly lower salinities, as indicated by lower Tmice. All of these type 1 fluid inclusions homogenize into the liquid phase predominantly between 90°C and about 170°C (Figs. 3-7, 3-8). Only a few two-phase fluid inclusions from Q2 yield higher Th (Figs. 3-7, 3-8) and only a few three-phase fluid inclusions from Q2 yield lower Th (Figs. 3-7, 3-8).

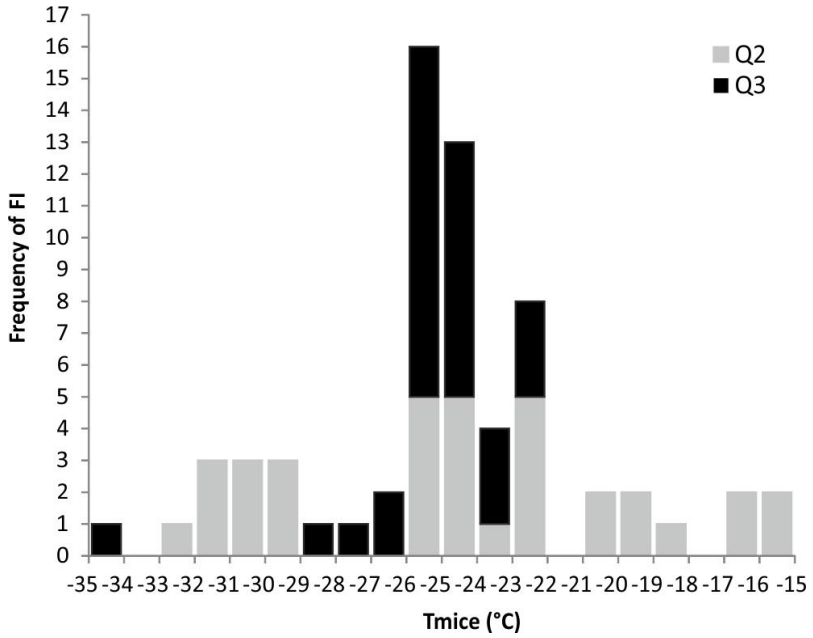

Figure 3-6. Histogram showing the number of measurements of the temperature of ice melting (Tmice) from fluid inclusions (FI) in Q2 (from SW18-382.5a) and Q3 (from SW382.5b)

The TmNaCl in type 2 (Lwh or Lwh') inclusions are measured to be between 190°C and 240°C, which converts to a salinity ranging between 31 and 34 wt% equivalent NaCl-$CaCl_2$, after Sterner *et al*. (1988). These TmNaCl are considerably higher than the Th for the same inclusions, which range from 69 to 125°C, with the higher Th for the three-phase fluid inclusions from Q3 (Fig. 3-7). In these three-phase fluid inclusions, including halite, no ice nucleated when cooled down to -180°C.

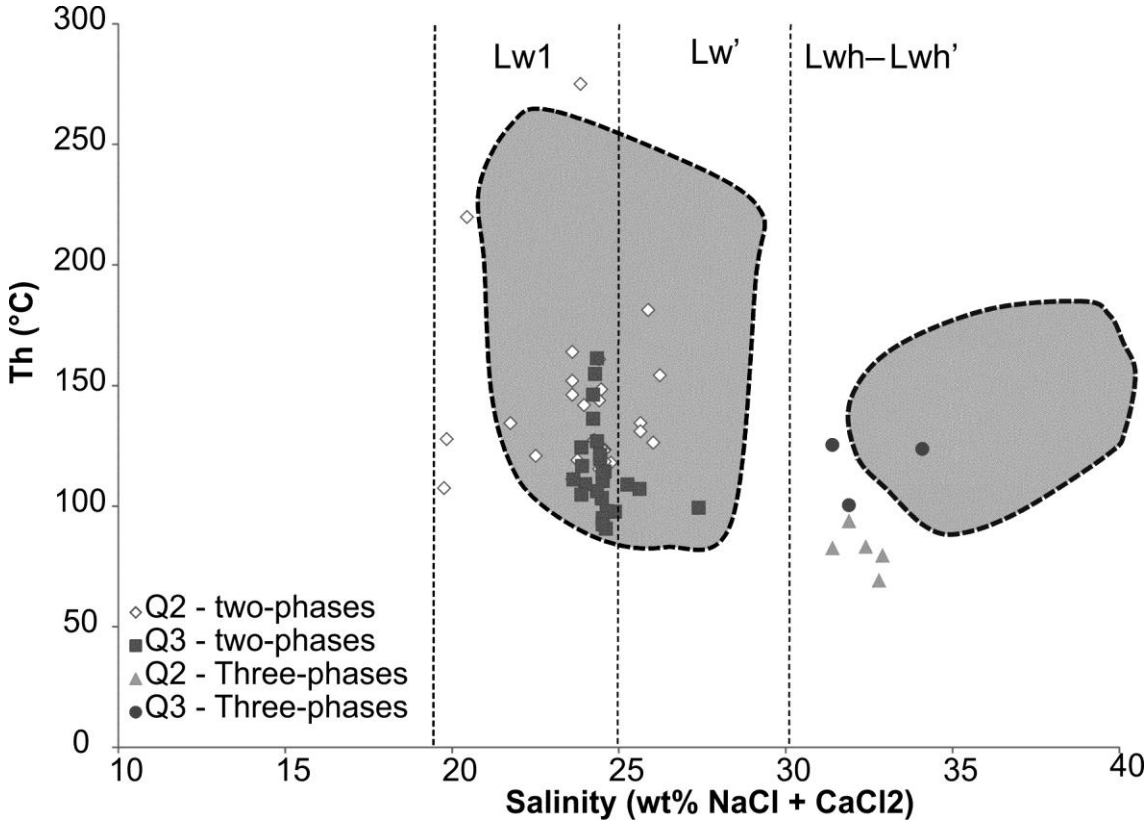

Figure 3-7. Temperature of homogenization (Th) and salinity in the NaCl-$CaCl_2$ system for two-phase and three-phase aqueous fluid inclusions from the RGZ (modified after Mercadier *et al*. 2010). The salinity increases as the Th decreases, as observed by Derome *et al*. (2005) and Mercadier *et al*. (2010). Lw1 and Lw' correspond to NaCl-rich brines and CaCl-rich brines, respectively, from the data from Derome *et al*. (2005) and Mercadier *et al*. (2010).The grey areas represent the data from Mercadier *et al*. (2010)

The Th versus salinity plot (Fig. 3-7) of the aqueous fluid inclusions shows a broad increase in salinity with a decrease in Th, which is similar to trends observed at McArthur River (Derome *et al*. 2005) and P-Patch (Mercadier *et al*. 2010).

In sample SW42-484.0, all of the volatile-rich fluid inclusions (Vw) homogenize into the vapor phase (Figs. 3-5f, g) mainly between -135 and -125°C and -90 and -70°C (Fig. 3-9), with no evidence of freezing or melting of the liquid phase.

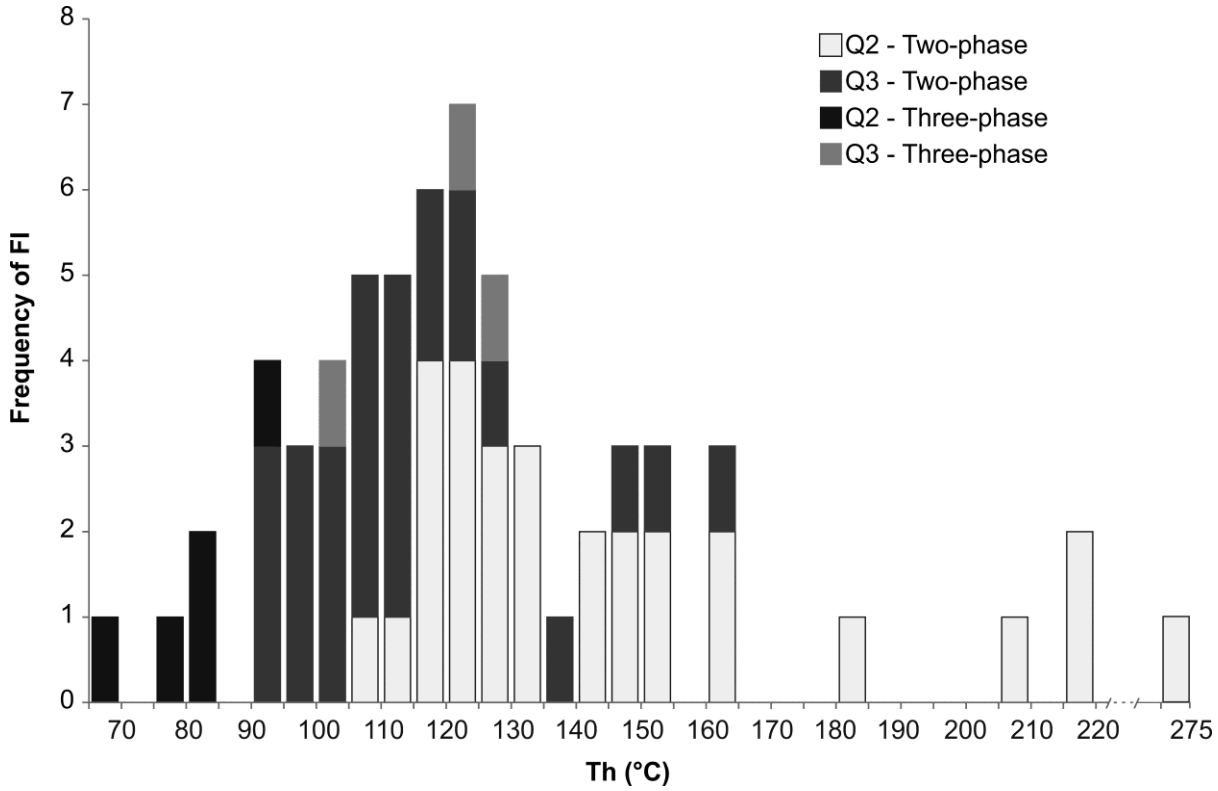

Figure 3-8. Histogram showing the number of measurements of the temperature of homogenization (Th) in fluid inclusions from Q2 (from SW18-382.5a) and Q3 (from SW382.5b)

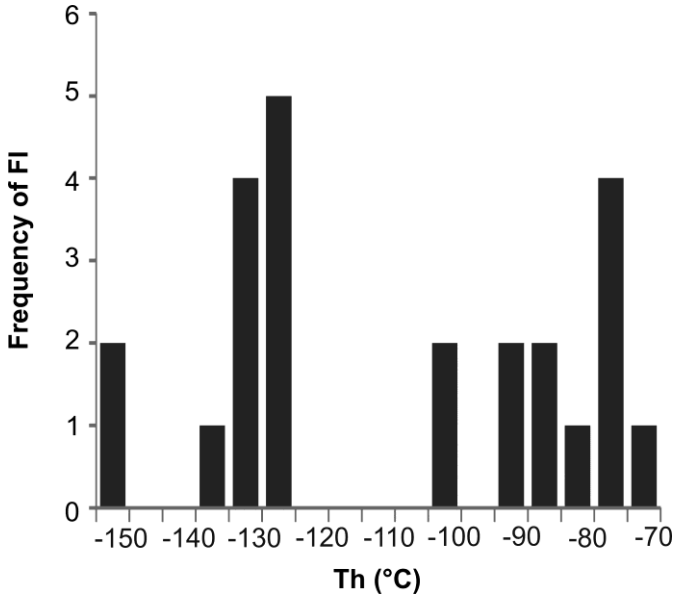

Figure 3-9. Histogram showing the number of measurements from SW42-484.0 of the temperature of homogenization into vapor phase

Raman Results

Raman analysis was carried out to determine the composition of the gas phase in selected monophase fluid inclusions from SW42-484.0 and SW18-382.5a (Table 3-2). The different fluid inclusions were chosen to provide an overview of the different gas species as a function of the Th.

Table 3-2. Composition of the volatile phase (mol.%) obtained by Raman spectroscopy for monophase vapor fluid inclusions and corresponding microthermometric measurements

Fluid Type	Location	Sample	FI type	Th(V) (°C)	Raman data
N_2 - dominant fluid	VGPS	SW42-484.0	V(w)	-152.1 < Th(V)< -100.8	n.d <CO_2< 1.9 11.0 <CH_4< 18.8 81.2 <N_2< 87.8
	RGZ	SW18-382.5	V(w)	Th(V) = -137.3	CO_2 = n.d 14.7 <CH_4< 22.1 77.9 <N_2< 85.3
CH_4 - dominant fluid	VGPS	SW42-484.0	V(w)	-81 < Th(V) < -74.1	n.d <CO_2< 16.4 77.2 <CH_4< 95.5 4.5 <N_2< 14.7

FI: Fluid inclusions, Th(V):Temperature of homogenization to the vapor phase, VGPS: Variably graphitic pelitic schist, RGZ: Red/green zone, n.d: not detected

This study has shown the presence of two main gases: methane (CH_4) and nitrogen (N_2) in variable amounts (Fig. 3-10). Some inclusions contain traces of CO_2 and traces of H_2S. Methane content in the CH_4-dominant fluid inclusions range from 77.2 to 95.5 mol.% whereas the N_2 content ranges from 4.5 to 14.7 mol.% . In the N_2-dominant inclusions, N_2 ranges from 21.2 to 87.8 mol.% with 11.0 to 18.8 mol.% of CH_4 in the less altered basement rocks, and 77.9 to 85.3 mol.% N_2 and 14.7 to 22.1 mol.% CH_4 in the RGZ. The fluid inclusions with N_2-dominant

correspond to the fluid inclusions with the lowest Th values (Fig. 3-9). Only a few vapor phase of the two-phase fluid inclusions from the RGZ have been analyzed, and CH_4 have been observed.

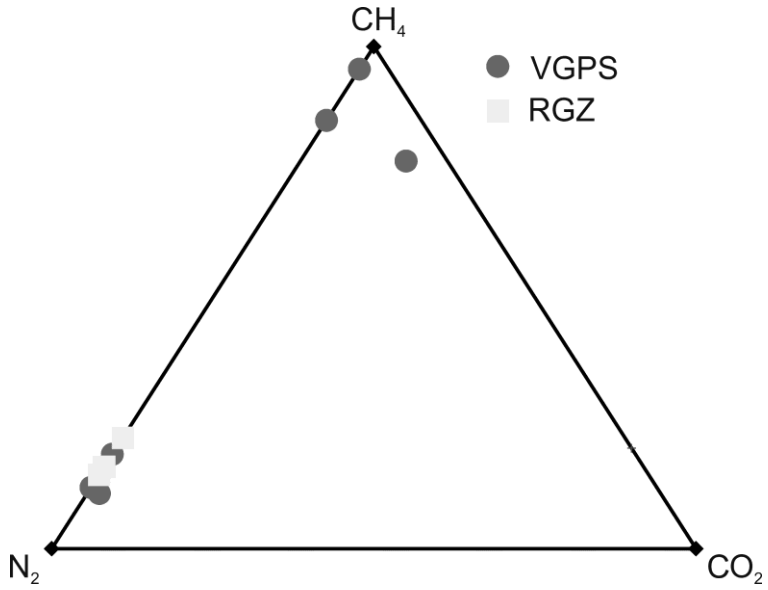

Figure 3-10. Ternary diagram showing the different compositions of fluid inclusions determined by Raman analyses in the variably graphitic pelitic schist (VGPS) and in the red/green zone (RGZ)

Pressure – Temperature Estimation

Using the microthermometric measurements and Raman analyses, a series of isochores representative of the two main compositions (CH_4 and N_2) for the volatile-rich fluid inclusions (Vw) have been calculated, using the computer code developed by Bakker (1999) (Fig. 3-11). Because water was suspected but not visible, an isochore for both fluids was also constructed assuming 5% of water. This led to a slight shift of the isochores to higher pressure, of about 10 to 20 Mpa depending on the temperature, *i.e.* around 10 MPa at 200°C and up to 20 MPa at 500°C.

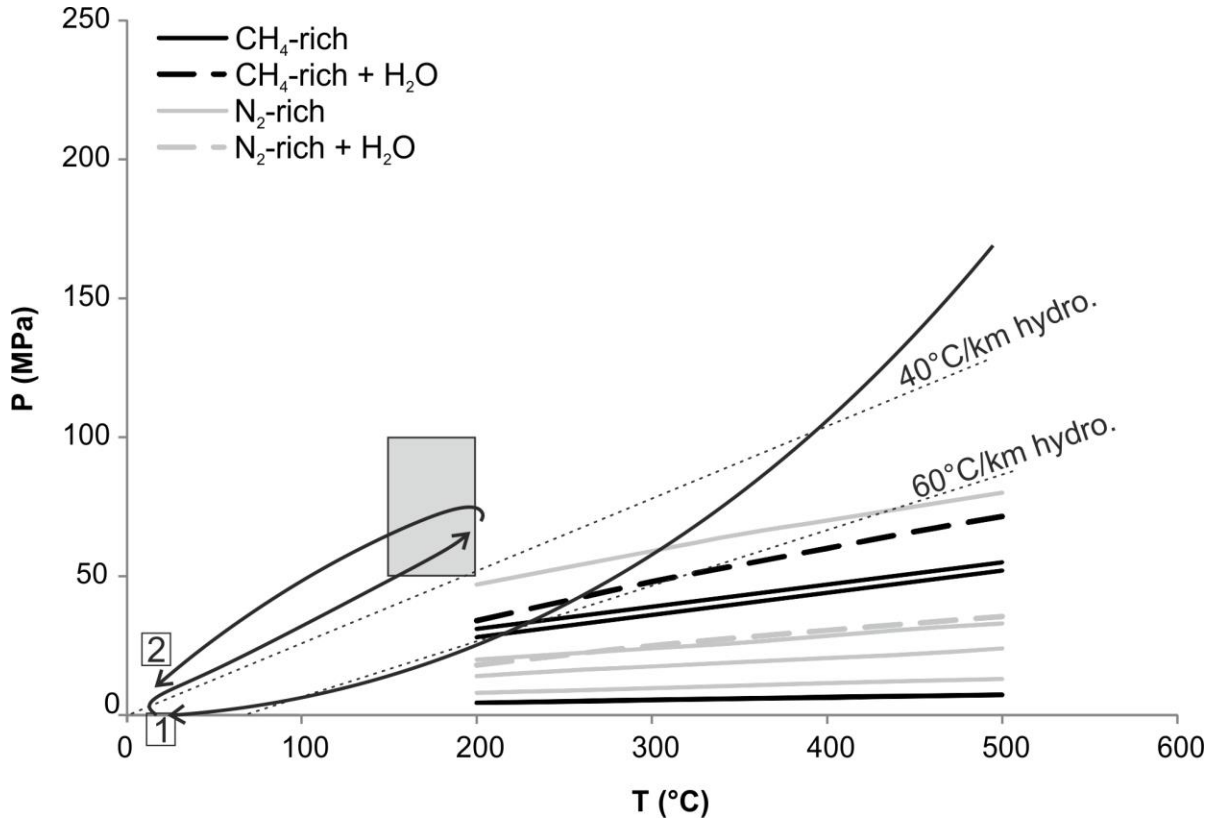

Figure 3-11. Pressure-temperature graph showing isochores drawn using the calculated molar volume, based on the different CH_4 and N_2 contents of the fluid inclusions. The grey box corresponds to the estimated P-T in the basin during the diagenetic hydrothermal alteration (ca. 1600-1400Ma) from 200 to 150°C after Derome *et al*. (2005), and Mercadier *et al*. (2010). The black arrow represents the low pressure section of the retrograde path after metamorphism during the Trans-Hudson Orogeny (after Annesley *et al*. 2005). Stage 1 corresponds to the uplift of the basement before the deposition of the Athabasca basin sediments. Stage 2 corresponds to the uplift of the basement after the deposition of the Athabasca Basin. The hydrostatic gradients calculated for thermal gradients of 40° and 60 °C/km during the Trans-Hudson late metamorphism are displayed

The isochores corresponding to the N_2- and CH_4- rich fluid inclusions define approximately similar P-T conditions with relatively low pressure due to the large predominance of the vapor phase of the inclusions at room temperature. The range of pressure-temperature estimated for V(w) inclusion is 4.5 to 80 MPa for a temperature range of 200 to 500°C under hydrostatic regime (Fig. 3-11). The isochores give lower pressure than the P-T conditions determined by Annesley *et al*. (2005) for the lower temperature and pressure segment of their retrograde path

after peak metamorphic conditions had been obtained in the Wollaston Domain. The isochores have also a lower pressure than the maximum P-T conditions estimated in the basin by Derome *et al*. (2005), and Mercadier *et al*. (2010), which is considered to be about 150 to 200°C and 50 to 100 MPa. The presence of monophase N_2-CH_4 fluid inclusions which homogenize into the liquid, leading to higher pressure, could resolve this problem of lower pressure compared to the P-T conditions already estimated in the basin; but none of this FI type has been observed.

Discussion

Three types of fluid have been observed, one highly saline which is only observed in the sample from the RGZ, one dominated by CH_4, and one dominated by N_2. The latter two mainly occur within the graphitic pelitic rocks, but the N_2-rich fluid has also been observed in small amounts in the RGZ (Table 3-1, Table 3-2).

Origin and Role of the C-N Fluids

Nitrogen is a common component in fluids from metamorphic environments (Huff & Nabelek 2007) especially in graphite-bearing lithologies (Bottrell *et al*. 1988). During the early stages of diagenesis of organic matter-bearing sediments, nitrogen is liberated from the organic molecules and is stored as ammonium ion (NH_4^+) substituting for K^+ in K-micas and K-feldspar (Bottrell *et al*. 1988). Release of nitrogen during destruction of organic matter with increasing temperature can be substantial (Mullis 1987) and can continue to high-temperature metamorphic conditions with the release of ammonia (NH_3) from phyllosilicates, clays or micas (Bebout *et al*. 1999, Hurai *et al*. 2000, Sadofsky & Bebout 2000). In this study, the rocks are graphitic pelitic schists and thus have initially contained organic matter and large proportions of micas which may have stored NH_4^+. During the breakdown of K-micas during prograde metamorphism, or the alteration

of biotite and/or muscovite to clay minerals during later hydrothermal alteration, NH_4^+ can be liberated from the K-sites and released into the fluid phase; leading to the presence of a nitrogen-rich fluid during the metamorphism (Halam & Eugster 1976) and/or alteration of the pelitic schists. The reaction can be summarized as:

K^+ (aq) + NH_4-micas = NH_4^+ (aq) + K-micas. The following reactions:

$2NH_4^+ = N_2 + 8H^+$

$NH_4^+ + OH^- = NH_3 + H_2O$

$4NH_3 + 3O_2 = 2N_2 + 6H_2O$

could then result in the generation of N_2 from NH_4^+, leading to a decrease in pH of the fluid, and consumption of O_2; thus acting as a powerful reducing agent (Dee & Roberts 1993, Crawford & Hollister 1986).

The occurrence of graphite in the pelitic schists can lead to the reaction between graphite and aqueous metamorphic fluids, probably migrating along shear zones, forming CH_4-bearing inclusions. There is abundant evidence that carbonic fluids are produced during metamorphism of organic-rich shales (Touret 2001, Schwab *et al*. 2005, Nabelek *et al*. 2003, Huff & Nabelek 2007), likely via the following reactions:

$2C+2H_2O \rightarrow CH_4 + CO_2$

or $C + 2H_2 \rightarrow CH_4$,

with H_2 resulting from the breakdown of NH_4^+ after being liberated during the alteration of the K-bearing minerals. However, the first equation yield equal amounts of CO_2 and CH_4. As no CO_2 fluid inclusion has been observed, except very small amounts of CO_2 in fluid inclusions dominated by CH_4 and N_2, the second equation most likely describes the reaction occurring in this study area. Another possibility is that CO_2 has been consumed by the precipitation of

carbonates or the reaction coupled with ammonia liberation from K-micas leading to the formation of N_2 and H_2 following $CO_2+4H_2=CH_4+2H_2O$. Thus, interaction of fluids with graphitic lithologies, as well as with different minerals phases such as biotite, and feldspar, led to the formation of a C-O-H fluid system, and potentially to the destruction of graphite.

The N_2-rich and CH_4-rich fluid inclusions co-exist in the graphitic pelitic schist, implying that these inclusions may have been trapped at the same time. High nitrogen concentrations are an important indicator of a metamorphic origin of fluids (Huff & Nabelek 2007). However, the variable CH_4–N_2 ratios in these inclusions suggest that the two components may have been derived from different source rocks/minerals; either CH_4 and N_2 coming directly from organic matter and/or mainly N_2 coming from phyllosilicate minerals (Huff & Nabelek 2007). These secondary inclusions within Q2 are considered to have been trapped after peak metamorphism, and thus the consumption of graphite to generate CH_4 and/or N_2 would have happened during and mainly after the formation of Q2.

These fluids are interpreted to have been trapped during retrograde metamorphism of the basement rocks at temperatures from about 500°C down to 250°C, and/or during the diagenetic hydrothermal alteration from 200 to 150°C. However, the pressures recorded at these temperatures by the isochores for these inclusions are too low with respect to the conditions prevailing during retrograde metamorphism and diagenetic hydrothermal alteration (Fig. 3-11). Therefore, these low pressures may be explained by reequilibration of the fluid inclusions at lower pressure(s), either during the protracted uplift of the basement before the deposition of the Athabasca sediments (stage 1 in Fig. 3-11), and/or during burial by the Athabasca basin sediment and their subsequent uplift (stage 2 in Fig. 3-11) from ca. 1760 – 1500 Ma (Ramaekers *et al*. 2007). The PT path followed by the rock after fluid inclusion formation, either during retrograde

metamorphism or burial by a thick sequence of sediments may lead to internal overpressure of fluid inclusions, leading to microfracturing and potential reduction in density as a result of fluid loss (*e.g.* Pêcher 1981, Goldstein 1986, Sterner & Bodnar 1989, Bodnar *et al.* 1989). The irregular shapes exhibited by some fluid inclusions in this study may be explained by reequilibration processes.

The presence of N_2-rich fluid inclusions in the RGZ, albeit rare, suggests interaction with a N_2-rich fluid similar to the one observed within the graphitic pelitic schists. The fluid may have been generated by the breakdown of NH_4 bearing K-phyllosilicate minerals, by interaction of a basinal fluid with organic matter present within the RGZ before it was consumed, or from fluids that were generated within the graphitic basement rocks and migrated laterally into the RGZ. This breakdown of NH_4^+ leads to the formation of N_2 and H_2, which can act as a reductant(s) for uranium mineralization.

Origin and Role of the Aqueous Fluids

The aqueous fluid inclusions show a wide range of temperature of homogenization between 69.1 and 275.0°C. Some of the variability in Th could be due to unidentified necking. However, in a given fluid inclusion assemblage the homogenization temperatures should be more consistent (Goldstein 2001). These fluid inclusions yield salinities ranging from 19.8 to 26.2 wt% equivalent NaCl-$CaCl_2$ for Lw1, from 25.9 to 27.4 wt% equivalent NaCl-$CaCl_2$ for Lw' and from 31.4 to 34.1 wt% equivalent NaCl-$CaCl_2$ for Lwh and Lwh' (Fig. 3-7). Two-phase fluid inclusions from Q2 tend to show lower salinities than the ones from the later Q3 veins, which may suggest that over time the fluid(s) became more saline. The highly saline fluid has a salinity of up to 34.1 wt% and is interpreted to contain both NaCl and $CaCl_2$, and is similar to fluids documented by Derome *et al.* (2005) for the McArthur River uranium deposit. The lower salinity

fluid inclusions, with Tmice ranging from -30 to -24°C (Lw1), are similar to those obtained from two-phase fluid inclusions (Lw1; Fig. 3-7) at McArthur River and P-Patch (Derome *et al*. 2005, Mercadier *et al*. 2010). In the same way, inclusions with the Tmice ranging from -35 to -30°C (Lw') could be interpreted as being equivalent to their two-phase fluid inclusions containing dominantly $CaCl_2$-rich brine (Lw'; Fig. 3-7). The three-phase fluid inclusions which contain a daughter mineral of halite (Lwh and Lwh') are also similar to those observed at the McArthur River (Derome *et al*. 2005) and P-Patch uranium deposits (Mercadier *et al*. 2010) and in similar deposits in the Kombolgie Basin in Australia (Derome *et al*. 2007). Derome *et al*. (2005) distinguished the characteristics of Lwh and Lwh' fluid inclusions based on the nature of the last phase to melt during the cooling (ice or hydrohalite, respectively). However in the present study, they cannot be differentiated because ice or hydrohalite melting in these three-phase fluid inclusions was not observed because neither ice nor hydrohalite nucleated. Therefore, after Derome *et al*. (2005) and Richard *et al*. (2010), the Lw1 and Lwh inclusions are interpreted to be representative of the NaCl-rich brine and the Lw' and Lwh' inclusions are interpreted as representative of the $CaCl_2$-rich brine. Thus, we speculate that $CaCl_2$-rich and NaCl-rich brines have also interacted within the RGZ at Dufferin Lake, as the microthermometric data are very similar to those from Derome *et al*. (2005) and Mercadier *et al*. (2010) (Table 3-3). The vapor phase of these two-phase fluid inclusions contains minor amounts of H_2, CH_4, N_2 and CO_2 (Derome *et al*. 2005).

Table 3-3. Comparison of the microthermometric characteristics of fluid inclusions from previous studies in different location in the Athabasca Basin

FI types	McArthur River Derome *et al*. (2005)	P-Patch Mercadier *et al*. (2010)	Dufferin Lake Zone This study
Lw1	-25°C< Tmice <-11.2°C 93.8°C<Th<210°C	-28.3°C<Tmice<-18.2°C 83.5°C <Th<193.5°C	-29.5°C<Tmice<-16.4°C 97.9°C<Th<275°C
Lw'	-58.8°C< Tmice<-30°C 58°C<Th<137°C	-44°C<Tmice<-30.8°C 66.9°C< Th<176.8°C	-35.5°C<Tmice <-30.5 °C 99.3°C<Th<181.3°C
Lwh-Lwh'	-58°C<Tmice<-24°C 99.5°C<TmNaCl<235°C	-43.1°C<Tmice (Lwh')<-34.5°C 121.3°C<TmNaCl<260.3°C 74.8°C<Th<183.7°C	Tmice : n.d 189.7°C<TmNaCl<239°C 69°C<Th<125.3°C

FI: Fluid inclusions, Tmice: Temperature of ice melting, TmNaCl: Temperature of halite dissolution, Th: Temperature of total homogenization (all inclusions homogenize to the liquid phase)

The NaCl-rich brine is interpreted to be the regional basinal fluid, observed elsewhere in the Athabasca Basin (Pagel 1975, Pagel & Jaffrezic 1977, Derome *et al*. 2005), and which percolated into the basement rocks in the RGZ below the unconformity along reactivated fault zones or microfractures. The $CaCl_2$-rich brine is interpreted to result from fluid/rock interaction between the NaCl-rich brines and Ca-rich rocks of the basement (Derome *et al*. 2005, Derome *et al*. 2007, Mercadier *et al*. 2010, Richard *et al*. 2010). Mixing between these two brines has been suggested by Derome *et al*. (2005) and Richard *et al*. (2010) to have occurred during uranium deposition. However, these brines are not observed in the graphitic pelitic schists in this study, but may be linked with the alteration of metamorphic minerals and their replacement by clay minerals and chlorite, and the dissolution of graphite in the RGZ.

Conclusions

This study provides constraints on the fluids that have interacted with the basement rocks, but as the inclusions are interpreted as secondary it is difficult to relate them in time. Nevertheless, several types of fluids have circulated in the basement rocks at DLZ, and we suggest that they may be related to specific geological (fluid) events that have affected these rocks. Also, it appears as though the fluids present in the upper part of the basement, *i.e.* within the RGZ profile, are different from the fluids found deeper in the less altered basement rocks.

Two types of brines in the RGZ have been documented in this study: the regional basinal NaCl-rich fluid and an evolved Ca-rich brine. These observations suggest that the regional basinal brines have circulated in the basement rocks and have been able to evolve by interaction with the basement rocks (Derome *et al*. 2005) to become a brine which could have interacted with regional basinal fluids and subsequently resulted in uranium precipitation. These brines have also been observed previously in other studies from other areas of the Athabasca Basin, such as at the McArthur River (Derome *et al*. 2005), P-Patch (Mercadier *et al*. 2010), Eagle Point, Rabbit Lake, P-Patch, and Millennium deposits (Richard 2009). Minor amounts of H_2, CH_4, N_2 and CO_2 have been detected irregularly in the highly saline aqueous inclusions by Derome *et al*. (2005).

Within the graphitic pelitic schists, two types of fluid have been observed, a CH_4-rich and a N_2-rich fluid. These fluids are interpreted to be the result of multiple fluid interactions with the graphitic lithologies along the retrograde PT path after peak metamorphism associated with the Trans-Hudson Orogen or with later fluids responsible for diagenetic hydrothermal alteration. The generation of these fluids likely resulted from the breakdown of graphite to CH_4 and associated feldspars and micas to NH_4^+ and N_2, and both CH_4 and NH_4^+ could represent possible reductants of the uranium-bearing brines, with NH_4^+ forming H_2 and N_2.

CHAPTER 4
SUMMARY AND CONCLUSIONS

In this study, we examined the graphitic schists (+/- sulfides) and their altered equivalents depleted in graphite and sulfides, in order to observe and document the consumption of graphite (and sulfides), and to characterize the different types of carbon species present in the graphitic samples. Also, we provided some new valuable information on the similarities and differences between the variably graphitic rocks and the ones depleted in graphite (and sulfides). Thus, we are able to offer new insights as to the processes that may have led to the consumption of graphite (and sulfides) in the basement rocks underlying uranium mineralization. The purpose of this M.Sc. project was to document the consumption of graphite in the basement rocks and to determine how and why it has been removed. An additional aim was also to determine the possible relationship between graphite and/or its breakdown in the mineralization of uranium, and thus, determine if the location of graphitic conductors is still important for the localization of a deposit.

Comparison of the Characteristics of Graphite-Bearing and Graphite-Depleted Rocks

Chapter 2 of this thesis documented the depletion of graphite and associated sulfides, in the upper part of the basement at Dufferin Lake Zone. This confirmation is based on macroscopic, petrographic, geochemical and Raman analyses. The graphitic pelitic schists and the graphite-depleted rocks are texturally very similar which confirm that the rocks were similar mineralogically before alteration occurred but some process or combination of processes removed graphite. Our analyses show that the graphite-depleted rocks are the result of fluid-rocks interactions, in particular within the bleached zone, leading to gain and loss in some elements, including loss in C and S, compared to the variably graphitic pelitic schists. Several

events through time could be responsible for this consumption, by breaking down graphite and carbonaceous matter (and sulfides), resulting in the migration of C (and S) as gas or fluid (*i.e.* rich in CH_4) upward to and above the unconformity, where it could have played a role in uranium mineralization, as suggested by Hoeve & Sibbald (1978). This depletion of graphite could have started during the retrograde metamorphism, and continued through paleoweathering, and finally consumed during fluid-rock interaction with basin brines, as described in Chapter 3.

Chapter 3 documents the characteristics of the different fluids that have interacted with the graphitic pelitic schists and their equivalent graphite-depleted rocks. This chapter documents the presence of carbonic CH_4 –rich fluids and N_2-rich fluids in the graphitic pelitic schists. These demonstrate the interaction of multiple fluids with graphitic lithologies. CH_4 is generated by the breakdown of graphite, and N_2 by the breakdown of feldspar and micas, where it has been stored after being liberated from carbonaceous matter. These are possible reductants for uranium-mineralization. In the upper part of the basement, within the RGZ, where graphite is not present anymore, basinal brines rich in NaCl and $CaCl_2$ are observed. These fluids have been observed elsewhere in the Athabasca Basin, and are interpreted to be the regional basinal fluid and the evolved fluid resulting from fluid/rock interactions, respectively. The latter is possibly related to uranium mineralization. By having circulated in the upper part of the basement, where graphite is missing, these fluids could be responsible for the consumption of graphite, having reacted with graphite and leading to its breakdown to CH_4 that could have act as a reductant for uranium mineralization. A few N_2-rich fluid inclusions have been observed in this graphite-depleted zone, which could be the result of interaction with former organic matter present in the RGZ.

Implications for Graphite Consumption, Uranium Exploration, and Future Research

The aim of this study was to confirm and document the depletion of graphite in the basement rocks underlying the Dufferin Lake Zone in the south-central Athabasca Basin, and to try to understand the mechanism(s) which could be responsible for this depletion. In addition, an attempt was made to link the changes to the basement rocks to the PT-t path followed by these rocks. In summary we documented the following through PT-t space:

1. During prograde metamorphism:
    a. Former black shales, rich in carbonaceous (organic) matter, were metamorphosed to graphitic pelitic schists.
    b. NH_4^+ was liberated from the carbonaceous matter and stored in K-micas, and the carbonaceous matter became more ordered and crystalline (semi-graphite to graphite).
    c. Q1 was formed during the peak metamorphism.
2. During retrograde metamorphism:
    a. Fluids interacted with the graphitic basement rocks, leading to the breakdown of graphite to CH_4 and the liberation of NH_4^+ from the phyllosicilicates minerals, which led to the formation of N_2 following $2NH_4^+ = N_2 + 8H^+$. Thus, a C-O-H fluid is formed. This fluid is interpreted as the one responsible for incipient graphite consumption (stage 1 – Fig. 4-1), during the uplift.
    b. Pre-Athabasca Q2 veins formed.
    c. Pre-Athabasca paleoweathering took place (stage 2 – Fig. 4-1), altering the upper part of the basement, and leading to the formation of the RGZ (Macdonald 1980, 1985). This step leaked varying proportions of C and S.

d. Athabasca Basin is filled, and post-Athabasca Q3 and younger Q4 veins are formed.

e. Post-Athabasca circulation of oxidized basinal brines and hydrothermal alteration events (stage 3 – Fig. 4-1) occurred in the basement. These events kept altering the upper part of the basement (RGZ) and produced the bleached zone which overprints the regolith profile. These brines reacted with the variably graphitic schists and thus, depleted graphite and sulfides, by breaking them down. This resulted in the migration of C and S as fluid and/or gas to the unconformity, or above, using the original graphite-sulfide-rich fault structures.

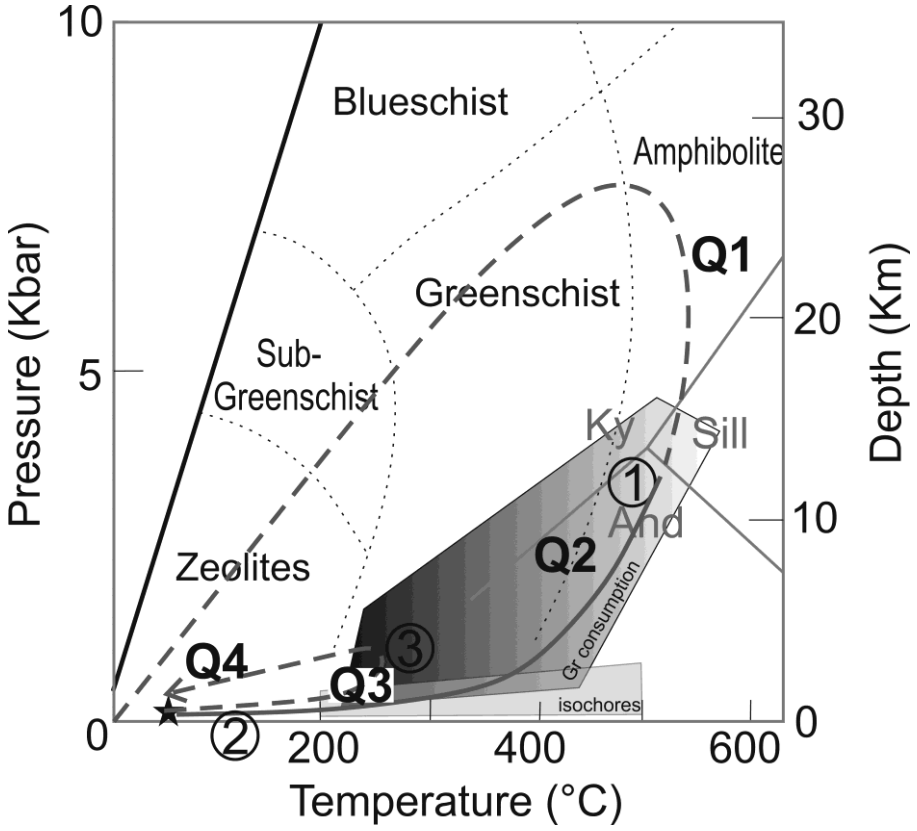

Figure 4-1. Pressure – Temperature diagram (Chapter 2) illustrating fluid inclusions isochores of graphitic pelitic schists and the different quartz (Chapter 3), as well as the different steps in graphite depletion

Thus, several events are considered to be responsible for graphite consumption. However, graphite-depletion seems to be more prevalent with decreasing pressure along retrograde PT-t paths (Ault & Selverstone 2008), in particular near the end (*i.e.* lower temperature part) of the retrograde metamorphism. Therefore, the late retrograde and diagenetic hydrothermal alterations are interpreted to be the processes that have played the most important role in the depletion/consumption of graphite. This is supported by the fact that the bleached zone has no graphite. Also, this is the most altered zone with evidence of hosting the most important fluid-rock interactions, including the one(s) that can be related to uranium mineralization. The interaction of fluids with early graphite led to its consumption and to the formation of CH_4 (as observed in the fluid inclusion study of this thesis – Chapter 3). As a result of upward migration of gases (and associated fluids), interaction with U bearing oxidized basinal fluids could have occurred above the unconformity whereby it could have produced a reductant for eventual uranium mineralization. This could explain why the Dufferin Lake uranium deposit is located in the sandstones.

To further advance these hypotheses, future research work should focus on determining the carbon isotopes of the different carbon species, in order to distinguish between metamorphic graphite and fluid-deposited graphite (Luques *et al*. 2012), and to determine their physiochemical conditions of origin. HRTEM investigations complemented with Raman analysis would also give more physiochemical information on the degree/state of carbon organization (Beyssac *et al* 2002b).

Also, future research work on the sandstone units, lying immediately above the unconformity, should be carried out to identify the geochemical signature and pathfinder potential of C and S species, which resulted from the upward migration of the carbon and sulfur, from the destruction

of graphite and sulfides, respectively. Previous studies have already identified some hydrocarbons in the sandstone, which could be the result of the carbon migration (Hoeve & Sibbald 1978, Landais 1996)

Other potential research studies, based on the known composition(s) of the basinal brine and the known P-T of formation, include the experimental testing of the interaction of basinal brines of different compositions with graphite, so to answer the question whether a fluid or a combination of fluids and gases under these conditions could really consume (*i.e.* break down) supposedly inert graphite.

This study has provided relative age constraints on the processes operating in this part of the basin, but the absolute age of these processes with respect to the timing of uranium mineralization is still not known.

REFERENCES

Aghbelagh, Y.B., & Yang, J. (2014) Effect of graphite zone in the formation of unconformity-related uranium deposits: insights from reactive mass transport modeling. *Journal of Geochemical Exploration*, doi: 10.1016/j.gexplo.2014.01.020.

Alexandre, P., & Kyser, K. (2006) Geochemistry of uraniferous bitumen in the southwest Athabasca Basin, Saskatchewan, Canada. *Economic Geology* 101, 1605-1612.

Alexandre, P., Kyser, K., Jiricka, D., & Witt, G. (2012) Formation and evolution of the Centennial unconformity-related uranium deposit in the south-central Athabasca Basin, Canada. *Economic Geology* 107, 385-400.

Alexandre, P., Kyser, K., Polito, P., & Thomas, D. (2005) Alteration mineralogy and stable isotope geochemistry of Paleoproterozoic basement-hosted unconformity-type uranium deposits in the Athabasca Basin, Canada. *Economic Geology* 100, 1547-1563.

Annesley, I.R., & Millar, R. (2011) Tourmaline- and sulfide-bearing graphitic pelitic gneisses of the Paleoproterozoic Wollaston Group, northern Saskatchewan: new insights into understanding the carbon-sulfur-boron-uranium geochemical system with implications for U/C-type uranium deposits. 25th IAGS, Finland.

Annesley, I.R., & Wheatley, K. (2011) Insights into understanding the carbon-uranium (± sulfur and boron) geochemical system along a retrograde P-T-t path from 600°C to 250°C: New constraints with implications for U/C-type uranium deposits. GAC MAC 2011 Annual meeting, May 2011.

Annesley, I.R., Madore, C., & Cutler, J. (2001) Synchrotron X-Ray analysis of graphtic pelitic gneisses in the vicinity of unconformity-type uranium mineralization. *In* Summary of Investigations 2001, Saskatchewan Geological Survey, Saskatchewan Energy and Mines, Miscellaneous Report 4(2), 132-140.

Annesley, I.R., Madore, C., & Portella, P. (2005) Geology and thermotectonic evolution of the western margin of the Trans-Hudson Orogen: evidence from the eastern sub-Athabasca basement, Saskatchewan. *Canadian Journal of Earth Sciences* 42, 573–597.

Ault, K.A., & Selverstone, J. (2008) Microtextural constraints on the interplay between fluid–rock reactions and deformation. *Contributions to Mineralogy and Petrology* 156, 501–515.

Bakker, R.J. (1999) Adaptation of the Bowers and Helgeson (1983) equation of state to the H2O–CO2–CH4–N2–NaCl system. *Chemical Geology* 154, 225–236.

Bebout, G.E., Cooper, D.C., Bradley, A.D., & Sadofsky, S.J. (1999) Nitrogen-isotope record of fluid-rock interactions in the Skiddaw aureole and granite, English Lake District. *American Mineralogist* 84, 1495–1505.

Berman, R.G., Pehrsson S., Davis, W.J., Ryan, J.J., Qui, H., & Ashton, K.E. (2013) The Arrowsmith orogeny: Geochronological and thermobarometric constraints on its extent and tectonic setting in the Rae craton, with implications for pre-Nuna supercontinent reconstruction. *Precambrian Research* 232, 44–69.

Berman, R.G., Sanborn-Barrie, M., Stern, R.A., & Carson, C.J. (2005) Tectonometamorphism at ca. 2.35 and 1.85 Ga in the Rae Domain, western Churchill Province, Nunavut, Canada: Insights from structural, metamorphic and in situ geochronological analysis of the southwestern Committee Bay Belt. *Canadian Mineralogist* 43, 409-442.

Beyssac, O., Brunet, F., Petitet, J.P., Goffé, B., & Rouzaud, J.N. (2003a) Experimental study of the microtextural and structural transformations of carbonaceous materials under pressure and temperature. *European Journal of Mineralogy* 15, 937–951.

Beyssac, O., Goffé, B., Chopin, C., & Rouzaud, J.N. (2002a) Raman spectra of carbonaceous material in metasediments: a new geothermometer. *Journal of Metamorphic Geology* 20, 859–87.

Beyssac, O., Goffé, B., Petitet, J.P., Froigneux, E., Moreau, M., & Rouzaud, J.N. (2003b) On the characterization of disorder and heterogeneous carbonaceous materials by Raman spectroscopy. *Spectrochimica Acta*, Part A 59, 2267–2276.

Beyssac, O., Goffé, B., Rouzaud, J.N., Clinard, C., Cassareuil, J., & Catel, N. (1999) From Anthracites to Graphite: Influence of Temperature, Pressure and Shear. *In* Prospects for Coal Science in the 21st Centrury (Li, B.Q. & Liu, Z.Y., eds.). Shanxi Science & Technology Press, 29-32.

Beyssac, O., Rouzaud, J.N., Goffé, B., Brunet, F., & Chopin, C. (2002b) Graphitization in a high pressure, low temperature metamorphic gradient: A Raman microspectroscopy and HRTEM study. *Contributions to Mineralogy and Petrology* 143, 19–31.

Bodnar, R.J., Binns, P.R., & Hall, D.L. (1989) Synthetic fluid inclusions. VI. Quantitative assessment of the decrepitation characteristics of fluid inclusions in quartz at one atmosphere confining pressure. *Journal of Metamorphic Geology* 7, 229-242.

Bottrell, S.H., Carr, L.P., & Dubessy, J. (1988) A nitrogen-rich metamorphic fluid and coexisting minerals in slates from North Wales. *Mineralogical Magazine* 52, 451-457.

Boynton, W. (1984) Geochemistry of the rare earth elements: meteorite studies. *In* Rare Earth Element Geochemistry (Henderson, P. eds.). Elsevier, 63-114.

Bustin, R.M., Ross, J.V., & Rouzaud, J.N. (1995) Mechanics of graphite formation from kerogen: experimental evidence. *International Journal of Coal Geology* 28, 1–36.

Cai, C.F., Li, H.T., Qin, M.K., Luo, X.R., Wang, F.Y., & Ou, G.X. (2007) Biogenic and petroleum-related ore-forming processes in Dongsheng uranium deposit, NW China. *Ore Geology Reviews* 32, 262-274.

Card, C.D. (2002) New investigations of basement to the western Athabasa Basin. *In* Saskatchewan Summary of Investigations 2002, Saskatchewan Geological Survey, Saskatchewan Energy and Mines, Miscellaneous Report 4(2), p 17.

Card, C.D. (2009) Cree South project 2009: reconnaissance bedrock mapping in the Lloyd Domain and Virgin River Shear Zone. *In* Summary of Investigations 2009, Saskatchewan Geological Survey, Saskatchewan Energy and Mines, Miscellaneous Report 4(2), Paper A-7, 21p.

Card, C.D. (2012) A proposed domainal reclassification for Saskatchewan's Hearne and Rae provinces. *In* Summary of Investigations 2012, Saskatchewan Geological Survey, Saskatchewan Energy and Mines, Miscellaneous Report 4(2), p 9.

Card, C.D., & Annesley, I.R. (2012) The origin(s) of Graphite-rich Rocks in the Wollaston-Mudjatik Transition Zone: Syngenetic Versus Epigenetic? Saskatchewan Geological Survey, Open House 2012, abstract volume, p 6.

Card, C.D., & Bosman, S.A. (2007) The Cree Lake South Project: reconnaissance bedrock mapping in the Mudjatik and Virgin River Domains, and the Virgin River Shear Zone near the southwest margin of the Athabasca Basin. *In* Summary of Investigations 2007, Saskatchewan Geological Survey, Saskatchewan Energy and Mines, Miscellaneous Report 4(2), p 22.

Card, C.D., McEwan, B., & Bosman, S.A. (2008) The Cree Lake South Project 2008: Regional Implications of Bedrock mapping along the Virgin River Transect. *In* Saskatchewan

Summary of Investigations 2008, Saskatchewan Geological Survey, Saskatchewan Energy and Mines, Miscellaneous Report 4(2), p 23.
Card, C.D., Pana, D., Portella, P., Thomas, D.J., & Annesley, I.R. (2007) Basement rocks to the Athabasca Basin, Saskatchewan and Alberta. *In* EXTECH IV: Geology and Uranium EXploration TECHnology of the Proterozoic Athabasca Basin, Saskatchewan and Alberta (C.W. Jefferson & G. Delaney eds.). Geological Survey of Canada 588, 69-87.
Chi, G.X., & Ni, P. (2007) Equations for calculation of NaCl/(NaCl+CaCl2) ratios and salinities from hydrohalite-melting and ice-melting temperatures in the H2O-NaCl-CaCl2 system. *Acta Petrologica Sinica* 23, 33-37.
Condie, K.C. (1993) Chemical composition and evolution of the upper continental crust: Contrasting results from surface samples and shales. *Chemical Geology* 104, 1-37.
Crawford, M.L., & Hollister, L.S. (1986) Metamorphic fluids: The evidence from fluid inclusions. *In* Fluid-Rock Interactions during Metamorphism (Walther, J.V., & Wood, B .J., eds.). Springer-Verlag, New York, pp 1–35.
Crespo, E., Luque, J., Fernandez-Rodriguez, C., Rodas, M., Diaz-Azpiroz, M., Fernandez-Caliani, C.J., & Barrenechea, J.F. (2004) Significance of graphite occurrences in the Aracena Metamorphic Belt, Iberian Massif. *Geological Magazine* 141, 687-697.
Cuesta, A., Dhamelincourt, P., Laureyns, J., Martinez-Alonso, A., & Tascon, J.M.D. (1994) Raman microprobe studies on carbon materials. *Carbon* 32, 1523–1532.
Cuney, M. (2010) Evolution of Uranium Fractionation Processes through Time: Driving the Secular Variation of Uranium Deposit Types. *Economic Geology* 105, 553–569.
Cuney, M., Brouand, M., Cathelineau, M., Derome, D., Freiberger, R., Hecht, L., Kister, P., Lobaev, V., Lorilleux, G., Peiffert, C., & Bastoul, A.M. (2003) What parameters control the high grade-large tonnage of the Proterozoic unconformity related uranium deposit? *In* Uranium Geochemistry 2003, International Conference, April 13-16, 2003, Proceedings, (Cuney, M., ed.). Unité Mixte de Recherche CNRS 7566G2R, Université Henri Poincaré, Nancy, France, p. 123-126.
Dee, S.J., & Robert, S. (1993) Late-kinematic gold mineralization during regional uplift and the role of nitrogen: an example from the La Codosera area, W. Spain. *Mineralogical Magazine* 57, 437-450.
Derome, D., Cathelineau, M., Cuney, M., Fabre, C., & Lhomme, T. (2005) Evidences of brine mixings in the McArthur River unconformity-type uranium deposit (Saskatchewan, Canada). Implications on genetic models. *Economic Geology* 100, 1529–1545.
Derome, D., Cathelineau, M., Fabre, C., Boiron, M.-C, Banks, D., Lhomme, T., & Cuney, M. (2007) Reconstitution of paleo-fluid composition by Raman, LIBS and crush-leach techniques: application to mid-proterozoic evaporitic brines (Kombolgie formation basin, northern territories, Australia). *Chemical Geology* 237, 240-254.
Dubessy, J., Poty, B., Ramboz, C. (1989) Advances in C–O–H–N–S fluid geochemistry based on micro-Raman spectrometric analysis of fluid inclusions. *European Journal of Mineralogy* 1, 517–534.
Fayek, M., & Kyser, T.K. (1997) Characterization of multiple fluid-flow events and rare-earth-element mobility associated with formation of unconformity-type uranium deposits in the Athabasca Basin, Saskatchewan. *Canadian Mineralogist* 35, 627–658.
Ferrari, A.C. & Robertson, J. (2000) Interpretation of Raman spectra of disordered and amorphous carbon. *Physical Review B* 61, 14095-14107.

Ferrari, A.C., & Basko, D.M. (2013) Raman spectroscopy as a versatile tool for studying the properties of graphene. *Nature Nanotechnology* 8, 235-246.
French, B.M. (1966) Some Geological Implications of Equilibrium between Graphite and a C-H-O Gas Phase at High Temperatures and Pressures. *Reviews of Geophysics* 4(2), 223-253.
Geological Atlas of Saskatchewan, Saskatchewan Energy and Resources, version 16 (2013) Miscellaneous Report 2013-7. http://www.infomaps.gov.sk.ca/website/SIR_Geological_Atlas/viewer.htm
Gilboy, C.F. (1985a) Basement geology, part of the Cree Lake (south) area. Saskatchewan Energy and Mines, Report 203, 1-47.
Gilboy, C.F. (1985b) Compilation bedrock Geology, Cree Lake, NTS Area 74G. Saskatchewan Energy and Mines, Report 237.
Goldstein, R.H. (1986) Reequilibration of fluid inclusions in low-temperature calcium-carbonate cement. *Geology* 14, 792-795.
Goldstein, R.H. (2001) Fluid inclusions in sedimentary and diagenetic systems. *Lithos* 55, 159-193.
Grant, J.A. (1986) The isocon diagram, a simple solution to Gresens' equation for metasomatic alteration. *Economic Geology* 81, 1976–1982.
Hoeve, J., & Quirt, D. (1984) Mineralization and host rock alteration in relation to clay mineral diagenesis and evolution of the middle Proterozoic Athabasca basin, northern Saskatchewan, Canada. Saskatchewan Research Council Technical Report 187, 187 p.
Hoeve, J., & Quirt, D. (1987) A stationary redox front as a critical factor in the formation of high grade, unconformity-type uranium ores in the Athabasca basin, Saskatchewan, Canada. *Bulletin Minéralogie*, 110, 151–171.
Hoeve, J., & Sibbald, T. (1978) On the Genesis of Rabbit Lake and Other Unconformity-type Uranium Deposits in Northern Saskatchewan, Canada. *Economic Geology* 73, 1450-1473.
Hoeve, J., Sibbald, T.I.I., Ramaekers, P., & Lewry, J.F. (1980) Athabasca Basin unconformity-type uranium deposits: a special class of sandstone-type deposits. *In* Uranium in the Pine Creek Geosyncline, (S. Ferguson & A. Goleby, eds). *International Atomic Energy Agency, Vienna, Austria*, 575-594.
Hoffman, P.F. (1988) United plates of America, the birth of a craton: Early Proterozoic assembly and growth of Laurentia. *Annual Review of Earth and Planetary Sciences* 16, 543-603.
Hoffman, P.F. (1990) Subdivision of the Churchill Province and extent of the Trans-Hudson orogeny. In The Early Proterozoic Trans-Hudson Orogen of North America (Lewry, J.F. & Stauffer, M.R., eds.). *Geological Association of Canada*, Special Paper 37, 15-39.
Huff, T.A., & Nabelek, P.I. (2007) Production of carbonic fluids during metamorphism of graphitic pelites in a collisional orogen—An assessment from fluid inclusions. *Geochimica et Cosmochimica Acta* 71, 4997–5015.
Huizenga, J.M & Touret, J.L.R. (2012) Granulites, CO2 and graphite. *Gondwana Research* 22, 799-809.
Huizenga, J.M. (2010) Thermodynamic modelling of a cooling C–O–H fluid–graphite system: implications for hydrothermal graphite precipitation. *Mineralium Deposita* 46(1), 23-33.
Hurai, V., Janak, M., Ludhova, L., Horn, E.E., Thomas, R., & Majzlan, J. (2000) Nitrogen-bearing fluids, brines and carbonate liquids in Variscan migmatites of the Tatra Mountains, Western Carpathians; heritage of high-pressure metamorphism. *European Journal of Mineralogy* 12, 1283–1300.

Jefferson, C.W., Thomas, D.J., Gandhi, S.S., Ramaekers, P., Delaney, G., Brisbin, D., Cutts, C., Portella, P., & Olson, R.A. (2007) Unconformity associated uranium deposits of the Athabasca Basin, Saskatchewan and Alberta. *In* EXTECH IV: Geology and Uranium EXploration TECHnology of the Proterozoic Athabasca Basin, Saskatchewan and Alberta, (Jefferson, C.W., & Delaney, G., eds.). *Geological Survey of Canada*, Bulletin 588, 23–67.

Jehlicka, J., Urban, O., & Pokorny, J. (2003) Raman spectroscopy of carbon and solid bitumens in sedimentary and metamorphic rocks. *Spectrochimica Acta part A* 59, 2341-2352.

Jiricka, D.E., & Leppin, M. (2003) Virgin River Project 2003 Annual Exploration Report Mineral Claims: S-7794, S-7795, S-105678 and S-105679, NTS 74G/5 and 74G/12. Unpublished internal report for Cameco Corporation.

Jiricka, D.E., & Witt, G. (2002) Virgin River Project 2002 Annual Exploration Report Mineral Claims: S-7794 and S-7795, NTS 74G/11 and 74G/12. Unpublished internal report for Cameco Corporation.

Jiricka, D.E., Witt, G., & Fiolleau, K. (2007) Southwest Athabasca Project. 2006 annual exploration report. Internal Cameco report, 1-77.

Johnson, R.L. (1968) The Geology of the Nyberg Lakes Area (West Half), Saskatchewan. Saskatchewan Mineral Resources Report 118, p 15.

Komninou, A., & Sverjensky, D.A. (1996) Geochemical modeling of the Formation of an Unconformity-Type uranium Deposit. *Economic Geology* 91, 590-606.

Kotzer, T.G., & Kyser, T.K. (1990) The use of stable and radiogenic isotopes in the identification of fluids and processes associated with unconformity-type uranium deposits. In Modern Exploration Techniques. *Saskatchewan Geological Society*, Special Publication 10, 115-131.

Kotzer, T.G., & Kyser, T.K. (1995) Petrogenesis of the Proterozoic Athabasca Basin, northern Saskatchewan, Canada, and its relation to diagenesis, hydrothermal uranium mineralization and paleohydrogeology. *Chemical Geology* 120, 45-89.

Kotzer, T.G., Kyser, T.K., & Irving, E. (1992) Paleomagnetism and the evolution of fluids in the Proterozoic Athabasca Basin, Northern Saskatchewan, *Canadian Journal of Earth Sciences* 29, 1474-1491.

Kribek, B., Hrabal, J., Landais, P., & Hladikova, J. (1994) The association of poorly ordered graphite, coke and bitumens in greenschist facies rocks of the Ponikla Group, Lugicum, Czech Republic; the result of graphitization of various types of carbonaceous matter. *Journal of Metamorphic Geology* 12, 493-503.

Kwiecińska, B., & Nowak, G. (1997) Highly metamorphosed coal from the Lower Silesian coal basin (SW Poland). *In* Proceedings of the XIII International Congress on The Carboniferous and Permian, (Podemski, M., Dybova, J.S., Jaworowski, K., Jureczka, J., & Wagner, R., eds.). *Prace Panstwowego Instytutu Geologicznego* 157(2), 547-255.

Kwiecińska, B., & Petersen, H.I. (2004) Graphite, semi-graphite, natural coke, and natural char classification—ICCP system. *International Journal of Coal Geology* 57, 99-116.

Kyser, T.K., Wilson, M.R., & Ruhrmann, G. (1989) Stable isotope constraints on the role of graphite in the genesis of unconformity-type uranium deposits. *Canadian Journal of Earth Sciences* 26(3), 490-498.

Landais, P. (1996) Organic geochemistry of sedimentary uranium ore deposits. *Ore Geology Reviews* 11, 33-51.

Landais, P., & Dereppe, J.M. (1985) A chemical study of the carbonaceous material from the Carswell Structure. In The Carswell Structure Uranium Deposits, Saskatchewan, (Lainé,

R., Alonso, D., & Svab, M., ed.). *Geological Association of Canada*, Special paper 29, 165-174.
Landais, P., Dubessy, J., Dereppe, J.M., & Philp, R.P. (1993) Characterization of graphite alteration and bitumen genesis in the Cigar Lake deposit (Saskatchewan, Canada). *Canadian Journal of Earth Sciences* 30(4), 743-753.
Lopez-Moro, F.J. (2012) EASYGRESGRANT—A Microsoft Excel spreadsheet to quantify volume changes and to perform mass-balance modeling in metasomatic systems. *Computers & Geosciences* 39, 191–196.
Lorilleux, G., Cuney, M., Jébrak, M., Rippert, J.C., & Portella, P. (2003) Chemical brecciation processes in the Sue unconformity-type uranium deposits, Eastern Athabasca Basin (Canada). *Journal of Geochemical Exploration* 80, 241–258.
Luque, F.J., Crespo-Feo, E., Barrenechea, J.F., & Ortega, L. (2012) Carbon isotopes of graphite: Implications on fluid history. *Geoscience Frontiers* 3(2), 197–207.
Luque, F.J., Pasteris, J.D., Wopenka, B., Rodas, M., & Barrenechea, J.F. (1998) Natural fluid deposited graphite: mineralogical characteristics and mechanisms of formation. *American Journal of Science* 298, 471-498.
Macdonald, C. (1980) Mineralogy and geochemistry of a Precambrian regolith in the Athabasca Basin. M.Sc. Thesis: University of Saskatchewan, 151 p.
Macdonald, C. (1985) Mineralogy and geochemistry of the sub-Athabasca regolith near Wollaston Lake. *In* Geology of Uranium Deposits, Proceedings of the CIM-SEG Uranium Symposium, September 1981(Sibbald, T.I.I., & Petruk, W., eds.). *The Canadian Institute of Mining and Metallurgy*, Special Volume 32, 155-158.
Madore, C., & Annesley, I.R. (1997) Graphitic pelitic gneisses of the paleoproterozoic Wollaston Group, Hearne Province, Saskatchewan. *In* Mineral deposits, Research and Exploration-Where do they meet? (Papunen, H., ed.). Balkema, 79-82.
McCready, A.J., & Annesley, I.R. (2006) Deciphering EM target conductor responses in the Atahabasca Basin with Raman and synchrotron spectroscopy: applications and benefit to uranium exploration. GAC-MAC Montreal 2006.
McCready, A.J., Annesley, I.R., Parnell, J., & Richardson, L.C. (1999a) Morphology, chemistry, and origin of carbonaceous matter from the McArthur River deposit, Saskatchewan, Canada. *In* Mineral Deposits: Processes to Processing (Stanley, C.J., *et al*., eds.). Balkema, 251-254.
McCready, A.J., Annesley, I.R., Parnell, J., & Richardson, L.C. (1999b) Uranium-bearing carbonaceous matter, McArthur River uranium deposit, Saskatchewan. *In* Saskatchewan Summary of Investigations 1999, Saskatchewan Geological Survey, Saskatchewan Energy and Mines, Miscellaneous Report 4(2), 110-120.
Mercadier, J., Cuney, M., Cathelineau, M., & Lacorde, M. (2011) U redox fronts and kaolinisation in basement-hosted unconformity-related U ores of the Athabasca Basin (Canada): late U remobilization by meteoric fluids. *Mineralium Deposita* 46, 105-135.
Mercadier, J., Richard, A., & Cathelineau, M. (2012) Boron- and magnesium-rich marine brines at the origin of giant unconformity-related uranium deposits: δ11B evidence from Mg-tourmalines. *Geology* 40, 231-234.
Mercadier, J., Richard, A., Boiron, M.-C., Cathelineau, M., & Cuney, M. (2010) Migration of brines in the basement rocks of the Athabasca Basin through microfracture networks (P-Patch U deposit, Canada). *Lithos* 115, 121–136.

Mullis, J. (1987) Fluid inclusion studies during very low-grade metamorphism. *In* Low Temperature Metamorphism (Frey, M., ed.). Chapman and Hall, New York, pp. 162–199.
Nabelek, P.I., Wilke, M., Huff, T.A., & Wopenka, B. (2003) Methane, an important component of fluids in graphitic metapelites. *Geochimica et Cosmochimica Acta* 67, A317.
Nemanich, R.J., & Solin, S.A. (1979) First- and second-order Raman scattering from finite-size crystals of graphite. *Physical Review B* 20, 392-401.
Nover, G., Stoll, J.B., & Von der Gönna, J. (2005) Promotion of graphite formation by tectonic stress - a laboratory experiment. *Geophysical Journal International* 160, 1059–1067.
Orrell, S.E., Bickford, M.E., & Lewry, J.F. (1999) Crustal evolution and age of thermotectonic reworking in the western hinterland of the Trans-Hudson Orogen, northern Saskatchewan. *Precambrian Research* 95, 187–223.
Ortega, L., Millward, D., Luque, F.J., Barrenechea, J.F., Beyssac, O., Huizenga, J.M., Rodas, M., & Clarke, S.M. (2010) The graphite deposit at Borrowdale (UK): a catastrophic mineralizing event associated with Ordovician magmatism. *Geochimica et Cosmochimica Acta* 74, 2429-2449.
Pagel, M. (1975) Détermination des conditions physico-chimiques de la silicification diagénétique des grès Athabasca (Canada) au moyen des inclusions fluides. Comptes Rendus Académie Sciences Paris 280, 2301–2304.
Pagel, M., & Jaffrezic, H. (1977) Analyses chimiques des saumures des inclusions du quartz et de la dolomite du gisement d'uranium de Rabbit Lake (Canada). Aspect méthodologique et importance génétique. *Comptes Rendus Académie Sciences Paris* 284, 113–116.
Pagel, M., Poty, B., & Sheppard, S.M.F. (1980) Contribution to some Saskatchewan uranium deposits mainly from fluid inclusion and isotopic data. *In* International Uranium Symposium on the Pine Creek Geosyncline (ed) IAEA Vienna, pp 639–654.
Pana, D., Creaser, R.A., Muehlenbachs, K., & Wheatley, K. (2007) Basement geology in the Alberta portion of the Athabasca Basin: context for the Maybelle River area. *In* EXTECH IV: Geology and Uranium EXploration TECHnology of the Proterozoic Athabasca Basin, Saskatchewan and Alberta (Jefferson, C.W., & Delaney, G., eds.). *Geological Survey of Canada, Bulletin* 588, 135-153.
Pascal, M., Ansdell, K., Annesley, I.R., Boiron, M.-C., Kotzer, T., Jiricka, D., & Cuney, M. (2013) Microthermometric and Raman analysis of fluids that interacted with variably graphitic pelitic schist in the Dufferin Lake zone, south-central Athabasca Basin: Implications for graphite loss and uranium deposition. Goldschmidt 2013 Conference abstracts, p1930.
Pascal, M., Ansdell, K., Annesley, I.R., Jiricka, D., & Kotzer, T. (2013) Petrography and geochemistry of the pelitic schist in the Dufferin Lake Zone, south central Athabasca Basin, Saskatchewan, Canada. 12th SGA Biennial Meeting 2013, S3.13 Uranium and thorium deposits, p31.
Pasteris, J. (1989) In situ analysis in geological thin-sections by laser Raman microprobe spectroscopy - a cautionary note. *Applied Spectroscopy* 43, 567-570.
Pasteris, J.D., & Wopenka, B. (1991) Raman spectra of graphite as indicators of degree of metamorphism. *Canadian Mineralogist* 29, 1-9.
Pêcher, A. (1981) Experimental decrepitation and re-equilibration of fluid inclusions in synthetic quartz. *Tectonophysics* 78, 565-576.

Pimenta, M.A., Dresselhaus, G., Dresselhaus, M.S., Cancado, L.G., Jorio A. & Saito, R. (2007) Studying disorder in graphite-based systems by Raman spectroscopy. *Physical Chemistry Chemical Physics* 9, 1276–1291.

Powell, B., Wood, G., & Bzdel, L. (2007) Advances in Geophysical Exploration for Uranium Deposits in the Athabasca Basin. *In* Proceedings of Exploration 07: Fifth Decennial International Conference on Mineral Exploration (Milkereit, B., ed.), 771-790.

Raffensperger, J.P., & Garven, G. (1995) The formation of unconformity-type uranium ore deposits coupled hydrochemical modeling. *American Journal of Science* 295, 639-696.

Rahl, J.M., Anderson, K.M., Brandon, M.T., & Fassoulas, C. (2005) Raman spectroscopic carbonaceous material thermometry of low-grade metamorphic rocks: calibration and application to tectonic exhumation in Crete, Greece. *Earth and Planetary Science Letters* 240, 339–354.

Ramaekers, P., Jefferson, C.W., Yeo, G.M., Collier, B., Long, D.G.F., Drever, G., McHardy, S., Jiricka, D., Cutts, C., Wheatley, K., Catuneanu, O., Bernier, S., Kupsch, B., & Post, R.T. (2007) Revised geological map and stratigraphy of the Athabasca Group, Saskatchewan and Alberta. *In* EXTECH IV: Geology and Uranium EXploration TECHnology of the Proterozoic Athabasca Basin, Saskatchewan and Alberta (Jefferson, C.W., & Delaney, G., ed.). *Geological Survey of Canada Bulletin* 588,155–191.

Ray, J. (2009) Carbon isotopic variations in fluid-deposited graphite: evidence for multicomponent Rayleigh isotopic fractionation. *International Geology Review* 51, 45-57.

Reid, K., Ansdell, K., Jiricka, D., Witt, G., & Card, C. (2014) Regional setting, geology and paragenesis of the Centennial unconformity-related uranium deposit, Athabasca Basin, Saskatchewan, Canada. *Economic Geology* 109, 539-566.

Richard, A. (2009) Brine migration at the basement/sedimentary cover unconformity and formation of Proterozoic uranium mineralizations (Athabasca Basin, Canada). Unpublished Ph. D. thesis, Institut National Polytechnique de Lorraine, Nancy, France, 239 p.

Richard, A., Boiron, M.-C., Cathelineau, M., Derome, D., Pettke, T., Banks, D.A., Mercadier, J., & Cuney, M. (2008) U Concentrations in Ore Fluids: A LA-ICP-MS Investigation of Fluids Associated with Unconformity-Related Uranium Deposit. GAC-MAC congress, Québec, Canada, p 143.

Richard, A., Boulvais, P., Mercadier, J., Boiron, M.-C., Cathelineau, M., Cuney, M., & France-Lanord, C. (2013) From evaporated seawater to uranium-mineralizing brines: Isotopic and trace element study of quartz–dolomite veins in the Athabasca system. *Geochimica et Cosmochimica Acta* 113, 38–59.

Richard, A., Kendrick, M.A., & Cathelineau, M. (2014) Noble gases (Ar, Kr, Xe) and halogens (Cl, Br, I) in fluid inclusions from the Athabasca Basin (Canada): Implications for unconformity-related U deposits. *Precambrian Research* 247:110–125

Richard, A., Pettke, T., Cathelineau, M., Boiron, M.-C., Mercadier, J., Cuney, M., & Derome, D. (2010) Brine–rock interaction in the Athabasca basement (McArthur River U deposit, Canada): consequences for fluid chemistry and uranium uptake. *Terra Nova* 22, 303–308.

Richard, A., Rozsypal, C., Mercadier, J., Banks, D.A., Cuney, M., Boiron, M.-C., & Cathelineau, M. (2012) Giant uranium deposits formed from exceptionally uranium-rich acidic brines. *Nature Geoscience* 5, 142–146.

Roedder, E. (1984) Fluid Inclusions. Mineralogical Society of America, *Reviews in Mineralogy* 12, p 644.

Sadofsky, S.J., & Bebout, G.E. (2000) Ammonium partitioning and nitrogen-isotope fractionation among coexisting micas during high-temperature fluid-rock interactions; examples from the New England Appalachians. *Geochimica et Cosmochimica Acta* 64, 2835–2849.

Schwab, V., Spangenberg, J.E., & Grimalt, J.O. (2005) Chemical and carbon isotopic evolution of hydrocarbons during prograde metamorphism from 100 °C to 550 °C: Case study in the Liassic black shale formation of Central Swiss Alps. *Geochimica et Cosmochimica Acta* 69, 1825–1840.

Spence, H.S. (1920) Graphite. Canada Department of Mines, Mines Branch, Report No. 511.

Sterner, S.M., & Bodnar, R.J. (1989) Synthetic fluid inclusions VII. Re-equilibration of fluid inclusions in quartz during laboratory-simulated metamorphic burial and uplift. *Journal of Metamorphic Geology* 7, 243-260.

Sterner, S.M., Hall, D.L., & Bodnar, R.J. (1988) Synthetic fluid inclusions. V. Solubility relations in the system NaCl-KCl-H2O under vapor-saturated conditions. *Geochimica et Cosmochimica Acta* 52, 989-1005.

Thomas, D. (2002) Structural observations from selected drill core and outcrops along the Dufferin Fault (Southwest Athabasca and MacFarlane Projects): Unpublished internal Cameco report, p. 1-36.

Thomas, D., Matthews, R.B., & Sopuck, V. (2000) Athabasca Basin (Canada) unconformity-type uranium deposits: exploration model, current mine developments and exploration directions. *In* Geology and Ore Deposits 2000: The Great Basin and Beyond (Cluer, J.K., Price, J.G., Struhsacker, E.M., Hardyman, R.F., & Morris, C.L., eds.). Geological Society of Nevada, Symposium Proceedings, Reno, Nevada, May 15-18 2000, 1, 103-126.

Touret, J.L.R. (2001) Fluids in metamorphic rocks. *Lithos* 55, 1–25.

Tuinstra, F., & Koenig, J.L. (1970) Raman spectrum of graphite. *Journal of Chemical Physics* 53, 1126–1130.

Wallis, R.H. (1970) The geology of the Dufferin Lake Area (West Half) Saskatchewan. Department of Mineral Resources, Geological Sciences Branch, Precambrian Geology Division (Regina). Geological Report 132.

Wilson, N.S.F., Stasiuk, L.D., & Fowler, M.G. (2007) Origin of organic matter in the Proterozoic Athabasca Basin of Saskatchewan and Alberta, and significance to unconformity uranium deposits. *In* EXTECH IV: Geology and Uranium Exploration TECHnology of the Proterozoic Athabasca Basin, Saskatchewan and Alberta, (Jefferson, C.W., & Delaney, G., ed.). *Geological Survey of Canada*, Bulletin 588, 325-339.

Wopenka, B., & Pasteris, J.D. (1993) Structural characterization of kerogens to granulite-facies graphite: Applicability of Raman microprobe spectroscopy. *American Mineralogist* 78, 533–557.

Yeo, G.M., & Delaney, G. (2007) The Wollaston Supergroup, stratigraphy and metallogeny of a Paleoproterozoic Wilson cycle in the Trans-Hudson Orogen, Saskatchewan. *In* EXTECH IV: Geology and Uranium Exploration TECHnology of the Proterozoic Athabasca Basin, Saskatchewan and Alberta, (Jefferson, C.W., & Delaney, G., ed.). *Geological Survey of Canada, Bulletin* 588, 89-117.

Yeo, G.M., & Potter, E.G. (2010) Review of reducing mechanisms potentially involved in the formation of unconformity-type uranium deposits and their relevance to exploration. *In* Summary of Investigation 2010, Saskatchewan Geological Survey, Saskatchewan Ministry of Energy and Resources, Miscellaneous Report 4(2), 1-13.

Yui, T.-F., Huang, E., & Xu, J. (1996) Raman spectrum of carbonaceous material: a possible metamorphic grade indicator for low-grade metamorphic rocks. *Journal of Metamorphic Geology* 14, 115–12.

APPENDIX A
DRILL HOLE SW-20

Figure A-1. Drill hole SW-20 showing the transition of the variably graphitic pelitic schists (VGPS) to the red/green zone (RGZ) and the bleached zone (BZ), as we approach the unconformity (U/C)

APPENDIX B
DUFFERIN LAKE FIELD OBSERVATIONS REPORT

Introduction

The report provide my field observation notes from 12 days of logging, sampling and photographing drill core at Dufferin Lake, from July 8th to July 19th. I examined 7 drill holes from Cameco (DF-60, SW-10, SW-13, SW-17, SW-18, SW-19, SW-20; Figure 1) near a conductor in a mineralized zone and 1 drill hole (SW-42) in an unmineralized zone to compare the type of graphite. Samples have been analyzed to characterize the textural relationships, crystallinity, and type of CM/graphite.

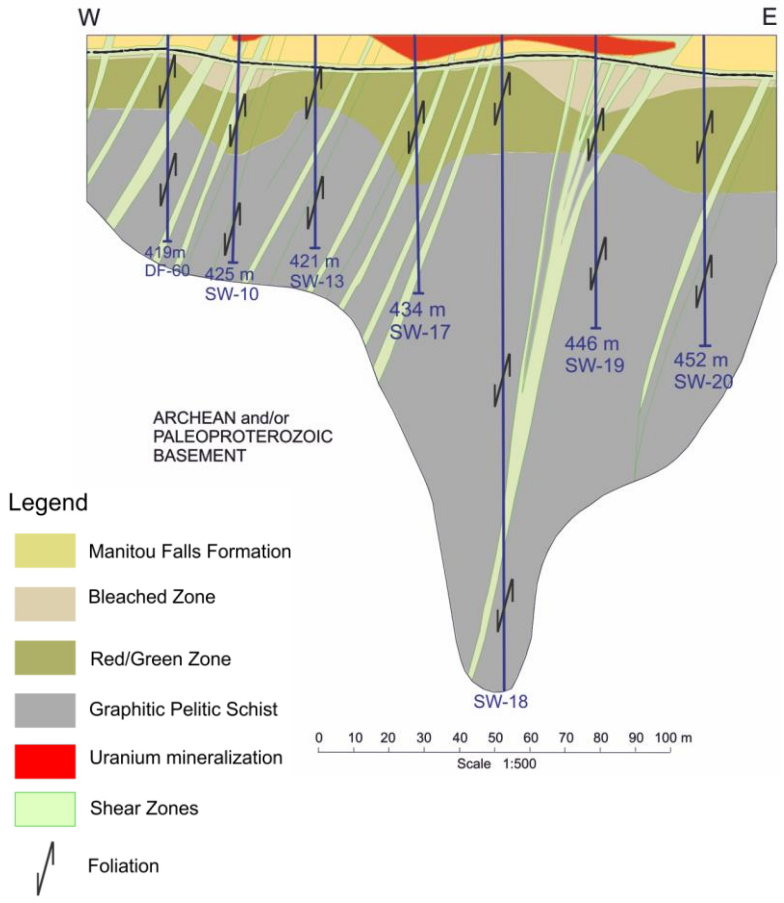

Figure B-1. Geological cross section from the Dufferin Lake Zone, illustrating the presence of graphite-depleted (Gr-poor-depleted) and graphite-rich (Gr-rich) zones

DDH DF-60

Core Logging

Log	Degree of graphite (/5)	Core axis	Samples (m)
364.4m: unconformity			
364.4m-365.5m: friable, rubble core, strongly bleached	0		
365.8m-367.4m: strongly bleached, friable, clay alteration	0		366.5
367.4m-382.1m: red/green zone, pelitic schist, foliated (5-30°), highly sheared, contorted, crenulated, rubble core, more hematite at the beginning then more chloritic, clay alteration, small quartz boudins, quartz veinlets	0-1	5-30	369.0 373.0 375.2 381.7
382.1m-419.0m: variably graphitic pelitic schist with local graphitic fault, foliated (5-20°), pyrite 383.2m-396m, 416.2m-419.0m Strongly graphitic fault at : 396.0m-416.2m: weakly graphitic pelitic schist, lots of pyrite, quartz boudins	3-4-5	5-20	387.0 390.7 399.2 414.1 417.9

Sampling

DDH	Depth (m)	Observations	Photos
DF-60	366.5	close to the unconformity, strongly bleached, brecciated, clay alteration, no graphite	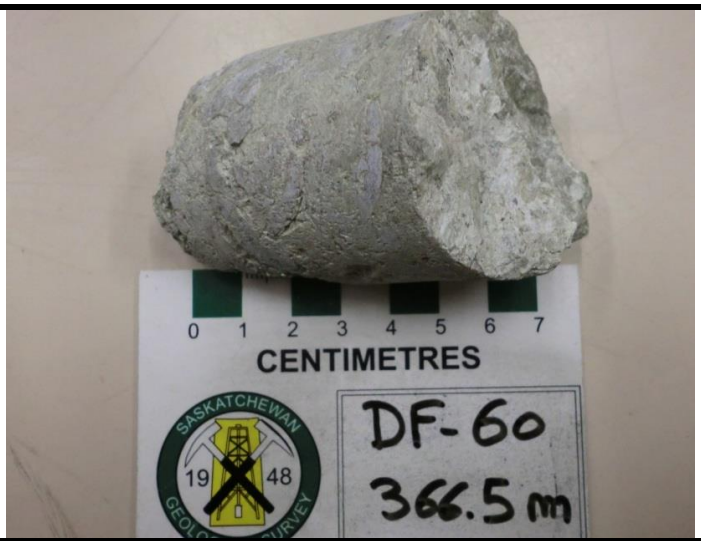

DF-60	369.0	foliated (40°), red/green foliation, quartz vein along the foliation, boudinage, altered garnets	
DF-60	373.0	foliated, more chloritic, quartz veinlets with hematite, hematite in fractures	
DF-60	375.2	chloritic pelitic schist, quartz veins crosscut the foliation (20°)	

DF-60	381.7	transition red-green zone to fresher rocks, chloritic	
DF-60	387.0	brecciated graphitic fault	
DF-60	390.7	50cm of fresh rock between brecciated graphitic fault, quartz veinlets crosscut the foliation	

DF-60	399.2	weakly graphitic pelitic schist, pyrite, foliated (5-10°), blue-grey quartz vein crosscut the foliation	
DF-60	414.1	quartz boudins, pyrite, the foliation (10°) is contorted, altered garnets	
DF-60	417.9	brecciated graphitic fault	

DDH SW-10

Core Logging

Log	Degree of graphite (/5)	Core axis	Samples (m)
364.3m-368.9m : Sandstone locally hematite, locally strongly desilicified, locally druzy quartz and brecciated, and vuggy quartz 362.2m-368.9m: polymectic conglomerates	0		364.4 367.6 365.2
368.9m: Unconformity	0		
368.9m-370.3: rubble core	0		
370.3m-377.6m: foliated argillaceous sericite-muscovite-rich phyllite, locally boudinage, banded, layered, weakly hematite along layers, progressively more hematite and chlorite,	1	Variable 15/20°	372.5
377.6m-394.7m: moderately to strongly hematite and chlorite locally fractures controlled, parallel to the fabric, chlorite fractures postdate the foliation parallel to chlorite and hematite	1	0- 10/20°	377.9 381.0 385.1 385.6 389.5 392.5 393.5
394.7m-398.2m: Foliated weakly banded pelitic schist with quartz vein (397m-398m), horizontal fractures locally graphite (1/2cm wide)	2	10/20	396.5 397.4
398.2m-404m: weakly graphitic pelitic schist, layered, fractures, sulfides along fractures, fractures along foliation with quartz and/or carbonates, horizontal fractures, Graphite layer-controlled	2	0/10	399.5 401.0 403.9
404m-425m: Moderately to strongly graphitic pelitic schist, foliated and contorted Graphite along the fracture, along the foliation 410.6m: fracture with sulfide 411.2m: fracture with sulfide	3-4	0-20	404.7 414.7

Sampling

DDH	Depth (m)	Observation	Photos
SW-10	364.4	sandstone, CM?	
SW-10	367.6	sandstone, CM?	
SW-10	365.2	quartz veinlet/vug greenish-grey chloritization?	

SW-10	372.5	characteristic of the interval, the foliation is weakly contorted, hematite veinlets along the foliation. Foliation: 10°	
SW-10	377.9	red/green bands, small fractures, quartz veins, no graphite, foliation: 40°	
SW-10	381.0	chlorite/K-feldspar-apatite breccia?, chlorite/carbonate /hematite fracture	

SW-10	385.1	In the red green zone, foliated (30°), no banded, no brecciated compared to the last one and the next one	
SW-10	385.6	chlorite/hematite bands, brecciated, fractures	
SW-10	389.5	brecciated, chlorite and hematite, hematite seems to replace some minerals	

SW-10	392.5	brecciated red/green zone	
SW-10	393.5	strongly hematitic, chlorite stain	
SW-10	396.5	less hematite, only few stains, banded, weakly more graphitic (?), foliated (10°)	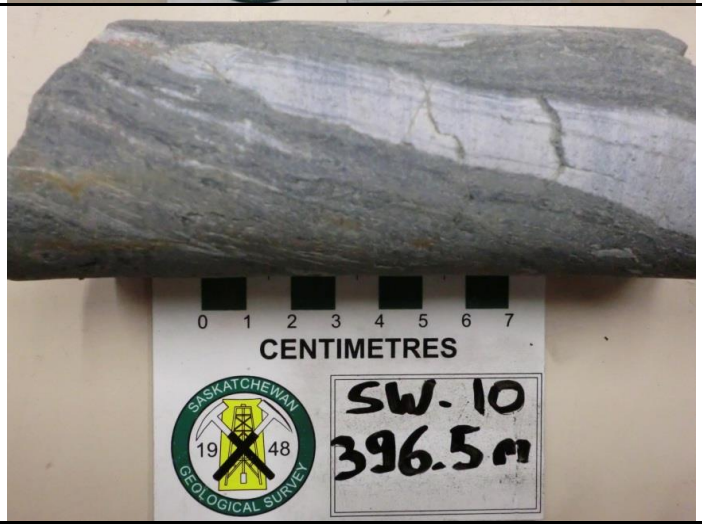

SW-10	397.4	quartz vein with hematite veinlets and fractures	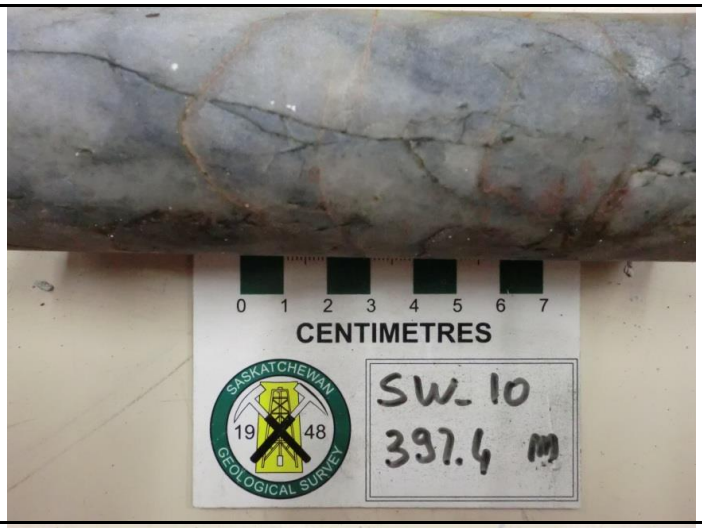
SW-10	399.5	foliated (20°), contorted pelitic schist, similar to the interval SW-17-392.2 (387m-396m), weakly graphitic	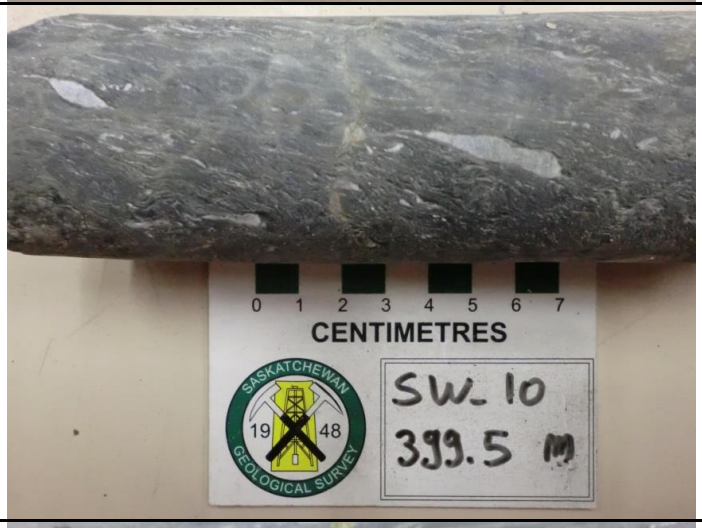
SW-10	401.0	weakly graphitic pelitic schist, sulfides disseminated or veinlets, foliation (20°), sulfide fractures crosscut the foliation	

SW-10	403.9	quartz vein crosscut the foliation (0/5°), more graphitic layers	
SW-10	404.7	brecciated, some ductile deformation, some graphite along the foliation/fractures	
SW-10	414.7	Strongly graphitic foliated (0°) pelitic schist, graphite along the foliation, sulfides, sample representative of the last unit	

DDH SW-13

Core Logging

Log	Degree of graphite (/5)	Core axis	Samples (m)
368.5m: unconformity			
368.5m-369.5m: rubble core so maybe fault (?), clays alteration, the ten first centimeters are foliated with red/green bands and the foliation is contorted.			
369.6m-371.8m: Foliated, bedded phyllitic pelitic schist. The foliation is a little contorted	0-1	10	369.6
371.8m-376.5m: foliated pelitic schist. Boudinage along the foliation (Feldspar?), hematite veinlets along the foliation, veinlets crosscut the foliation, quartz veins, presence of sulfide and maybe cobalt 375.8m-376.5m: rubble core, sulfides stain, hematite veins crosscut the foliation, foliation contorted	1-2	10,20, 70	373.1 373.4 376.0
376.5m-382.9m: Foliated pelitic schist. Foliation little contorted, quartz/carbonates veinlets and sulfide veinlets crosscut the foliation	1	10/40	377.7
382.9m-421.0m: Foliated pelitic schist. Altered garnet layers along the foliation which becomes washed deeper, the foliation is contorted and become closer to core axis at depth, boudins along the foliation, locally big quartz band. 407m-409.5m: rubble core: fault (?) more graphitic	2-3 (in fault)	0/40	385.6 394.8 402.9 408.8

Sampling

DDH	Depth (m)	Observations	Photos
SW-13	369.6	representative of the phylitic pelitic schist without graphite, the foliation is contorted	

SW-13	373.1	sulfides disseminated, hematite vein, weakly to moderately graphitic	
SW-13	373.4	boudinage (feldspar), lineation, foliation (10°), hematite vein	
SW-13	376.0	sulfides, maybe cobalt, hematite vein, graphitic	

			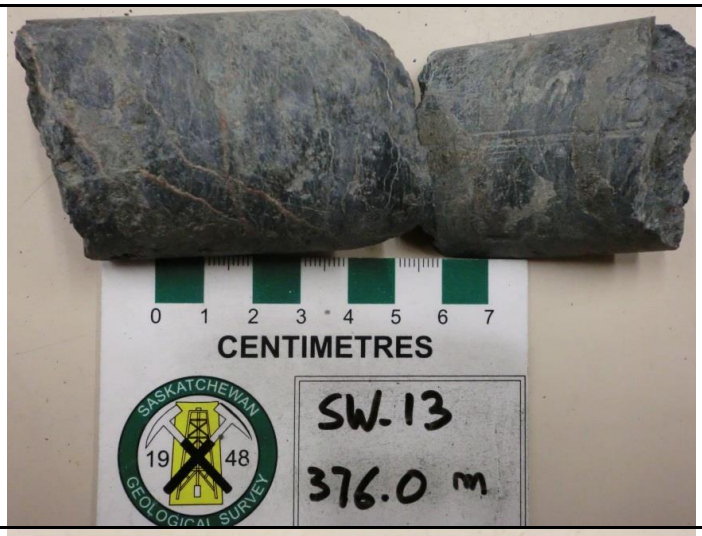
SW-13	377.7	foliation (20°), boudinage, fresh rock, weakly graphitic, representative of the interval 376.5m-382.9m	
SW-13	385.6	foliated (30°), altered garnet layer	

SW-13	394.8	brecciated, foliated (40°), some graphite along the foliation,	
SW-13	402.9	foliated (40°), fresh pelitic schist, representative of the interval 382.9m-421m	
SW-13	408.8	graphitic fault	

DDH SW-17

Core Logging

Log	Degree of graphite (/5)	Core axis	Samples (m)
sandstone			364.9 369.9
370.2m: Unconformity			
370.2m-371.1m: foliated pelitic schist, clay alteration, strongly hematitic, friable		60/70	370.7
371.1m-374.9m: foliated pelitic schist , clay alteration, hematite veins along the foliation, red/green bands, quartz vein, foliation is weakly contorted, locally quartz band along the foliation, friable	0/1	15	374.2
374.9m-387.1m: foliated pelitic schist, banded, locally fractured, boudinage, hematite veins along or crosscut the foliation, locally rubble core so maybe some fault (?), the foliation is locally contorted, quartz bands, quartz veinlets, lot of altered garnet. Graphite along the foliation and fractures	1/2	10-30	377.2 380.0 383.0 383.9
387.1m-396.5m: foliated graphitic pelitic schist. The foliation is locally contorted, locally brecciated, hematite veinlets along or crosscut the foliation, graphite along the foliation , quartz boudins along the foliation 391-396.5: Highly sheared zone	2/3	30	388.2 391.0 392.9 395.8
396.5m-410m: foliated pelitic schist. Locally rubble core so maybe fault (?), banded, locally hematite bands, locally garnet 404.5m-407m: weakly sheared	2/3	0-20	404.1 406.7
410m-416m: Graphitic pelitic schist. foliated, locally brecciated, the foliation is crenulated, sulfides along and crosscut the foliation	2/3		412.4
416m-421m: pelitic schist. graphite along the fractures, sulfides locally quartz band, boudins along foliation, the foliation is contorted and locally microfolded	2/3	5-40	
421m-430.4m: strongly graphitic pelitic schist. the foliation is contorted and locally microfolded, locally quartz band, graphite is along the fractures, sulfides crosscut the foliation, highly sheared	3/4	10-20-45	423.0
430.4m-434m: graphitic schist. graphite along the foliation, disseminated sulfides, the foliation is contorted	2/3	10-20	433.2

Sampling

DDH	Depth (m)	Observations	Photos
SW-17	364.9	sandstone, radioactivity, cm?	
SW-17	369.9	sandstone, radioactivity, cm?	
SW-17	370.7	close to the U/C, highly clay altered, green/red banded, phyllitic, no graphite	

SW-17	374.2	close to the U/C, no graphite, foliated (30°), clay alteration	
SW-17	377.2	hematite veins, sheared and then brecciated, foliated (25°)	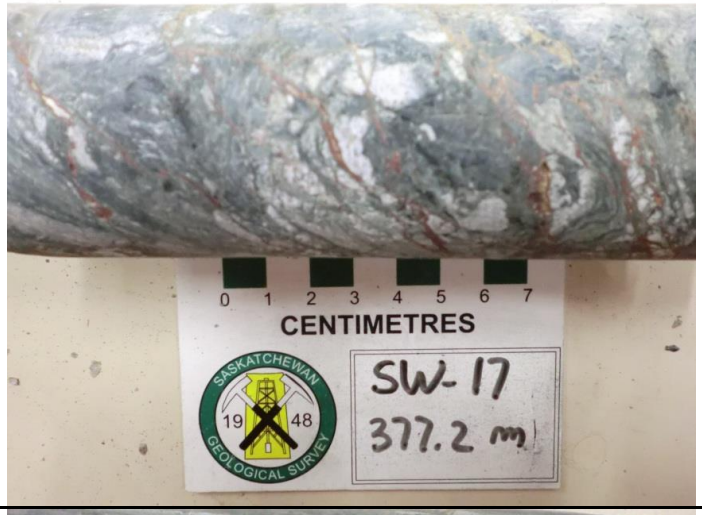
SW-17	380.0	garnet-graphite-phyllite (?) pelitic schist crosscut by hematite, chlorite vein, grey-black band	

SW-17	383.0	altered garnet layers, foliation (30°), quartz vein, contact altered garnet layers then no garnet, quartz band	
SW-17	383.9	vein, foliation (30°), weakly sheared	
SW-17	388.2	chlorite-quartz-carbonate vein	

SW-17	391.0	carbonate vein	
SW-17	392.9	representative of the shear zone	
SW-17	395.8	highly sheared graphitic pelitic schist	

SW-17	404.1	hematite band, grey-black band, foliated (20/30°)	
SW-17	406.7	brecciated vein, sulfides, hematite vein	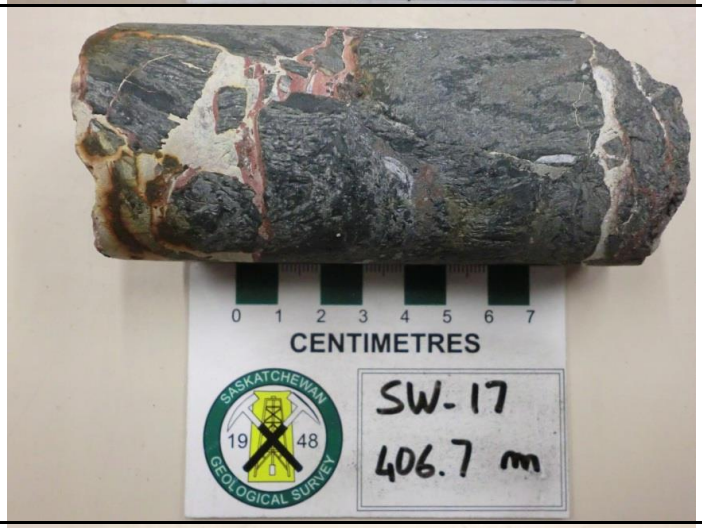
SW-17	412.4	strongly sheared, sulfides fracture crosscut	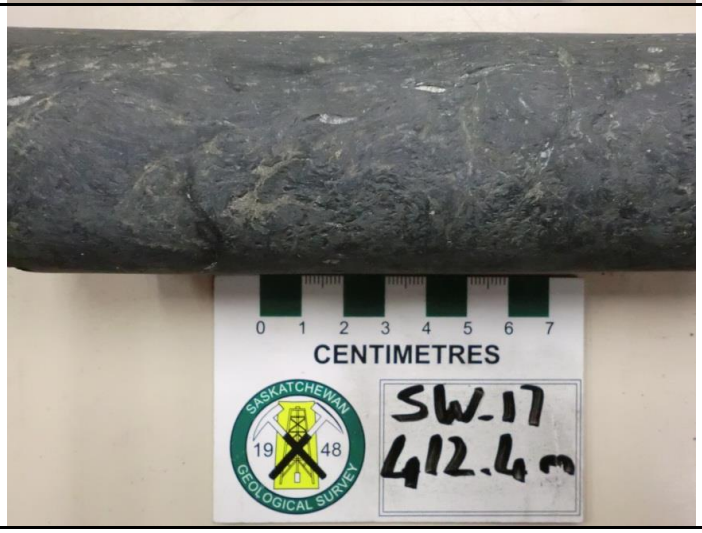

SW-17	423.0	strongly sheared and strongly graphitic, sulfides	
SW-17	433.2	not so sheared, seems to be less graphitic, foliated (25°)	

DDH SW-18

Core Logging

Log	Degree of graphite (/5)	Core axis	Samples (m)
368.6m: unconformity sharp			
368.6m-369.7m: phyllitic, friable for the first 50cm become progressively greenish and pinkish		45, 60	368.8
369.7m-395.1m: red/green zone 369.7m-374.1m: more green than red, locally rubble core, foliated (50°), chlorite altered garnet *al*ong bedding, locally quartz boudins, locally clay altered, quartz vein along the foliation, hematite veinlets or stain.	0-1	10, 45, 50,60	369.9 373.3 379.0 376.5 382.5 386.2 387.5

374.1m-392.9m: more hematitic, strongly altered garnet, hematite bands or stain, foliated (10/45°), contorted and microfolded, more quartz boudins to the end and more sheared 385.8m-388m: more green-black zone 392.9m-395.1m: more green-black zone and become progressively less chloritic to fresh basement rocks			388.0 388.8 390.9
395.1m-611m: variably graphitic pelitic schist, variably sheared and variable foliation. Strongly graphitic fault (4): 410.7m-411m, 583.0m-583.3m, 590.9m-592.7m, 596.1m, 604.3m-604.9m. 395.1m-398m: weakly graphitic (2) along the foliation (20°), the foliation is contorted 398.0m-406.7m: strongly graphitic (3), locally garn*et al*tered, graphite along the foliation or along fractures, the foliation os contorted, more quartz boudins at the end. 406.7m-410m: weakly graphitic (2), no shear zone, foliated (10-20°), locally garnet 410.0m-422.2m: moderately graphitic (3), foliated (5-20°), contorted, locally highly sheared, graphite along the foliation, locally garnet, locally quartz boudin layers, sulfides along the foliation. 422.2m-433.3m: strongly graphitic (3-4), locally altered garnet, foliated (20-40°), contorted, some sulfides, 433.3m-467.5m: moderately graphitic, foliated (5-30°), contorted 434.0m-436.6m: highly sheared, quartz boudins, graphite along the foliation/fractures 467.5m—595.3m: moderately to strongly graphitic (3-4), locally garnet, sulfides, variably sheared, locally weakly graphitic (531.8-532.80) 472.5m-504.8m: more sheared zone with quartz boudins 595.3m-611m: weakly graphitic	2 3 2 3 3-4 3-4	5, 10, 20, 30, 40	396.0 401.0 409.4 416.1 425.9 434.3 456.0 469.8 481.4 504.6 512.3 514.5 543.0 547.2 562.3 564.8 568.5 591.6 599.6

Sampling

DDH	Depth (m)	Observations	Photos
SW-18	368.8	unconformity, friable, foliated	
SW-18	369.9	close to the unconformity, foliated, contorted, pinkish/grey bands, altered garnet, no graphite	
SW-18	373.3	characteristic of the more green zone, altered garnet, foliated (30°), hematite stain, grey-blue quartz	

SW-18	376.5	transition green/red zone, banded, foliated, contorted, altered garnet	
SW-18	379.0	characteristic of more red zone, strongly garnetiferous, chlorite stain	
SW-18	380.6	next chlorite zone with sphalerite and hematite veins, foliated (30°)	

SW-18	382.5	druzy quartz with pink ? Feldspar/apatite	
SW-18	387.5	specular hematite (?)/sphalerite(?) in vein crosscuted by pink apatite/K-feldspar (?). Note subvertical fracture just up from sub horizontal fracture	
SW-18	388.8	clot of black chlorite in a shear red/green phyllitic rock, crosscut by lots of hematite vein (?)	

SW-18	390.9	green/red bands, foliation (30°)	
SW-18	396.0	weakly graphitic pelitic schist, altered garnet, foliated (10°), contorted, hematite stain	
SW18	398.0	sphalerite vein (50°) crosscut the foliation, chlorite/hematite bands, quartz boudins, altered garnet	

SW-18	401.0	strongly graphitic pelitic schist, foliated (30°) sulfides along the foliation, quartz/carbonates veinlets along the foliation	
SW-18	409.4	weakly graphitic pelitic schist, foliated (20°)	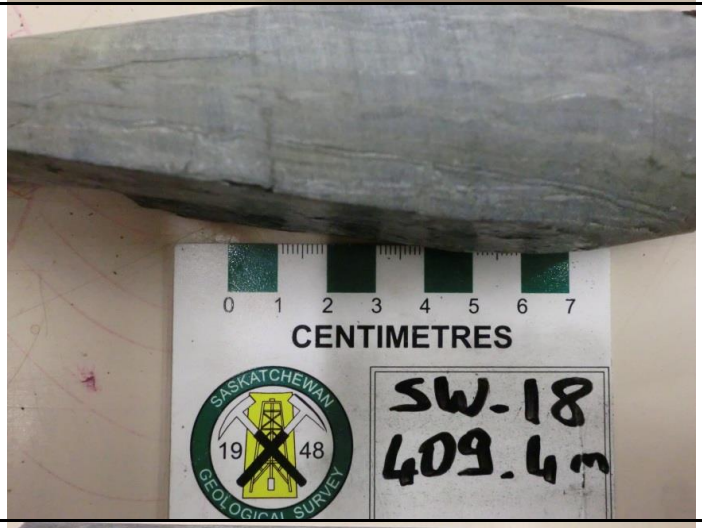
SW-18	416.1	moderately graphitic pelitic schist characteristic, graphite along the foliation (5-10°), contorted, sulfides, local garnets	

SW-18	425.9	strongly graphitic pelitic schist, strongly sheared, sulfides in veinlets crosscut the foliation and sulfide disseminated, the foliation is contorted	
SW-18	434.3	moderately graphitic pelitic schist, highly sheared with quartz boudins, sulfides	
SW-18	456.0	representative of the interval, more layered, less sheared, rock, local garnets, moderately graphitic, sulfides, quartz boudins	

SW-18	469.8	graphitic fault	
SW-18	481.4	representative of a small zone, quartz boudins, sulfides, altered garnet	
SW-18	504.6	moderately graphitic, lot of sulfides, quartz boudins, altered garnet	

SW-18	512.3	strongly graphitic fault, with vertical extension within extensional fracture green-chlorite/ euhedral quartz/ pyrite	
SW-18	514.5	euhedral quartz in extensional fracture contains green chlorite and sulfides	
SW-18	543.0	nice carbonate fracture	

SW-18	547.2	moderately graphitic, clots of pyrite in fracture zones, quartz veins, foliation (5°)	
SW-18	562.3	chlorite veinlets with pyrite veinlets, chlorite in pyrite vein, relationship between chlorite/pyrite/quartz	
SW-18	564.8	carbonates-quartz-sulfides fracture	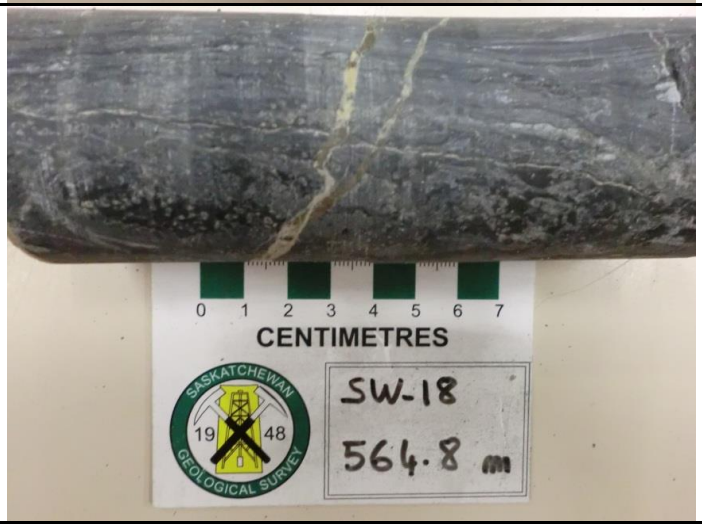

SW-18	591.6	graphitic fault	
SW-18	599.6	weakly graphitic pelitic schist, characteristic of the last unit, sulfides veinlets and disseminated, quartz boudins	

DDH SW-19

Core Logging

Log	Degree of graphite (/5)	Core axis	Samples (m)
369.7m: unconformity			369.5
367.9m-372.0m: phyllitic, strongly bleached, clay alteration, foliated (50°), contorted, crenulated	0	50	
372.0m-384.3m: foliated (15-30°), weakly bleached, local rubble core, local breccia, increase of hematite content to the end of the unit, greenish bands, strongly sheared	0	15-30	376.2 382.5 384.2
384.3m-395.0m: red/green zone, become progressively fresh basement rock, foliated (10-30-40°), locally	0-1	10, 30, 40	389.7 394.9

banded pelitic schist, locally rubble core, hematite veinlets, hematite stain, altered garnets, shear zone			
395.0m-446m: foliated variably graphitic schist, locally rubble core, locally strongly pyritic, locally altered garnet, locally highly sheared	2-3	5, 10, 30, 45	398.0 413.2 435.5 444.8

Sampling

DDH	Depth (m)	Observations	Photos
SW-19	369.5	representative of the unit, phyllitic, strongly bleached, clay alteration, foliated (50°), contorted, crenulated	
SW-19	376.2	representative of the unit, strongly sheared, green/red shear bands, clay alteration, foliated (20°), no graphite	

SW-19	382.5	more hematitic, strongly sheared, greenish band	
SW-19	384.2	brecciated with hematite veins and veinlets, friable, clay alteration	
SW-19	389.7	representative of the unit, foliated (30°), hematite band, hematite veinlets which crosscut or along the foliation/fractures, altered garnet	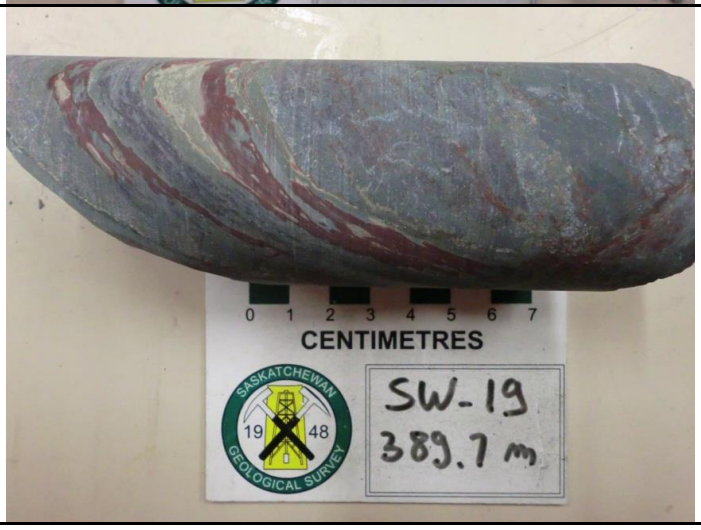

SW-19	394.9	fresher rock, foliated (20°), altered garnets, weakly sheared, carbonate vein crosscut	
SW-19	398.0	strongly graphitic, sulfides veinlets, altered garnets along the foliation, carbonate vein crosscut the foliation, the foliation (10°) is weakly contorted	
SW-19	413.2	more sheared, the foliation is contorted, altered garnets, sulfides along the foliation (20-30°), quartz boudins, weakly graphitic	

SW-19	435.5	foliated (20-30°), sulfides along the foliation or disseminated	
SW-19	444.8	representatives of a zone, garn*et al*tered, sulfides, foliated (10-20°), contorted, quartz boudins	

DDH SW-20

Core Logging

Log	Degree of graphite (/5)	Core axis	Samples (m)
sandstone, medium grain size, brecciated, some fractures, weakly pinkish, clay alteration			327.0 341.3 361.0 364.4 366.0
374.4m-374.7: unconformity, sharp contact, friable			
374.7m-375.7m: bleached zone, the foliation is contorted			375.3
375.7m-378.6m: green color, hematite stain, foliated (30°), locally clay alteration, hematite veinlets, altered garnets	0-1	30	376.6

378.6m-406.2m: red/green zone, hematite is dominant throughout the interval, foliated (10-40°), variably sheared, quartz boudins, clay alteration, local rubble core		10-40	381.6 384.8 397.5 406.2
406.2m-452.0m: variably graphitic pelitic schist, foliated (5-10°), altered garnets, the foliation is locally contorted , local rubble core with graphite, locally boudinage mostly at the beginning of this interval, locally folded, locally strongly graphitic in rubble core: 413.9m, 423.4m, 426.7m-421.1m	2-3-4	5,10, 25	407.0 410.6 413.9 415.0 418.4 423.6 427.5 437.3 441.3 443.2 447.0 450.5

Sampling

DDH	Depth (m)	Observations	Photos
SW-20	327.0	sandstone	

SW-20	341.3	sandstone	
SW-20	361.0	sandstone, subvertical fracture with sphalerite/hematite crystals	
SW-20	364.4	sandstone, green chlorite crystal?, partly kaolinitized	

SW-20	366.0	sandstone, chlorite/hematite overprint by late kaolinite and Fe-oxides	
SW-20	375.3	representative sample of the bleached zone, altered garnets	
SW-20	376.6	representative sample black-green/greenish color, hematite vein and hematite stain, clay alteration	

SW-20	381.6	quartz segregation, hematite, carbonates veinlets, chlorite stain	
SW-20	384.8	representative sample, hematite and chlorite, quartz vein, foliated (20-30°)	
SW-20	397.5	more chloritic with hematite vein and stain, quartz boudins	

SW-20	406.2	transition to fresher rocks, the foliation seems to be 10-20°, sheared, quartz with hematite vein	
SW-20	407.0	moderately graphitic pelitic schist, foliated (5°)local clay alteration	
SW-20	410.6	weakly graphitic, quartz boudins, foliated (10°), clay alteration, quartz veinlets	

SW-20	413.9	strongly graphitic fault	
SW-20	415.0	moderately graphitic pelitic schist, the foliation is hardly contorted, sulfides disseminated and in veinlets	
SW-20	418.4	moderately to strongly graphitic, quartz boudins, altered garnet, foliated (30°)	

SW-20	423.6	foliated (10°) contorted, graphitic pelitic schist, quartz boudins, pyrite veinlets and clots of pyrite	
SW-20	427.5	moderately graphitic, altered garnet, quartz boudins, foliated (5°)	
SW-20	437.3	foliated (40°), microfolded, altered garnet, carbonates veinlets, weakly graphitic, chalcopyrite (?)	

SW-20	441.3	lots of pyrite, band of altered (sulfides?) garnets along a vein, weakly graphitic, quartz veinlets, sulfides veinlets	
SW-20	443.2	foliated (5-10°), contorted, quartz boudins, altered garnets, moderately graphitic, sulfides	
SW-20	447.0	clots of pyrite, sulfides veinlets, weakly graphitic	

SW-20	450.5	foliated (20-30°), altered garnets, sulfides, boudinage	

DDH SW-42

Core Logging

Log	Degree of graphite (/5)	Core axis	Samples (m)
439.0m: unconformity			
439.0m-444.0m: strongly bleached, mostly toward the unconformity, become progressively pinkish, clay alteration			442.8
444.0m-474.9m: red/green zone, clay alteration and bleached at the beginning of the interval, foliated, hematite is dominant in the interval, patchy green stain along the fractures	0-1		447.4 458.6 461.2 461.9 472.9
474.9m-519.7m: moderately to strongly graphitic pelitic schist, local rubble core, foliated (20-45°), the rocks are sandy compare to SW-10-13-17-18-19-20, muddy part in the sandy rocks (brittle-ductile deformation), local pyrite, veinlets	3-4-5	20-45	479.4 481.4 484.0 487.6 495.7 506.0 514.0 519.0

Sampling

DDH	Depth (m)	Observations	Photos
SW-42	442.8	representative sample of this area, strongly bleached, clay alteration, consolidated	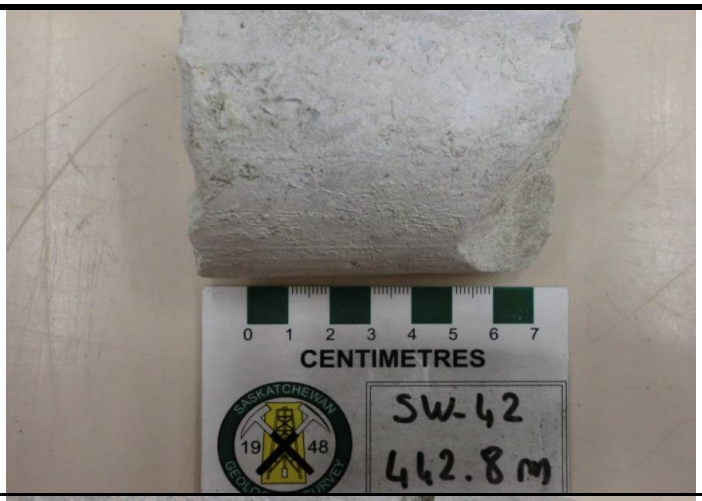
SW-42	447.4	red/green zone, clay alteration, chlorite/hematite, foliated(30°), fractures crosscut, vein quartz, hematite vein	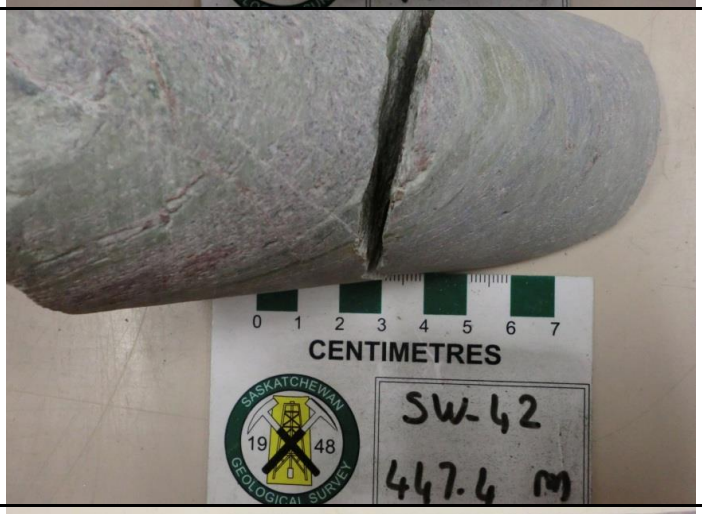
SW-42	458.6	green/red zone, foliated (30°),hematite veinlets crosscut the foliation, hematite stain crosscut by veinlets	

SW-42	461.2	sandy hematitic pelitic schist, foliated (40°), quartz veinlets	
SW-42	461.9	relationship between vein quartz/chlorite/hematite	
SW-42	472.9	more chloritic, quartz boudins along the foliation, veinlets of quartz/hematite, fractures, clay alteration	

SW-42	479.4	strongly graphitic pelitic schist, foliated (30°), pyrite disseminated	
SW-42	484.0	strongly graphitic pelitic schist, quartz boudins rotated, sulfides along fractures, quartz veinlets	
SW-42	487.6	sandy and locally muddy part, quartz veinlets crosscut by a fracture, sulfides, strongly graphitic	

SW-42	495.7	foliated (40°) pelitic schist, sandy and muddy part, pyrite along the foliation, strongly graphitic, quartz boudinage	
SW-42	506.0	representative sample, fresh, foliated (10°), moderately graphitic	
SW-42	514.0	strongly graphitic (fault?)	

SW-42	519.0	strongly graphitic, brecciated (?), clot of pyrite, blue-grey quartz	

APPENDIX C
PETROGRAPHIC OBSERVATIONS

Table C-1. Petrographic observations

		Deformation			Selected minerals									Quartz generations					Porph	Geochemistry				
Sample	Zone	Brittle	Brittle/ Ductile	Ductile	C species	Py 1	Py 2	Hem 1	Hem 2	Chl 1	Chl 2	Clay	Drv	Q1	Q2a	Q2b	Q3	Q4	(St, Gt. And)	C %wt	S %wt	B ppm	U ppm	SiO2 %wt
DF60-384.2	VGPS	x	x		x	x	x			x		x				x			x	4.84	0.43	344	37	59.5
DF60-403.8	VGPS		x	x	x	x	x			x		x				x			x	0.83	1.66	228	17	51.2
SW10-377.9	RGZ	x	x	x				x	x	x	x	x								0.62	0.01	2130	24	34.3
SW10-389.5	RZ	x	x	x				x	x	x		x			x	x			x	0.29	0.01	35	15	67.1
SW10-392.5	RGZ	x	x						x	x		x			x	x		x		0.61	0.01	55	11	54.0
SW10-396.5	GZ		x	x					x	x	x	x		x	x	x				0.24	0.03	36	2	65.9
SW10-404.7	GZ		x	x		x	x			x		x	x	x	x	x			x	1.4	2.29	654	7	53.9
SW13-373.1	GZ	x	x	x		x			x	x	x									0.91	10.79	48	37	20.0
SW17-375	GZ		x	x						x					x	x				0.27	0.01	206	5	60.8
SW17-383.0	GZ	x	x	x	x (?)		x	x		x		x			x	x			x	0.31	0.07	53	8	54.7
SW17-385.1	GZ		x	x	x		x			x					x	x			x	0.34	0.01	211	5	56.2
SW17-395.0	GZ	x	x	x	x			x		x		x		x	x	x	?			0.56	0.01	185	14	55.1
SW17-395.8	GZ	x	x	x	x		x	x		x					x	x			x	0.98	0.01	201	3	64.4
SW17-412.4	VGPS	x	x	x	x	x	x			x					x	x			x	5.37	8.84	120	6	37.5
SW17-415.1	VGPS		x	x	x	x	x			x					x				x	3.08	5.25	215	7	56.3
SW17-423	VGPS		x	x	x	x	x			x		x			x	x			x	4.18	6.13	166	<2	50.7
SW17-425.1	VGPS	x	x	x	x		x					x							x	4.64	5.16	209	9	45.9
SW17-433.9	VGPS		x	x	x	x				x						x			x	0.48	0.54	236	2	67.6
SW18-369.9	BZ									x		x	x		x	x				0.56	0.01	13100	65	52
SW18-380.6	RGZ		x	x				x	x	x		x			?		?		x	0.65	0.01	148	5	45.7
SW18-382.5	RGZ	x	x	x		x		x	x				x	x	x		x	x		0.5	0.01	142	12	59.5
SW18-398	RGZ	x	x	x				x		x		x							x	1.99	0.01	35	12	43

Sample	Zone	Deformation			Selected minerals									Quartz generations					Porph	Geochemistry				
		Brittle	Brittle/ Ductile	Ductile	C species	Py 1	Py 2	Hem 1	Hem 2	Chl 1	Chl 2	Clay	Drv	Q1	Q2a	Q2b	Q3	Q4	(St, Gt, And)	C %wt	S %wt	B ppm	U ppm	SiO2 %wt
SW18-409.1	GZ	x	x	x	x	x	x			x						x				0.53	0.59	143	<2	66.4
SW18-415.0	VGPS		x	x	x	x	x			x					x	x				1.43	0.99	88	3	58.9
SW18-416.1	VGPS		x	x	x	x	x			x			?		x	x			x	1.21	1.42	216	<2	58.5
SW18-425.0	VGPS	x	x		x	x	x			x					x	x			x	4.14	3.59	32	9	58.3
SW18-469.8	VGPS	x	x	x	x					x					x	x				0.74	0.53	51	6	60.5
SW18-475	VGPS		x	x	x					x					x	x			x	2.92	3.71	562	7	49.7
SW18-495	VGPS		x	x	x					x					x	x			x	1.12	1.70	190	6	59.6
SW18-515.0	VGPS	x	x	x	x					x					x	x			x	0.70	0.90	140	4	70.3
SW18-535.1	VGPS	x	x	x	x															1.54	2.12	205	5	56.9
SW18-565.1	VGPS			x	x										x	x			x	1.70	0.79	175	4	59.9
SW18-595.1	VGPS	x	x	x	x					x				?	x	x				0.52	0.86	39	4	57.0
SW19-369.5	BZ											x	x							0.84	0.01	12200	187	43.7
SW19-376.2	RGZ?		x	x	?			x		x		x			x	x				0.25	0.01	5.23	9	65.8
SW19-384.2	GZ				x				x	x					x	x			x	1.96	0.01	302	5	57.9
SW19-398.0	VGPS		x	x	x		x			x					x	x			x	1.24	0.88	275	<2	58.5
SW19-413.2	VGPS		x	x	x	x	x			x			x	x	x	x			x	1.18	2.35	207	<2	50.8
SW20-381.6	RZ		x						x						x			x		0.59	0.01	119	11	65.1
SW20-397.5	RGZ	x	x	x				x	x	x	x	x	x		?	?				0.08	0.01	642	<2	55.7
SW20-406.2	GZ			x						x					x	x				0.14	0.01	304	<2	62.2
SW20-410.6	GZ		x	x	?					x					x	x				0.17	0.01	359	<2	61.9
SW42-458.6	RGZ	x	x	x				x		x		x			x	x				0.12	0.01	221	<2	71.8
SW42-484.0	VGPS		x			x	x							x	x					1.13	0.17	177	<2	66.9

Porph: porphyroblast, C: carbon, Py: pyrite, Hem: hematite, Chl: chlorite, Drv: dravite, St: staurolite, Gt: Garnet, And: andalusite, VGPS: variably graphitic pelitic schist, RGZ: red/green zone, RZ: red zone, GZ: green zone, BZ: bleached zone

APPENDIX D
BACKSCATTER ELECTRON IMAGES

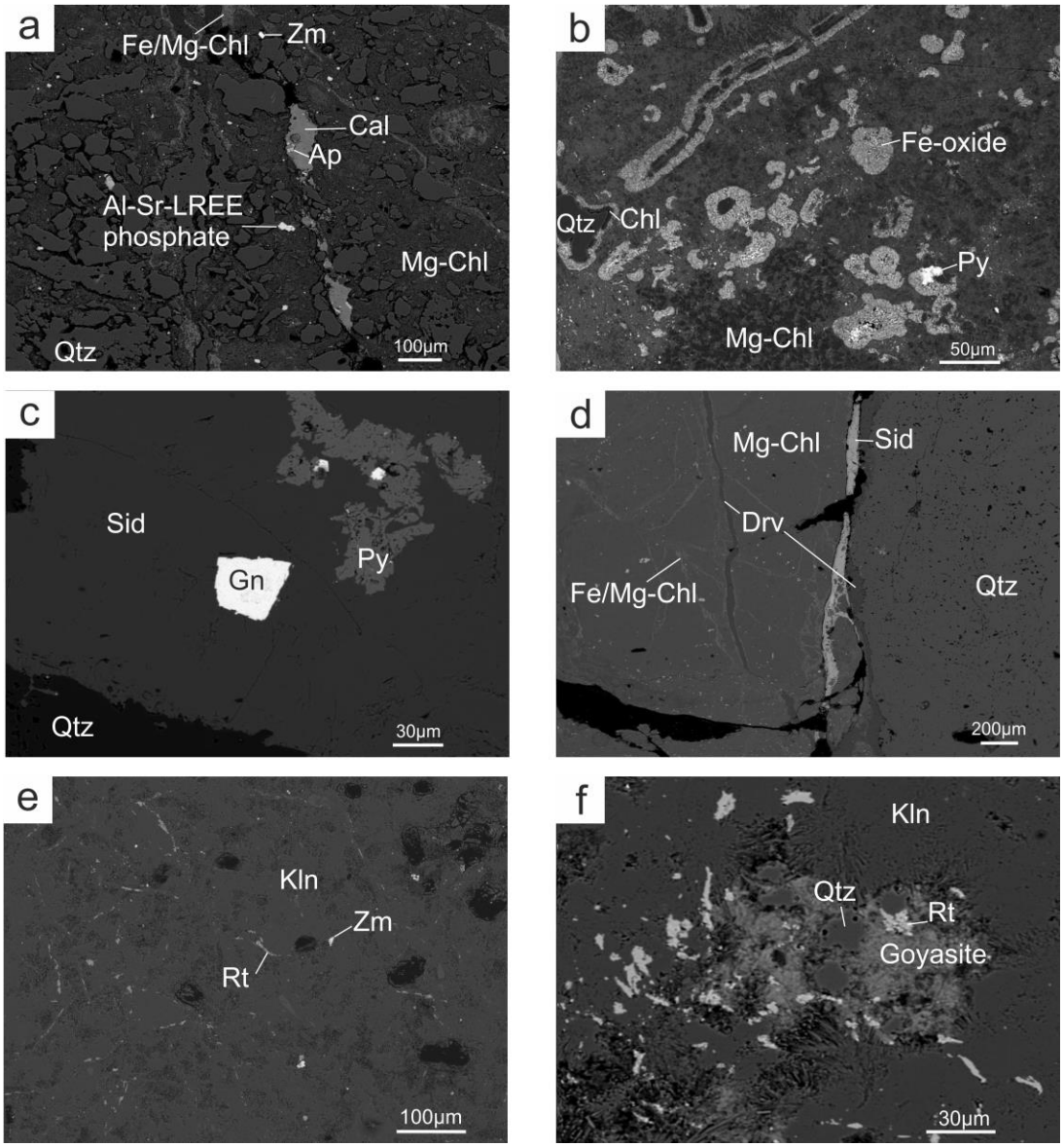

Figure D-1. Backscatter electron images of mineral assemblages observed in the bleached zone, the RGZ and a graphitic pelitic schist. (a) Mixture of Mg-chlorite and Fe/Mg-chlorite with quartz, zircon, Al-Sr-LREE phosphate (APS), and calcite (Cal) with apatite in the RGZ of the sample SW18-382.5. (b) Presence of Fe-oxides surrounding quartz and chlorite, with sometimes pyrite in the Mg-rich chlorite matrix of the RGZ of the sample SW18-382.5. (c) Siderite (Sid) vein with galena (Gn) and pyrite, surrounded by quartz in the RGZ of sample SW18-382.5. (d) Mixture of Mg-rich chlorite (Mg-Chl) and Fe/Mg-rich chlorite dominated by Fe (Fe/Mg-Chl), and quartz alteration matrix in the RGZ of the sample SW18-382.5. The matrix is crosscut by dravite and siderite. (e) Kaolinite-rich (Kln) alteration matrix representative of the bleached zone with the presence of zircon and rutile, of the sample SW18-369.9. (f) Kaolinite-rich alteration matrix with the presence of goyasite, rutile and quartz in the bleached zone of the sample SW18-369.9

APPENDIX E
RAMAN SPECTRA

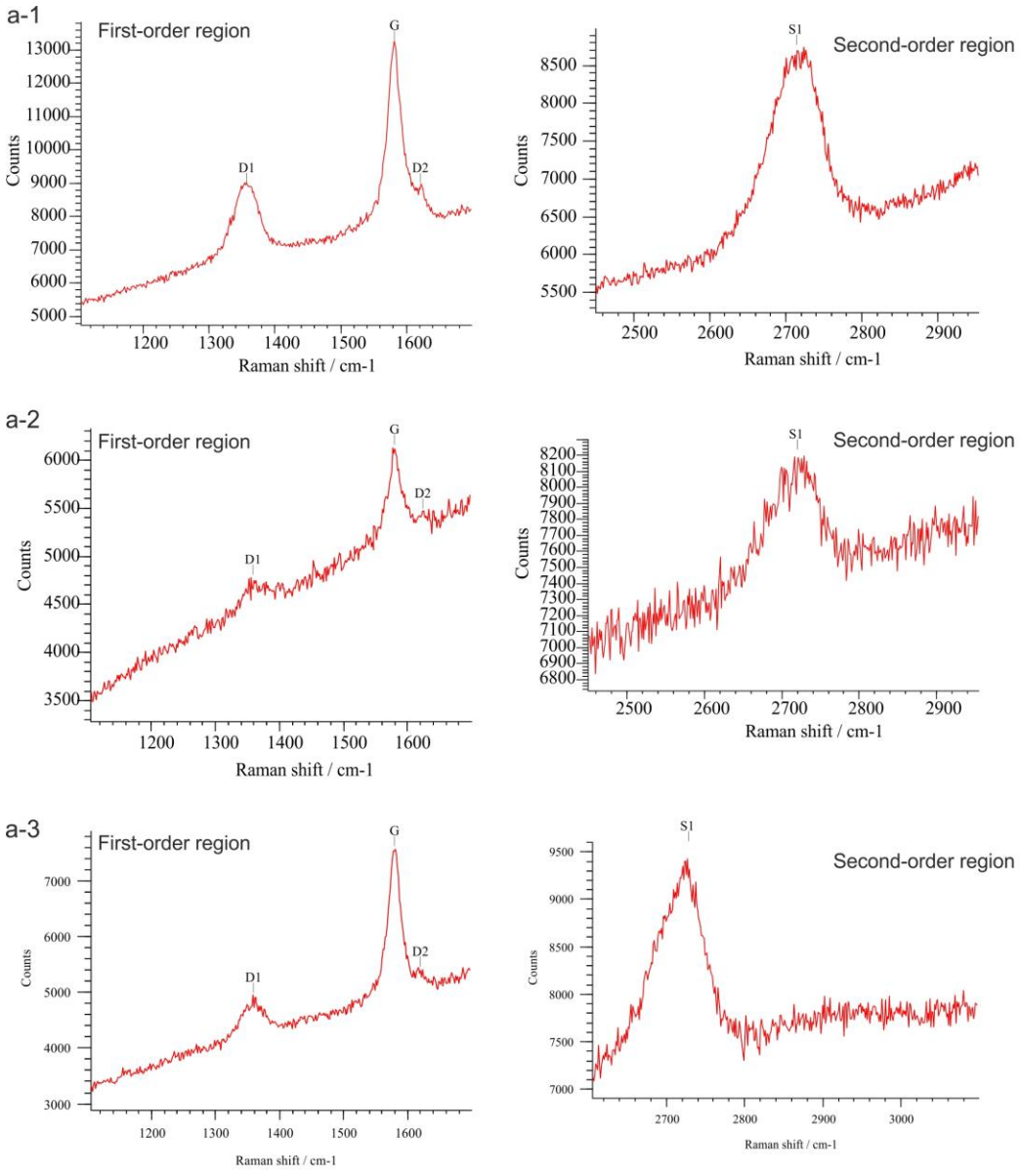

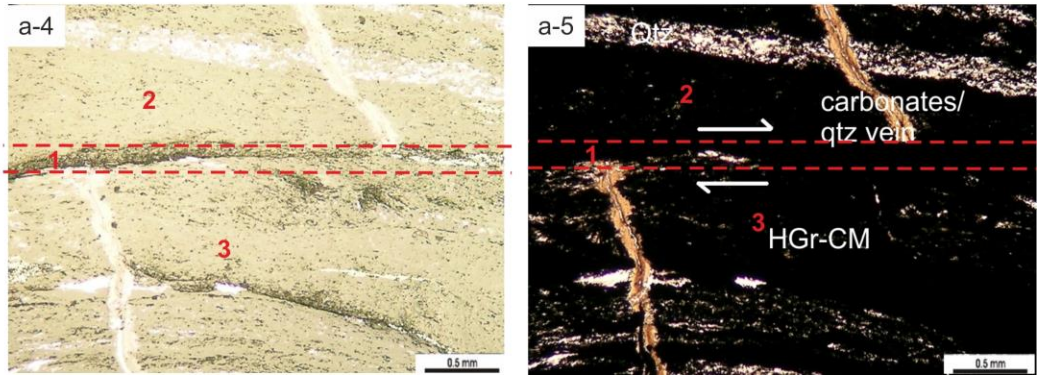

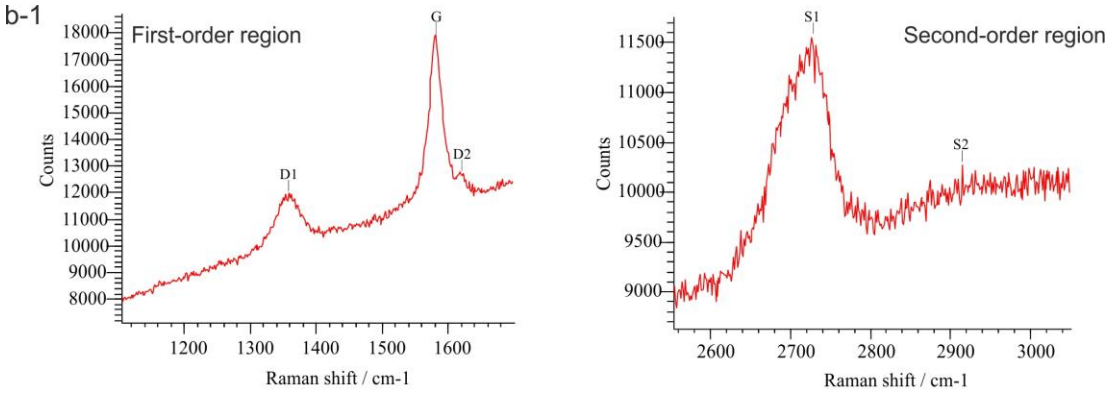
b-1
First-order region
G
D1
D2
Counts
Raman shift / cm-1
Second-order region
S1
S2
Counts
Raman shift / cm-1

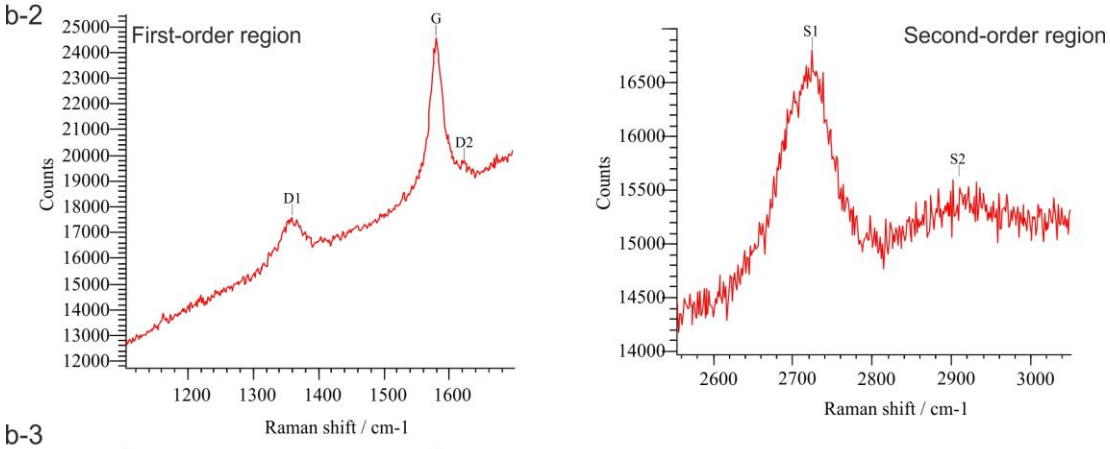
b-2
First-order region
G
D1
D2
Counts
Raman shift / cm-1
Second-order region
S1
S2
Counts
Raman shift / cm-1

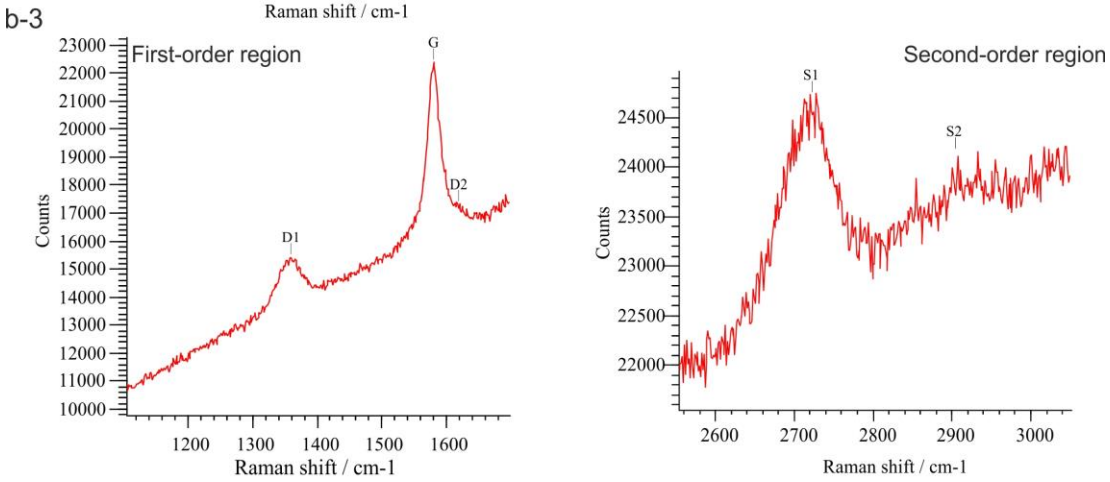
b-3
First-order region
G
D1
D2
Counts
Raman shift / cm-1
Second-order region
S1
S2
Counts
Raman shift / cm-1

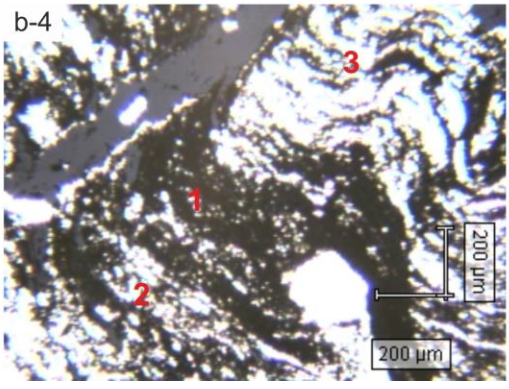
b-4
3
1
2
200 µm
200 µm

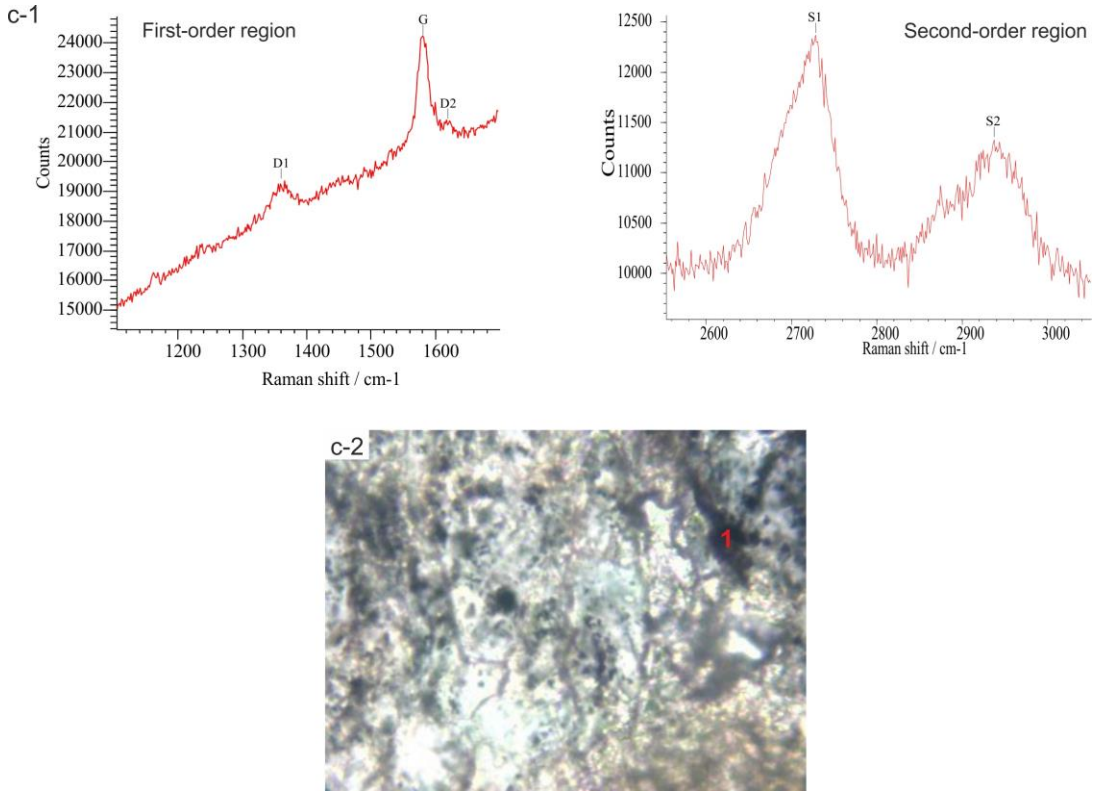

Figure E-1. Raman spectra showing the variability of well-crystallized graphite in different areas in samples from the graphitic pelitic schist and from the RGZ. The spectra show nice graphite band (G band), defect band 1 (D1) and defect band 2 (D2) in the first-order regions, and S1 and sometimes S2 bands in the second-order regions. (a) Sample SW18-565.1. a-1, a-2, a-3 are the spectra corresponding to the area 1, 2, 3, on pictures a-4 (transmitted light) and a-5 (reflected light), respectively. (b) Sample SW18-565.1. b-1, b-2, b-3 are the spectra corresponding to the area 1, 2, 3, on picture b-4 (reflected light), respectively. (c) Sample SW10-389.5 from the RGZ. c-1 are the spectra corresponding to the area 1 on picture c-2

APPENDIX F
WHOLE ROCK GEOCHEMISTRY RESULTS

Table F-1. Major elements

Sample	Zone	mineralized fence	SiO2 *(wt %)*	TiO2	Al2O3	Fe2O3	MnO	MgO	CaO	Na2O	K2O	P2O5	LOI	SUM
DF60-384.2	VGPS	in	59.5	0.90	14.9	7.42	0.06	5.68	0.10	0.09	2.30	0.04	9.2	100.19
DF60-403.8	VGPS	in	51.2	0.60	14.6	18.6	0.15	6.52	0.10	0.05	0.75	0.14	7.0	99.71
SW10-377.9	RGZ	in	34.3	1.14	28	7.54	0.07	14.6	0.31	0.17	1.42	0.16	12.2	99.91
SW10-389.5	RZ	in	67.1	0.48	11.2	6.7	0.07	7.43	0.09	0.02	0.18	0.04	5.6	98.91
SW10-392.5	RGZ	in	51	0.63	16.8	11	0.07	11.8	0.16	0.02	0.14	0.05	8.5	100.17
SW10-396.5	GZ	in	65.9	0.37	10.6	12.5	0.12	5.67	0.34	0.02	0.1	0.14	4.4	100.16
SW10-404.7	GZ	in	53.9	0.75	16.6	8.79	0.06	9.14	0.02	0.06	0.74	0.04	9.1	99.20
SW13-373.1	GZ	in	20	0.44	10.9	32	0.11	14.1	3.33	0.02	0.12	2.29	16.9	100.21
SW17-374.2	GZ	in	66.4	0.91	18	2.47	0.01	2.63	0.03	0.21	4.58	0.01	3.9	99.15
SW17-375	GZ	in	60.8	0.67	16	7.16	0.06	7.44	0.18	0.12	1.91	0.11	5.8	100.25
SW17-383.0	GZ	in	54.7	0.55	12.7	13	0.17	10.8	0.83	0.02	0.12	0.4	7.0	100.29
SW17-385.1	GZ	in	56.2	0.94	21.4	6.07	0.05	4.6	0.14	0.22	5.32	0.07	5.1	100.11
SW17-395	GZ	in	55.1	0.55	13.3	11.2	0.09	10	1.28	0.07	0.63	0.87	6.4	99.49
SW17-395.8	GZ	in	64.4	0.56	12	9.79	0.06	6.13	0.61	0.1	1.52	0.04	5.6	100.81
SW17-412.4	VGPS	in	37.5	0.55	12	26	0.09	6.52	0.7	0.03	0.17	0.44	16.6	100.60
SW17-415.1	VGPS	in	56.3	0.52	12.7	12.8	0.07	3.8	0.67	0.11	1.88	0.56	9.7	99.11
SW17-423.0	VGPS	in	50.7	0.46	11.4	17.6	0.06	4.7	1.07	0.08	1.27	0.75	12.9	100.99
SW17-425.1	VGPS	in	45.9	0.55	14.5	16.7	0.07	7.22	1.08	0.05	0.41	0.94	12.8	100.22
SW17-433.9	VGPS	in	67.6	0.66	14.1	7.13	0.08	3.21	0.26	0.11	2.94	0.17	4.2	100.46
SW18-369.9	BZ	in	52	0.91	28.8	2.85	<0.01	9.04	0.13	0.73	0.18	0.1	6.1	100.84
SW18-380.6	RGZ	in	45.7	0.73	18.8	7.67	0.1	16.9	0.14	0.03	0.21	0.04	10.6	100.92
SW18-382.5	RGZ	in	59.5	0.61	13.9	6.57	0.05	11.4	0.29	0.03	0.19	0.11	7.6	100.25

Sample	Zone	mineralized fence	SiO2 *(wt %)*	TiO2	Al2O3	Fe2O3	MnO	MgO	CaO	Na2O	K2O	P2O5	LOI	SUM
SW18-409.4	GZ	in	66.4	0.72	16.4	5.48	0.07	2.64	0.05	0.18	3.72	<0.01	4.2	99.86
SW18-415	VGPS	in	58.9	0.83	18.3	8.18	0.1	3.4	0.14	0.2	4.01	0.1	5.9	100.06
SW18-416.1	VGPS	in	58.5	0.85	18.7	8.35	0.1	3.09	0.12	0.2	4.12	0.08	6.0	100.11
SW18-425	VGPS	in	58.3	0.65	16.9	8.25	0.07	1.95	0.26	0.19	4.52	0.13	9.3	100.52
SW18-469.8	VGPS	in	60.5	0.81	17.2	8.62	0.13	2.82	0.06	0.17	3.73	0.03	5.9	99.97
SW18-475	VGPS	in	49.7	0.78	17.9	13.8	0.12	4.51	0.14	0.12	3.21	0.11	9.5	99.89
SW18-481.4	VGPS	in	45.1	0.89	20.8	14.2	0.11	4.5	0.14	0.16	4.23	0.1	9.0	99.23
SW18-495	VGPS	in	59.6	0.71	17.2	9.49	0.09	3.53	0.14	0.15	3.7	0.1	6.0	100.71
SW18-515	VGPS	in	70.3	0.59	14.6	4.14	0.03	1.87	0.12	0.22	3.82	0.06	4.1	99.85
SW18-535.1	VGPS	in	56.9	0.76	19.3	8.48	0.1	3.44	0.17	0.2	4.25	0.14	6.8	100.54
SW18-565.1	VGPS	in	59.9	0.72	17	8.84	0.11	3.43	0.18	0.17	3.3	0.16	5.8	99.61
SW18-595.1	VGPS	in	57	0.76	21.1	7.95	0.06	3.1	0.16	0.37	4.55	0.12	5.1	100.27
SW19-369.5	BZ	in	43.7	1.56	35.7	1.9	0.01	4.76	0.09	0.66	5.41	0.14	5.9	99.83
SW19-376.2	RGZ	in	65.8	0.88	19	1.61	<0.01	4.87	0.04	0.15	3.17	0.05	5.2	100.77
SW19-384.2	GZ	in	57.9	0.73	15.8	8.71	0.04	4.7	0.32	0.15	3.01	0.04	8.9	100.30
SW19-398.0	VGPS	in	58.5	1	22.1	4.29	0.03	2.68	0.03	0.25	5.6	0.02	6.1	100.60
SW19-413.2	VGPS	in	50.8	0.61	15.1	18.4	0.11	6.26	0.18	0.06	1.25	0.13	7.2	100.10
SW20-375.3	BZ	in	46.5	1.15	33.1	2.13	0.01	5.62	0.07	0.49	5.36	0.04	5.5	99.97
SW20-381.6	RZ	in	65.1	0.55	13.7	4.96	0.04	6.47	1.29	0.09	2.02	0.16	6.1	100.48
SW20-397.5	RGZ	in	55.7	0.88	22.5	3.27	<0.01	7.96	0.1	0.1	1.98	0.21	7.5	100.20
SW20-406.2	GZ	in	62.2	0.87	19.2	3.91	<0.01	4.95	0.06	0.15	3.82	0.03	5.0	100.19
SW20-410.6	GZ	in	61.9	0.92	21.6	2.48	<0.01	3.1	0.04	0.23	5.74	0.02	4.1	100.13
SW42-458.6	RGZ	out	71.8	0.7	16.1	2.03	<0.01	1.96	0.07	0.12	4.58	0.05	3.0	97.41
SW42-484.0	VGPS	out	66.9	0.7	14.2	6.61	0.05	3.32	0.03	0.09	3.08	<0.01	5.3	94.98

VGPS: Variably graphitic pelitic schist; RGZ: Red/green zone, including the red zone (RZ) and the green zone (GZ); BZ: Bleached zone

Table F-2. Trace elements, carbon and sulfur

Sample	Zone	mineralized fence	C (wt%)	S	B *(ppm)*	Ba	Ga	As	Cr	V	Li	Ni	Co	Cu
DF60-384.2	VGPS	in	4.84	0.43	344	182	19	104	276	224	201	99	45	67
DF60-403.8	VGPS	in	0.83	1.66	228	74	22	50	228	121	216	70	35	23
SW10-377.9	RGZ	in	0.62	0.01	2130	376	36	100	128	165	384	1600	257	884
SW10-389.5	RZ	in	0.29	0.01	35	10	15	20	74	78	91	161	39	4
SW10-392.5	RGZ	in	0.61	0.01	55	3	26	25	62	87	171	318	75	118
SW10-396.5	GZ	in	0.24	0.03	36	1	15	<1	102	96	170	120	36	59
SW10-404.7	GZ	in	1.4	2.29	654	138	23	85	113	184	176	91	100	27
SW13-373.1	GZ	in	0.91	10.79	48	<1	32	1110	83	304	73	1700	1720	5610
SW17-374.2	GZ	in	0.33	0.01	167	728	27	3	175	101	56	47	19	3
SW17-375	GZ	in	0.27	0.01	206	346	22	5	176	107	175	122	66	5
SW17-383.0	GZ	in	0.31	0.07	53	2	18	46	80	85	237	242	134	59
SW17-385.1	GZ	in	0.34	0.01	211	806	28	2	248	132	116	53	33	3
SW17-395	GZ	in	0.56	0.01	185	145	23	6	152	190	144	92	21	3
SW17-395.8	GZ	in	0.98	0.01	201	342	21	<1	92	165	115	33	12	35
SW17-412.4	VGPS	in	5.37	8.84	120	17	24	79	82	245	206	253	178	84
SW17-415.1	VGPS	in	3.08	5.25	215	370	20	175	144	151	83	87	65	14
SW17-423.0	VGPS	in	4.18	6.13	166	367	22	127	77	220	96	105	78	45
SW17-425.1	VGPS	in	4.64	5.16	209	143	20	115	155	229	156	108	68	26
SW17-433.9	VGPS	in	0.48	0.54	236	325	18	41	309	102	78	46	20	6
SW18-369.9	BZ	in	0.56	0.01	13100	15	41	8	234	130	92	389	90	167
SW18-380.6	RGZ	in	0.65	0.01	148	9	28	2	115	151	412	565	120	56
SW18-382.5	RGZ	in	0.5	0.01	142	6	21	21	87	109	256	220	86	18
SW18-398	RGZ	in	1.99	0.01	35	<1	23	108	48	168	146	201	148	16
SW18-409.4	GZ	in	0.53	0.59	143	609	23	29	131	104	57	63	35	11
SW18-415	VGPS	in	1.43	0.99	88	608	24	20	207	114	73	67	24	194
SW18-416.1	VGPS	in	1.21	1.42	216	605	27	19	136	134	105	56	28	251
SW18-425	VGPS	in	4.14	3.59	32	815	24	4	175	296	45	69	36	258

Sample	Zone	mineralized fence	C (wt%)	S	B *(ppm)*	Ba	Ga	As	Cr	V	Li	Ni	Co	Cu
SW18-469.8	VGPS	in	0.74	0.53	51	502	24	73	135	112	71	73	30	8
SW18-475	VGPS	in	2.92	3.71	562	358	25	72	246	211	109	113	50	74
SW18-481.4	VGPS	in	2.11	3.39	387	527	30	62	151	188	76	97	42	16
SW18-495	VGPS	in	1.12	1.7	190	558	24	33	213	138	81	69	27	54
SW18-515	VGPS	in	0.78	0.9	140	678	18	83	168	99	36	44	29	14
SW18-535.1	VGPS	in	1.54	2.12	205	619	26	17	209	145	63	57	27	14
SW18-565.1	VGPS	in	1.7	0.79	175	521	22	23	212	137	65	40	17	80
SW18-595.1	VGPS	in	0.52	0.86	39	619	27	8	189	131	71	49	14	23
SW19-369.5	BZ	in	0.84	0.01	12200	683	52	1	215	197	41	44	18	31
SW19-376.2	RGZ	in	0.25	0.01	523	371	29	2	153	127	75	84	23	<1
SW19-384.2	GZ	in	1.96	0.01	302	381	24	<1	106	127	83	61	24	6
SW19-398.0	VGPS	in	1.24	0.88	275	811	30	29	165	179	66	65	56	10
SW19-413.2	VGPS	in	1.18	2.35	207	197	18	15	99	115	164	85	31	10
SW20-375.3	BZ	in	0.33	0.01	9530	598	52	<1	193	190	38	66	26	21
SW20-381.6	RZ	in	0.59	0.01	119	255	20	<1	74	96	93	113	50	6
SW20-397.5	RGZ	in	0.08	0.01	642	181	21	<1	167	105	142	82	6	6
SW20-406.2	GZ	in	0.14	0.01	304	478	26	<1	144	167	80	51	7	9
SW20-410.6	GZ	in	0.17	0.01	359	648	29	<1	147	126	44	30	5	9
SW42-458.6	RGZ	out	0.12	0.01	221	724	26	<1	64	105	33	49	23	<1
SW42-484.0	VGPS	out	1.13	0.17	177	520	22	11	106	136	53	65	42	10

Sample	Be	Sc	Zr	Sr	Y	Pb	Nb	Mo	Ag	Cd	Sn	Hf	Ta	W	Bi	Th	U	Zn
DF60-384.2	2.1	17	118	24	21	13	9	11	<0.2	1	6	3	<1	<1	1	8	37	80
DF60-403.8	2.6	11	109	57	14	12	7	3	0.2	2	3	3	<1	<1	9	10	17	157
SW10-377.9	7.2	25	250	321	107	37	19	5	0.9	3	8	8	<1	2	9	23	24	434
SW10-389.5	1.6	11	95	51	38	11	9	<1	<0.2	1	5	4	<1	<1	<1	9	15	64
SW10-392.5	2.9	9	135	14	38	9	11	<1	0.5	1	5	4	<1	<1	6	8	11	156
SW10-396.5	2.4	10	83	27	53	10	8	<1	0.6	1	5	2	<1	<1	15	10	2	191
SW10-404.7	2.6	16	128	75	16	29	13	5	0.4	2	5	7	<1	<1	16	13	7	99
SW13-373.1	6.2	10	74	18	47	44	6	1	1.8	3	5	2	<1	6	166	8	37	203
SW17-374.2	1.7	17	188	28	14	40	10	<1	0.7	1	7	6	<1	<1	<1	7	6	34
SW17-375	2.8	16	119	61	14	8	6	<1	<0.2	1	4	3	<1	<1	<1	11	5	77
SW17-383.0	4	12	104	26	24	7	8	<1	0.5	1	3	4	<1	9	23	9	8	242
SW17-385.1	2.6	25	138	86	38	21	5	<1	<0.2	1	6	4	<1	<1	<1	11	5	97
SW17-395	4.2	9	105	21	29	22	10	1	<0.2	1	<1	3	<1	5	4	10	14	171
SW17-395.8	3.6	11	120	44	20	22	12	<1	0.6	1	6	3	<1	7	40	13	3	114
SW17-412.4	2.8	11	127	14	28	38	14	11	2	2	8	3	<1	6	138	14	6	263
SW17-415.1	1.4	12	104	16	21	27	7	3	0.2	1	9	2	<1	2	27	10	7	114
SW17-423.0	1.8	14	107	69	30	34	12	10	1.2	2	7	3	<1	2	131	12	<2	135
SW17-425.1	2.3	13	109	53	31	25	11	11	0.2	2	2	3	<1	<1	27	13	9	173
SW17-433.9	1.6	13	110	21	19	7	5	<1	<0.2	1	6	2	<1	<1	5	5	2	69
SW18-369.9	13.2	26	166	225	54	26	12	<1	0.8	1	6	5	<1	<1	2	18	65	81
SW18-380.6	6.5	19	171	48	54	10	14	<1	0.4	1	4	5	<1	<1	3	14	5	58
SW18-382.5	4.6	13	133	46	38	10	11	<1	0.4	1	4	4	<1	<1	5	12	21	44
SW18-398	3.3	12	69	35	49	8	8	<1	<0.2	2	3	2	<1	12	12	9	12	237
SW18-409.4	1.5	18	118	19	15	17	7	<1	0.6	1	6	3	<1	1	<1	9	<2	74
SW18-415	2	18	130	25	14	11	4	<1	<0.2	1	7	3	<1	<1	<1	10	3	79
SW18-416.1	1.6	18	151	31	17	16	10	1	0.6	1	8	4	<1	<1	<1	11	<2	119
SW18-425	1.8	20	123	28	33	21	12	16	<0.2	1	8	3	<1	<1	<1	12	9	50
SW18-469.8	1.8	17	138	34	19	11	8	<1	0.5	1	7	3	<1	2	20	9	6	97

Sample	Be	Sc	Zr	Sr	Y	Pb	Nb	Mo	Ag	Cd	Sn	Hf	Ta	W	Bi	Th	U	Zn
SW18-475	2.5	21	131	24	21	14	9	5	0.2	2	7	3	<1	<1	<1	12	7	101
SW18-481.4	1.5	20	123	31	15	23	11	2	<0.2	2	6	8	<1	1	5	10	2	92
SW18-495	2	17	114	31	18	12	6	4	<0.2	1	7	3	<1	<1	2	10	6	66
SW18-515	1.7	11	145	28	12	17	7	2	<0.2	1	7	4	<1	<1	7	10	4	61
SW18-535.1	1.7	18	125	45	26	15	5	2	<0.2	1	4	3	<1	<1	<1	11	5	90
SW18-565.1	1.7	16	102	27	19	9	4	1	<0.2	1	5	3	<1	<1	<1	8	4	115
SW18-595.1	1.8	18	154	49	18	13	6	<1	<0.2	1	7	4	<1	<1	1	13	4	115
SW19-369.5	8.4	31	270	320	41	56	17	<1	1.3	2	9	7	1	<1	<1	19	187	32
SW19-376.2	2	19	141	106	16	12	10	<1	0.5	1	6	4	<1	<1	<1	9	20	30
SW19-384.2	2.1	15	161	103	40	10	8	<1	0.4	1	6	5	<1	<1	7	9	5	36
SW19-398.0	2	23	156	42	14	17	10	1	0.6	1	7	4	<1	<1	21	11	<2	75
SW19-413.2	2.6	13	90	19	25	15	9	1	<0.2	2	5	8	<1	<1	5	7	<2	62
SW20-375.3	6.9	27	216	73	22	18	16	<1	0.6	2	8	6	<1	<1	2	17	18	28
SW20-381.6	2.6	12	114	20	16	11	6	<1	0.3	1	4	4	<1	<1	2	6	11	22
SW20-397.5	2.6	16	143	102	461	11	8	<1	0.3	1	4	4	<1	<1	<1	16	<2	15
SW20-406.2	2.1	19	154	35	24	20	10	<1	0.3	1	7	5	<1	<1	2	10	<2	23
SW20-410.6	2	19	168	31	17	13	10	<1	0.6	1	7	5	<1	<1	1	11	<2	23
SW42-458.6	1.4	17	168	64	18	8	13	<1	0.5	1	8	4	1	<1	<1	17	<2	37
SW42-484.0	1.2	16	120	20	10	10	9	<1	0.5	1	8	4	<1	1	4	9	<2	102

VGPS: Variably graphitic pelitic schists; RGZ: Red/green zone, including the red zone (RZ) and the green zone (GZ); BZ: Bleached zone

Table F-3. Rare Earth Elements

Sample	La	Ce	Pr	Nd	Sm	Eu	Gd	Tb	Dy	Ho	Er	Yb	Total REE	HREE	LREE	HREE/LREE
DF60-384.2	15	30	1	12	1	0.4	<1	<1	3.4	<1	1.8	2.1	66.7	7.3	59.4	0.12
DF60-403.8	93	193	20	85	9	1.0	<1	<1	3.0	<1	1.7	1.7	407.4	6.4	401	0.02
SW10-377.9	106	212	23	100	3	3.7	19	3	15.8	3	9.3	7.6	505.4	38.7	466.7	0.08
SW10-389.5	60	112	11	50	8	1.8	7	<1	6.8	2	4.7	3.2	266.5	16.7	249.8	0.07
SW10-392.5	28	58	5	23	5	1	6	1	6.5	1	3.9	3.4	141.8	15.8	126	0.13
SW10-396.5	43	77	8	31	4	1.3	8	1	8.9	1	4.8	4.2	192.2	19.9	172.3	0.12
SW10-404.7	87	145	13	51	6	0.9	4	<1	2.6	1	3.1	2.1	315.7	8.8	306.9	0.03
SW13-373.1	11	26	3	22	2	1.4	11	<1	7.9	1	4.4	4.5	94.2	17.8	76.4	0.23
SW17-374.2	3	6	<1	1	<1	0.2	1	<1	1.9	<1	2.7	1.5	17.3	6.1	11.2	0.54
SW17-375	18	40	1	12	1	0.4	<1	<1	2.4	<1	1.2	1.4	77.4	5	72.4	0.07
SW17-383.0	28	49	3	15	4	0.6	4	<1	4.6	<1	2.8	2.7	113.7	10.1	103.6	0.10
SW17-385.1	52	92	5	29	3	0.8	2	<1	5.6	1	3.2	3.4	197	13.2	183.8	0.07
SW17-395	5	15	<1	9	3	0.9	<1	<1	5	1	2.5	2.9	44.3	11.4	32.9	0.35
SW17-395.8	84	127	12	42	7	0.8	5	<1	3.6	<1	2.1	1.8	285.3	7.5	277.8	0.03
SW17-412.4	66	137	15	54	9	1	9	<1	5.9	1	3	3.1	304	13	291	0.04
SW17-415.1	9	19	<1	7	1	0.3	<1	<1	3.7	<1	1.8	2	43.8	7.5	36.3	0.21
SW17-423.0	100	180	21	73	4	1.6	8	1	5.7	1	3.1	3	401.4	13.8	387.6	0.04
SW17-425.1	91	164	15	62	7	1.1	<1	<1	5.7	1	2.7	2.9	352.4	12.3	340.1	0.04
SW17-433.9	17	37	2	14	2	0.6	<1	<1	3.3	<1	1.6	1.7	79.2	6.6	72.6	0.09
SW18-369.9	31	62	3	27	4	0.9	6	1	9.7	1	5.2	4.2	155	21.1	133.9	0.16
SW18-380.6	30	52	3	22	4	1.1	7	1	8.1	1	5.2	4.8	139.2	20.1	119.1	0.17
SW18-382.5	29	57	4	24	5	1.1	6	1	6.1	1	3.6	3	140.8	14.7	126.1	0.12
SW18-398	55	97	9	34	2	1	10	1	8.1	1	4.3	4.2	226.6	18.6	208	0.09
SW18-409.4	20	46	2	19	4	0.6	3	<1	2.7	<1	1.8	1.8	100.9	6.3	94.6	0.07
SW18-415	32	63	4	26	4	0.8	1	<1	2.7	<1	1.3	1.6	136.4	5.6	130.8	0.04
SW18-416.1	36	70	6	29	2	0.9	5	<1	3.4	<1	2.2	1.9	156.4	7.5	148.9	0.05
SW18-425	52	92	8	41	6	1.2	3	<1	5.4	1	2.8	3.3	215.7	12.5	203.2	0.06

Sample	La	Ce	Pr	Nd	Sm	Eu	Gd	Tb	Dy	Ho	Er	Yb	Total REE	HREE	LREE	HREE/LREE
SW18-469.8	16	32	1	14	13	0.6	4	<1	3.5	<1	2.4	2.2	88.7	8.1	80.6	0.10
SW18-475	32	75	5	31	5	1.2	<1	<1	4.3	<1	2	2.5	158	8.8	149.2	0.06
SW18-481.4	26	49	3	19	2	0.6	3	<1	3	1	3.3	1.9	111.8	9.2	102.6	0.09
SW18-495	46	83	6	30	4	0.9	<1	<1	3.5	1	1.8	2	178.2	8.3	169.9	0.05
SW18-515	9	18	<1	5	<1	0.3	<1	<1	1.9	<1	1.1	1.3	36.6	4.3	32.3	0.13
SW18-535.1	54	104	8	41	5	1.3	2	<1	4.4	1	2.1	2.2	225	9.7	215.3	0.05
SW18-565.1	28	58	4	22	3	0.9	<1	<1	3.6	<1	1.8	2	123.3	7.4	115.9	0.06
SW18-595.1	32	61	4	25	3	0.9	1	<1	3.1	<1	1.6	1.9	133.5	6.6	126.9	0.05
SW19-369.5	115	193	24	106	8	3	12	2	8.7	1	5	3.1	480.8	19.8	461	0.04
SW19-376.2	47	99	9	49	8	1.6	5	<1	2.8	1	3.2	1.6	227.2	8.6	218.6	0.04
SW19-384.2	59	95	14	59	1	1.9	9	1	6.9	1	3.8	3.2	254.8	15.9	238.9	0.07
SW19-398.0	26	49	2	17	2	0.5	3	<1	2.3	<1	2.1	1.8	105.7	6.2	99.5	0.06
SW19-413.2	35	68	6	29	4	0.9	4	<1	4.7	1	3.6	2.7	158.9	12	146.9	0.08
SW20-375.3	22	31	1	17	46	0.6	3	<1	3.7	<1	3.1	2.7	130.1	9.5	120.6	0.08
SW20-381.6	9	18	<1	9	17	0.6	4	<1	3.2	<1	1.7	1.5	64	6.4	57.6	0.11
SW20-397.5	84	194	18	68	3	7.6	59	13	88	15	37.5	24.4	611.5	177.9	433.6	0.41
SW20-406.2	21	44	2	19	1	1.1	5	<1	4.1	<1	2.8	2.3	102.3	9.2	93.1	0.10
SW20-410.6	10	23	<1	8	2	0.5	3	<1	2.8	<1	2.2	1.9	53.4	6.9	46.5	0.15
SW42-458.6	26	49	3	18	<1	0.5	3	<1	2.9	<1	2.2	2	106.6	7.1	99.5	0.07
SW42-484.0	8	17	<1	5	<1	<0.2	2	<1	1.7	<1	1.4	1.5	36.6	4.6	32	0.14

LREE: La+Ce+Pr+Nd+Sm+Eu+Gd, HREE: Tb+Dy+Ho+Er+Yb

APPENDIX G
MICROTHERMOMETRY DATA

Table G-1. Microthermometry and Raman data

Samples	Zone	Qtz type	FI name	FI type	Tmice	Tmh	Th(L)	Th(V)	Raman results		
									CO_2	CH_4	N_2
					°C	°C	°C	°C	wt %	wt %	wt %
SW42-484.0	VGPS	Q2	a1	Vw	n.d	n.d	n.d	-79.0			
SW42-484.0	VGPS	Q2	b1-1	Vw	n.d	n.d	n.d	-128.4	1.4	11.9	86.7
SW42-484.0	VGPS	Q2	b1-2	Vw	n.d	n.d	n.d	-128.4	1.6	11.7	86.7
SW42-484.0	VGPS	Q2	b1-3	Vw	n.d	n.d	n.d	-128.4	1.1	11.9	87
SW42-484.0	VGPS	Q2	b1-4	Vw	n.d	n.d	n.d	-100.8	1.9	11	87.1
SW42-484.0	VGPS	Q2	b1-5	Vw	n.d	n.d	n.d	-9.9			
SW42-484.0	VGPS	Q2	b2-1	Vw	n.d	n.d	n.d	-133.4			
SW42-484.0	VGPS	Q2	b2-2	Vw	n.d	n.d	n.d	-93.9			
SW42-484.0	VGPS	Q2	b2-3	Vw	n.d	n.d	n.d	-137.3			
SW42-484.0	VGPS	Q2	b2-4	Vw	n.d	n.d	n.d	-100.8			
SW42-484.0	VGPS	Q2	c1	Vw	n.d	n.d	n.d	-81.0		95.5	4.5
SW42-484.0	VGPS	Q2	c2	Vw	n.d	n.d	n.d	-79.0			
SW42-484.0	VGPS	Q2	d1	Vw	n.d	n.d	n.d	-134.3		13.4	86.3
SW42-484.0	VGPS	Q2	d2	Vw	n.d	n.d	n.d	-130.4		12.2	87.8
SW42-484.0	VGPS	Q2	d3	Vw	n.d	n.d	n.d	-130.4			
SW42-484.0	VGPS	Q2	d4	Vw	n.d	n.d	n.d	-152.1		16.8	83.2
SW42-484.0	VGPS	Q2	e1	Vw	n.d	n.d	n.d	-91.9			
SW42-484.0	VGPS	Q2	e2	Vw	n.d	n.d	n.d	-88.9			
SW42-484.0	VGPS	Q2	e3-1	Vw	n.d	n.d	n.d	-85.0			
SW42-484.0	VGPS	Q2	e3-2	Vw	n.d	n.d	n.d	-150.1			
SW42-484.0	VGPS	Q2	e3-3	Vw	n.d	n.d	n.d	-74.1	16.4	77.2	6.4
SW42-484.0	VGPS	Q2	e3-4	Vw	n.d	n.d	n.d	-79.0		85.3	14.7
SW42-484.0	VGPS	Q2	e3-5	Vw	n.d	n.d	n.d	-125.5			
SW42-484.0	VGPS	Q2	e4-1	Vw	n.d	n.d	n.d	-79.0			
SW42-484.0	VGPS	Q2	e4-2	Vw	n.d	n.d	n.d	-128.4			
SW18-382.5a	RGZ	Q2	a1	Lwh	n.d	193.1	82.6	n.d			
SW18-382.5a	RGZ	Q2	b1	Lw	-25.5	n.d	148.4	n.d			
SW18-382.5a	RGZ	Q2	b2	Lw	-25.3	n.d	115.4	n.d			
SW18-382.5a	RGZ	Q2	b3	Lw	-25.3	n.d	143.8	n.d			
SW18-382.5a	RGZ	Q2	b4	Lw	-25.8	n.d	123.5	n.d			
SW18-382.5a	RGZ	Q2	b5	Lw	-25.9	n.d	118.4	n.d			
SW18-382.5a	RGZ	Q2	b6	Lw	-22.6	n.d	146.2	n.d			
SW18-382.5a	RGZ	Q2	b7	Lw	-31.5	n.d	154.2	n.d			
SW18-382.5a	RGZ	Q2	b8	Lw	-30.3	n.d	181.3	n.d			

Samples	Zone	Qtz type	FI name	FI type	Tmice	Tmh	Th(L)	Th(V)	Raman results		
									CO_2	CH_4	N_2
					°C	°C	°C	°C	wt %	wt %	wt %
SW18-382.5a	RGZ	Q2	b12	Lw	n.d	n.d	n.d	-137.3		22.1	77.9
SW18-382.5a	RGZ	Q2	b12b	Vw	n.d	n.d	n.d	n.d		16.3	83.7
SW18-382.5a	RGZ	Q2	b12c	Vw	n.d	n.d	n.d	n.d		14.7	85.3
SW18-382.5a	RGZ	Q2	b13	Lw	-31.6	n.d	n.d	n.d			
SW18-382.5a	RGZ	Q2	b14	Lw	-31.2	n.d	n.d	n.d			
SW18-382.5a	RGZ	Q2	b15	Lw	-32.5	n.d	n.d	n.d			
SW18-382.5a	RGZ	Q2	b16	Lw	-23.4	n.d	275.0	n.d			
SW18-382.5a	RGZ	Q2	b17	Lw	-20.6	n.d	151.9	n.d			
SW18-382.5a	RGZ	Q2	b18	Lwh	n.d	n.d	n.d	n.d			
SW18-382.5a	RGZ	Q2	b19	Lw	-25.3	n.d	160.9	n.d			
SW18-382.5a	RGZ	Q2	b20	Lwh	n.d	n.d	n.d	n.d			
SW18-382.5a	RGZ	Q2	b21	Lw	-31.6	n.d	n.d	n.d			
SW18-382.5a	RGZ	Q2	b22	Lw	-25.9	n.d	123.4	n.d			
SW18-382.5a	RGZ	Q2	b25	Lw	-25.8	n.d	123.0	n.d			
SW18-382.5a	RGZ	Q2	b26	Lw	-24.8	n.d	127.4	n.d			
SW18-382.5a	RGZ	Q2	b27	Lw	-19.1	n.d	134.4	n.d			
SW18-382.5a	RGZ	Q2	b28	Lw	-20.7	n.d	163.9	n.d			
SW18-382.5a	RGZ	Q2	b29	Lwh	n.d	217.7	79.5	n.d			
SW18-382.5a	RGZ	Q2	b30	Lw	-23.8	n.d	141.9	n.d			
SW18-382.5a	RGZ	Q2	b31	Lw	-17.3	n.d	219.8	n.d			
SW18-382.5a	RGZ	Q2	c1	Lwh	n.d	197.4	93.7	n.d			
SW18-382.5a	RGZ	Q2	c2	Lw	n.d	n.d	217.2	n.d			
SW18-382.5a	RGZ	Q2	c3	Lw	n.d	n.d	207.8	n.d			
SW18-382.5a	RGZ	Q2	d1	Lwh	n.d	212.0	83.1	n.d			
SW18-382.5a	RGZ	Q2	d2	Lwh	n.d	216.5	69.1	n.d			
SW18-382.5a	RGZ	Q2	e1	Lw	-23.1	n.d	119.1	n.d			
SW18-382.5a	RGZ	Q2	e2	Lw	-22.6	n.d	111.2	n.d			
SW18-382.5a	RGZ	Q2	e3	Lw	-26.5	n.d	118.0	n.d			
SW18-382.5a	RGZ	Q2	e4	Lw	-15.9	n.d	n.d	n.d			
SW18-382.5a	RGZ	Q2	e5	Lw	-16.4	n.d	107.5	n.d			
SW18-382.5a	RGZ	Q2	e7	Lw	-16.5	n.d	127.8	n.d			
SW18-382.5a	RGZ	Q2	e8	Lw	-20.2	n.d	120.8	n.d			
SW18-382.5a	RGZ	Q2	e9	Lw	-23.1	n.d	n.d	n.d			
SW18-382.5a	RGZ	Q2	e10	Lw	-20.0	n.d	n.d	n.d			
SW18-382.5a	RGZ	Q2	e11	Lw	-29.5	n.d	131.0	n.d			
SW18-382.5b	RGZ	Q3	a1	Lw	-25.7	n.d	110.4	n.d			
SW18-382.5b	RGZ	Q3	a2	Lw	-26.0	n.d	90.6	n.d			
SW18-382.5b	RGZ	Q3	a3	Lw	-25.1	n.d	106.2	n.d			
SW18-382.5b	RGZ	Q3	a4	Lw	-24.9	n.d	154.8	n.d			

Samples	Zone	Qtz type	FI name	FI type	Tmice	Tmh	Th(L)	Th(V)	Raman results		
									CO_2	CH_4	N_2
					°C	°C	°C	°C	wt %	wt %	wt %
SW18-382.5b	RGZ	Q3	a8	Lw	-26.9	n.d	97.7	n.d			
SW18-382.5b	RGZ	Q3	a9	Lw	-28.2	n.d	108.9	n.d			
SW18-382.5b	RGZ	Q3	a10	Lw	-25.7	n.d	95.0	n.d			
SW18-382.5b	RGZ	Q3	a11	Lw	-26.2	n.d	n.d	n.d			
SW18-382.5b	RGZ	Q3	a12	Lw	-25.4	n.d	119.5	n.d			
SW18-382.5b	RGZ	Q3	a13	Lw	-29.4	n.d	107.1	n.d			
SW18-382.5b	RGZ	Q3	a14	Lw	-26.1	n.d	97.9	n.d			
SW18-382.5b	RGZ	Q3	a15	Lw	-24.7	n.d	146.2	n.d			
SW18-382.5b	RGZ	Q3	a16	Lw	-35.5	n.d	99.3	n.d			
SW18-382.5b	RGZ	Q3	a17	Lw	-26.8	n.d	n.d	n.d			
SW18-382.5b	RGZ	Q3	b1	Lw	-25.1	n.d	161.3	n.d			
SW18-382.5b	RGZ	Q3	c1	Lw	-25.4	n.d	121.2	n.d			
SW18-382.5b	RGZ	Q3	d1	Lwh	n.d	189.7	125.3	n.d			
SW18-382.5b	RGZ	Q3	d2	Lw	-23.5	n.d	124.3	n.d			
SW18-382.5b	RGZ	Q3	f1	Lw	-25.6	n.d	n.d	n.d			
SW18-382.5b	RGZ	Q3	f2	Lw	-24.5	n.d	n.d	n.d			
SW18-382.5b	RGZ	Q3	f3	Lw	-23.6	n.d	116.6	n.d			
SW18-382.5b	RGZ	Q3	f4	Lw	-25.1	n.d	126.9	n.d			
SW18-382.5b	RGZ	Q3	f5	Lw	-23.9	n.d	109.1	n.d			
SW18-382.5b	RGZ	Q3	f6	Lwh	n.d	199.3	100.3	n.d			
SW18-382.5b	RGZ	Q3	g1	Lwh	n.d	239.0	123.7	n.d			
SW18-382.5b	RGZ	Q3	g2	Lw	-25.9	n.d	114.3	n.d			
SW18-382.5b	RGZ	Q3	g5	Lw	-25.6	n.d	103.2	n.d			
SW18-382.5b	RGZ	Q3	g6	Lw	-25.7	n.d	113.7	n.d			
SW18-382.5b	RGZ	Q3	g7a	Lw	-25.6	n.d	103.3	n.d			
SW18-382.5b	RGZ	Q3	g7b	Lw	-25.7	n.d	92.4	n.d			

Qtz: Quartz, FI: Fluid inclusion, Tmice: Temperature of melting ice, Tmh: Temperature of melting halite, Th(L): Temperature of homogenization to the liquid phase, Th(V): Temperature of homogenization to the vapor phase, Vw: monophase volatile-rich fluid inclusion, Lw: two-phase fluid inclusion, Lwh: three-phase fluid inclusion, n.d: not detected